NORTHWESTERN UNIVERSITY

Design, Deposition, Characterization and Modification of Transparent, Conducting Anode Materials for Organic Light-Emitting Diodes

A DISSERTATION

SUBMITTED TO THE GRADUATE SCHOOL
IN PARTIAL FULFILLMENT OF THE REQUIREMENTS

for the degree

DOCTOR OF PHILOSOPHY

Field of Chemistry

By

Jianfeng Li

EVANSTON, ILLINOIS

June 2008

ABSTRACT

Design, Deposition, Characterization and Modification of Transparent, Conducting Anode Materials for Organic Light-Emitting Diodes

Jianfeng Li

The electronic properties of various transparent conducting oxide (TCO) surfaces are probed electrochemically via self-assembled monolayers (SAMs). A novel graftable probe molecule having a tethered trichlorosilyl group and a redox-active ferrocenyl functionality ($Fc(CH_2)_4SiCl_3$) is synthesized for this purpose. On as-received ITO, saturation coverage by a close-packed monolayer having of 6.6×10^{-10} mol/cm^2 and an electron-transfer rate of 6.65 s^{-1} is achieved after 9 hr of chemisorption. CV studies of this redox SAM on five different TCO surfaces reveal that MOCVD-derived CdO exhibits the greatest electro-active coverage and MOCVD-derived ZITO ($ZnIn_{2.0}Sn_{1.5}O$) exhibits the highest electron transfer rate.

Modification of inorganic electrodes has attracted great attention in the quest to optimize organic opto-electronic devices. An air-stable, crosslinkable trimethoxysilane functionalized hole-transporting triarylamine (4,4′-*bis*[(*p*-trimethoxysilylpropylphenyl) phenylamino]biphenyl, TPD-$[Si(OMe)_3]_2$) has been synthesized and self-assembled or spin-coated onto ITO anode surfaces to form monolayers or multilayer siloxane films, respectively. The increase in surface work function and enhanced ITO–HTL contact via robust covalent bonding are expected to facilitate hole injection from the ITO anode, resulting in OLED performance enhancement versus that of device without such interlayers. The air-stable interlayer material developed here is also applicable to large-area coating techniques.

Single-walled carbon nanotube (SWNT) films on flexible PET substrates are used as transparent, flexible anodes for organic light-emitting diodes (OLEDs). For polymer-based OLEDs having the carbon nanotube anode, a maximum light output of 3500 cd/m^2 and a current efficiency of 1.6 cd/A have been achieved. The device operational lifetime is comparable to that of devices with Sn-doped In_2O_3 (ITO)/PET anodes. The advantages of this novel type of anode over conventional ITO are discussed. Double-layer transparent conducting thin film structures containing single-walled carbon nanotubes (SW-CNTs) and Sn-doped In_2O_3 (ITO) layers are deposited on flexible PET substrates by a PDMS (poly-dimethylsiloxane)-based stamp printing method and ion-assisted deposition (IAD), respectively, at room temperature and used as anodes for polymer light-emitting diodes (PLEDs). The overall figure of merit ($\Phi = T^{10}/R_{sheet}$) of the film with 30 nm CNT and 50 nm IAD-derived ITO is greater than that of the CNT-only film. CNT/ITO-based PLEDs exhibit superior performance to that of the CNT-only control.

At last, a novel cyan emitting copolymer poly(2,5-N-n-octyl-3,4-cyclicimidothienyl-co-2',7'-9',9'-di-n- octylfluorene) (C8F8), consisting of electron-deficient cyclicimidothiophene and fluorene moieties, was synthesized and characterized.

_____

Thesis Advisor: Professor Tobin J. Marks

ACKNOWLEDGEMENTS

I am indebted to my advisor, Professor Tobin J. Marks for his guidance and support throughout my thesis research at Northwestern University. It has been a great opportunity and honor to work under his supervision. The research work in his group is no doubt the most significant part of my graduate school experience, and will have tremendous impact on my professional future. I am also grateful to Professor Robert Chang (Department of Materials Science and Engineering), Professor Peter Stair, and Professors Joseph Hupp (Department of Chemistry) for the suggestions and challenges they provided in my qualifying/research proposal/thesis exams and/or collaborative researches.

My research has been greatly motivated and enhanced through the discussion, collaboration, and friendship with many outstanding individuals. I would like to specially thank Dr. Liangbing Hu and Professor George Grüner at Department of Physics, University of California at Los Angles for providing Carbon Nanotube films. I would like to express my gratitude to Marks group, especially B-team members, for your friendship and camaraderie. Special thanks go to Dr. Qinglan Huang and Dr. He Yan who provide invaluable help and informative discussion for my beginning research life in Marks group and Northwestern University. I also would like to thank Jun Liu, Dr. Lian Wang, Dr. Jin Shu, and Norma Cortes, for their helpful experiments and discussion on transparent, conducting oxide films; Dr. Antonio Facchetti, and Dr. Gang Lu for close collaboration and discussion on the synthesis of π-conjugated light-emitting polymers. I also want to thank the research collaboration and support from Agiltron Inc. and Plextronics Inc. Highlighted thank goes to Dr. Qingwu Wang at Agiltron

and Dr. Shawn William, Dr. Chris Brown, and Dr. Darin Laird at Plextronics. In addition, I would like to thank Dr. Guennadi A. Evmenenko and Professor Pulak Dutta at Department of Physics for X-ray reflectivity measurements.

Past five years have been enjoyable because of my great fellow group members who are like a family to me and an excellent research setting in Marks group. The thank goes to Sharon Koh, Neeraj Saraiya, Matt McCain, and Mike Salata for sharing class experience and graduate school life. I also would like to thank Dr. Neng Guo, Dr. Matt Russell, Sara DiBenedetto, Alex Hains, Dr. Zhiming Wang, Hakan Usta, and Jangdae Youn for their invaluable help and valuable friendship.

I thank my parents, Aiping Li and Yuanzhen Wang, for the enduring love and support that I can feel all the time even being tens of thousands miles away from them.

Finally and most importantly, I thank my wife Dr. Jie Chen for her love, understanding, and for always encouraging me to be my best.

For Dad, Mom, Jie and little Stephanie “Nini”

TABLE OF CONTENTS

LIST OF SCHEMES

CHAPTER ONE

CHAPTER TWO

CHAPTER FIVE

LIST OF FIGURES

CHAPTER ONE

CHAPTER TWO

CHAPTER THREE

CHAPTER FOUR

CHAPTER FIVE

LIST OF TABLES

CHAPTER ONE

CHAPTER TWO

CHAPTER FOUR

CHAPTER FIVE

CHAPTER ONE

Characterization of Transparent Conducting Oxide Surfaces Using Self-Assembled Electroactive Monolayers

1. Introduction

Transparent conducting oxides (TCOs), a fascinating class of materials that are both optically transparent and electrically conductive, are finding increasing application in optoelectronic devices such as flat panel displays (FPDs), organic light-emitting diodes (OLEDs), organic photovoltaics (OPVs), inorganic solar cells, heat reflectors, de-icers, and energy-efficient windows.[1-3] The continuing development of OLED technologies and the interest in significantly improving the efficiency of OPV cells has intensified the need to understand and control the TCO surfaces upon which the active organic thin films are generally deposited.[4-10]

At present, tin-doped indium oxide (ITO) is used in numerous optic-electronic applications as an n-doped, degenerate wide band gap semiconductor because of its excellent transmittance in the visible and near-IR regions, low electrical resistivity, and ease of lithographic processing through chemical etch procedures.[1,11] However, the surfaces of such polar hydrophilic oxides are often chemically incompatible with non-polar organic thin films, leading to delamination of the organic layers and high series resistance in either OLED or OPV cells. The intrinsic TCO chemical incompatibility with many organic materials and the chemical instability of ITO on passing high current densities have led to several solution- and gas-phase pretreatment procedures to control ITO surface energy and work function.[12-15] Other strategies include the addition of thin conductive polymer films,[16,17] deposition of metal-organic species (e.g., zirconium oxides, phenoxytin complexes) with specific surface functionalities,[18,19] chemisorption of organic phosphonic acids[20] via chemical reaction between phosphonic acid groups with ITO surface hydroxyl groups, or addition of cross-linked triarylamine-siloxane injection/adhesion layers (self-assembled monolayers or spin-cast multiple layers, 10-50 nm) to the ITO surface via chemical

reaction between chlorosilyl groups and ITO surface hydroxyl groups.[21,22] ITO electrodes have also seen increasing use as electro-analytical sensors, where rates of electron transfer involving adsorbed or covalently linked molecules are critical for performance.[23,24]

Although ITO has been used widely, the chemical and electronic properties of ITO are far from optimum for current and future applications. There are several drawbacks: (1) the limited availability and high escalating cost of indium;[25] (2) significant absorption in blue region;[26] (3) deleterious diffusion of oxygen and In into proximate organic charge transporting/emissive layers;[27,28] (4) relatively low work function, which causes an energy level mismatch with typical hole transport layer (HTL) materials.[29] Our group has previously developed thermally and chemically stable, highly transparent, high work function ITO-alternative thin film TCO materials, such as metal-organic chemical vapor deposition (MOCVD)-derived doped and undoped CdO[30,31]and Zn-In-Sn-O (ZITO)[32], and ion assisted deposition (IAD)-derived ITO[33] and In_2O_3[34], which partially address the aforementioned deficiencies of ITO. Some of these materials, such as MOCVD-ZITO and IAD-ITO, have already been successfully implemented in OLEDs as effective anodes.[32,33]

To date, there have been a number of studies of ITO surface composition and effective work function, using UV-photoelectron spectroscopy (UPS) and monochromatic X-ray photoelectron spectroscopy (XPS).[12-15] High-resolution XPS studies of ITO surfaces show that there are high concentrations of $In(OH)_3$-like and InOOH-like surface species in the near-surface region. The hydroxyl groups on the ITO surface, especially as $In(OH)_3$-like species, may not be strongly bound to the conductive ITO lattice.[35-37] Furthermore, surface analytical methods such as Kelvin probe,[38,39] photoelectron emission spectroscopy (e.g. UPS, XPS),[12-15, 35-37] and scanning

probe microscopy (AFM, STM)[40-42] may not be effective in unambiguously identifying genuinely organic-inorganic and organic-metal interfacial characteristics, which are thought to be vital for optimizing device response properties,[43,44] because such nanoscale interfacial phenomena are frequently intermingled with bulk properties.

Self-assembled monolayers (SAMs) have been extensively characterized as well-organized arrays of organic molecules on substrate surfaces.[45-49] The formation of organic monolyers by self-assembly is directed by specific interactions between terminal functional groups and the surface. They provide a model system for studying interfacial electron transfer,[50-53] and have been described in applications as diverse as molecular recognition, electrocatalysis, biosensors,[54,55] corrosion protection,[56,57] and molecular electronic devices.[58-60] It is well known that *n*-alkanethiols and *n*-alkyltrichlorosilanes form monolayers on either noble metal or oxidized surfaces, respectively, through self-assembly from dilute organic solutions.[61] In this connection, ferrocene deratives represent an often-studied class of redox-active molecules, and ferrocene-based reagents are frequently used as prototypical redox centers in work demonstrating new techniques or concepts or in studies designed to test specific electron transfer theories. [62]

In this contribution, an approach combining SAMs and the ferrocene functional group is used to characterize the electrochemical properties of various TCO surfaces. In brief, an α, ω-tricholosilyl compound bearing a redox-active group (ferrocene) at one terminus of an alkyl chain is synthesized and then self-assembled to form monolayers on various TCO electrodes via covalent bonds (Scheme 1). It will be seen that a saturated, close-packed monolayer is obtained on as-received ITO after 9 hr, as determined by cyclic voltammetry (CV) and synchrotron X-ray reflectivity (XRR). A full coverage of 6.6×10^{-10} mol/cm^2 is determined by CV. Using this probe

molecule, we then quantitatively characterize the surface reactivity of a diverse series of TCO materials, subjected to selected surface cleaning procedures, with respect to organosilane

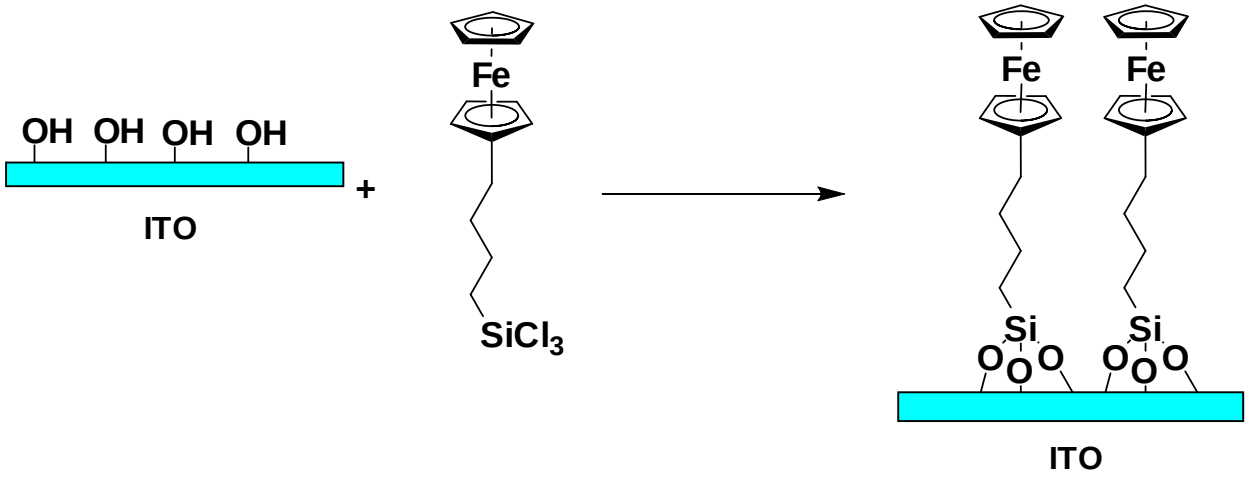

Scheme 1. Scheme for ITO surface modification by a covalently chemisorbed electrochemically-active molecular probe.

condensation chemistry. We believe that the present approach provides a general tool to study the surface electroactivity of TCO electrodes and will aid the development and optimization of TCO materials for organic electronic and opto-electronic applications.

2. Experimental Section

2-1. Materials and Methods. All chemical reagents were used as received unless otherwise indicated. All manipulations of air/moisture-sensitive materials were carried out on a dual-manifold Schlenk line or in a nitrogen-filled glovebox. Ether and THF were distilled before use from sodium/benzophenone ketyl. Toluene was dried using activated alumina and Q5 columns and was tested with benzophenone ketyl in ether solution. Anhydrous MeCN (HPLC grade) was purchased from Sigma-Aldrich and used as received. NMR spectra were obtained on Varian VXR-400 or 500 MHz NMR instruments. MS analyses were conducted on a Micromass Quattro II Triple Quadrupole HPLC/MS/MS mass spectrometer. Elemental analyses were carried out by Midwest Microlabs. Cyclic voltammetry was performed with a BAS 100 electrochemical workstation (SAM-coated TCO films with ~1cm^2 area working electrodes, a Ag wire pseudo-reference electrode, Pt wire counter electrode, 0.1M tetrabutylammonium hexafluorophosphate (TBAHFP) in anhydrous MeCN supporting electrolyte. Scan rate = 0.10 V/s.) TBAHFP was recrystallized from an ethyl acetate/hexanes mixture and dried in vacuo at 100°C for 10 h. Specular x-ray reflectivity experiments on coated single-crystal Si (111) or Si (100) substrates were performed on the Brookhaven National Laboratory X23B beamline at the National Synchrotron Light Source. XPS measurements were performed at Northwestern with an Omicron ESCA probe, which was equipped with EA125 energy analyzer. Photoemission was stimulated by monochromatic Al Kα radiation (1486.6 eV) with an operating power of 300 W, and a low-

energy electron flood gun was employed for charge neutralization. Binding energies of spectra are referenced to the C 1s binding energy set at 284.8 eV. AFM images were obtained on a Nanoscope III AFM under ambient conditions in the contact mode with Si_3N_4 cantilevers having pyramidal tips with 70° cone angles and 20-50 nm radii of curvature. The cantilever had a force constant of 0.12 N/m. The images were obtained using the height mode with a total force of 20-60 nN and a scan rate of ~10 Hz. The same image was scanned at least three times to ensure reproducibility as well as by scanning different area sizes (i.e., higher or lower magnifications) to verify image consistency. All the RMS surface roughness values are reported over an area of 25 μm^2. Quantitative SIMS analysis was carried out on a MATS quadrupole SIMS instrument using a 15 KeV Ga^+ ion source. Advancing aqueous contact angles were measured on a standard goniometric bench fitted with a Teflon micrometer syringe (Gilmont Instrument, Inc.) immediately after the self-assembly process.

2-2. ITO Samples. ITO-coated glass sheets (15 Ω/□, rms roughness = 2 nm) were purchased from Colorado Concept Coating. Commercial ITO substrates were cleaned in an ultrasonic detergent bath, followed by methanol, isopropanol, and finally acetone. The cleaned ITO resulting from this process is termed “as-received ITO” in the discussion below.

2-3. Pretreatments of ITO Surfaces. Following a normal cleaning procedure to produce the as-received ITO surface, two additional pretreatment/cleaning procedures were investigated in this study. The *piranha treatment*, adapted from Wilson and Schiffrin,[63] consisted of three steps: (1) heating the ITO in a 10 mM solution of NaOH for 4 h at 80°C, (2) soaking the ITO in piranha (4:1 H_2SO_4/H_2O_2) for 1 min, and (3) heating the ITO to ca. 160°C for 2 h. The ITO was rinsed

with copious amounts of water between each step. Pretreatment by *oxygen plasma cleaning* was carried out in an oxygen plasma cleaner for 1 min to remove any residual organic contaminants.

2-4. Other TCO Samples. CdO and ZITO (zinc- and tin- doped indium oxide) thin films were grown by low-pressure metal-organic chemical vapor deposition (MOCVD) on Corning 1737F glass substrates as described previously.[30-32] In contrast to simple sputtering, Ion-Assisted Deposition (IAD) is a unique thin-film growth technique which employs two ion beams to simultaneously effect film deposition, oxidation, and crystallization, resulting in smooth, adherent, and dense oxide thin films on various substrates at remarkable low temperature. For comparison, In_2O_3 and Sn-doped In_2O_3 (ITO) thin films were grown by the IAD technique. Prior to the film deposition, the glass substrate was cleaned with the assisted ion beam (Ar ion energy = 100 eV) for ~ 1 min. The In_2O_3 and ITO growth-process details have been reported elsewhere.[33,34] CdO, ZITO, In_2O_3, and IAD-ITO films were cleaned by ultrasonication in successive solutions of detergent, methanol, and isopropanol for at least 30 min each before the self-assembly process.

2-5. Synthesis of 1-ferrocenyl-3-buten-1-ol (1) (Scheme 2).[64] Under an atmosphere of nitrogen, a deep blue SmI_2 solution (0.1 M) was prepared by treatment of Sm (3.31 g, 22 mmol) with 1, 2-diiodoethane (5.07 g, 18 mmol) in anhydrous THF (200 mL) for 2 h at room temperature. To the freshly prepared SmI_2 solution (cooled in ice bath) was added a solution of allyl bromide (2.42 g, 20 mmol) in THF (25 mL). After 10 min, a solution of ferrocenecarboxaldehyde (2.57 g, 12 mmol) in THF (25 mL) was added. The mixture was stirred for 5 h at room temperature, and then quenched by addition of water (10 mL). The mixture was next filtered to obtain a clear solution, followed by extraction with EtOAc (3 × 100 mL). The combined extracts were washed with water (2 × 100 mL) and brine (2 × 100 mL), and dried over

anhydrous Na_2SO_4. Following filtration, solvent was removed in vacuum to yield an orange oil. Chromatography on silica gel with hexane: EtOAc (4:1) afforded 1.23 g of **1** as orange oil. Yield: 40%. ^{1}H NMR ($CDCl_3$, 400MHz): δ 2.09 (1H, d, OH), 2.47 (2H, m), 3.98-4.32 (9H, m), 4.41 (1H, m), 5.12 (2H, m), 5.89 (1H, m).

2-6. Synthesis of 4-ferrocenyl-1-butene (2). Under an atmosphere of nitrogen, a SmI_2 solution (0.1 M) in THF (40 mL) was prepared as described above. A mixture of alcohol **1** (256 mg, 1.0 mmol) and water (216 mg, 12 mmol) in THF (10 mL) was added. The reaction mixture was refluxed at 68 ^{o}C for 0.5 h, cooled, and filtered through a short silica gel column. Following filtration, solvent was removed in vacuum to yield a brown oil. Chromatography on a long silica gel column with hexane afforded 96 mg of **2** as brown oil. Yield: 40%. ^{1}H NMR ($CDCl_3$, 400MHz): δ 2.30 (2H, m), 2.45 (2H, m), 3.98-4.32 (9H, m), 5.12 (2H, m), 5.89 (1H, m). Anal. Calcd for $C_{14}H_{16}Fe$: C, 70.03; H, 6.72. Found: C, 70.42; H, 6.85.

2-7. Synthesis of 1-ferrocenyl-4-trichlorosilyl-butane (Fc-Si$_1$, 3). To a solution of **2** (0.096 g, 0.40 mmol) in 40 mL dry toluene at 25^{o}C under inert atmosphere was added H_2PtCl_6• xH_2O (0.001g), followed by trichlorosilane (0.54 g, 4.0 mmol). The reaction solution was warmed to 55^{o}C and monitored by NMR until completion of the reaction after 24 h. Removal of the solvent in vacuum yielded a yellow solid. Next, 35 mL dry toluene was added to the residue and resulting solution filtered into a dry, clean Schlenk flask by cannula. The crude product was then purified by Kugelrohr distillation. Compound **3** was obtained as yellow solid in 80% yield. ^{1}H NMR (benzene-d_6, 400 MHz): δ 0.90 (2H, t), 1.33 (4H, m), 2.03 (2H, t), 4.00 (9H, m); ^{13}C NMR (benzene-d_6, 400MHz): δ 22.78, 24.44, 29.63, 33.87, 68.05, 6.72, 69.28, 88.97; HRMS Calcd for $C_{14}H_{17}Cl_3FeSi$: 373.95. Found: 373.90.

2-8. Self-assembly of Fc-Si_1 on TCO Substrates. Following strict Schlenk protocol, clean TCO substrates were immersed in a 1.0 mM dry toluene solution of Fc-Si_1 at room temperature for measured times. After the self-assembly process, the toluene solution was removed by cannula and the substrates were rinsed with dry toluene (2 × 50 mL) and acetone in the ultrasonic bath for 3 min each. The treated substrates were then dried at 110°C/100 mmHg in a vacuum oven for 1 h.

2-9. Self-assembly of Fc-Si_1 on silicon substrates. Silicon (111) or (100) substrates (Semiconductor Processing Co.) were subjected to the cleaning procedure that follows. First, the substrates were immersed in "piranha" solution (4:1 H_2SO_4/H_2O_2) at 80°C for 1 h. After cooling to room temperature, the substrates were then rinsed repeatedly with de-ionized (DI) water, followed by an RCA-type cleaning protocol (H_2O: 30% H_2O_2: NH_3; 5:1:1 v/v/v; sonicated at room temperature for 40 min). The substrates were finally rinsed with copious amounts of DI water, heated to 125°C for 15 min, and dried *in vacuo.* Fc-Si_1 was then self-assembled onto the clean silicon substrates following the procedure described above for TCO substrates.

2-10. Self-assembly of Fc-Si_1 on Silicon/ITO substrates. A thin layer (22.5 Å) of ITO film was grown on the clean Silicon (100) substrate by IAD. The growth details have been reported elsewhere.[33,34] Fc-Si_1 was then self-assembled onto the fresh Si/ITO substrates following the procedure described above.

3. Results

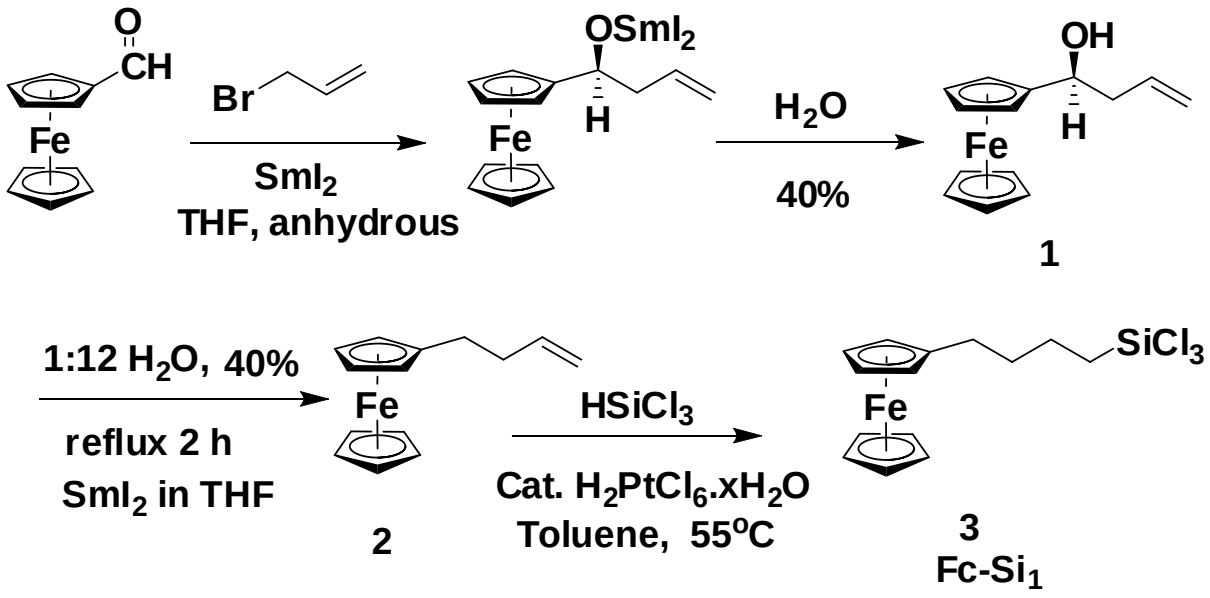

Scheme 2. Synthetic scheme for the electroactive probe molecule, Fc-Si_1.

In this section, the chemisorptive deposition of the Fc-Si_1 molecular probe on TCO or single-crystal substrates is first presented, as well as a discussion of saturation chemisorption of electroactive self-assembled Fc-Si_1 monolayers on as-received ITO. Also presented in this section is the characterization of this saturated self-assembled monolayer on as-received ITO, and then the successful application of this molecular probe to a diverse variety of non-ITO TCO materials to electrochemically characterize the variations in the chemisorptive and electrochemical properties.

3-1. Deposition of Fc-Si_1 on TCO substrates and on single-crystal silicon.

The chlorosilane-tethered probe molecule Fc-Si_1 is self-assembled onto the hydrophilic ITO substrate surfaces with nanoprecise control in thickness, utilizing a self-limiting, solution-based chemisorption process. As illustrated in Scheme 1, clean TCO-coated glass surfaces possess hydroxyl functionalities and chemisorbed water that are reactive toward chlorosilanes, thereby achieving covalent binding of the silane to the surface.[46-49,65] The use of air- and moisture-free deposition conditions is crucial for monolayer formation, preventing the pre-chemisorption oligomerization of Fc-Si_1. Further exposure of the fresh film to air/moisture in the following wet acetone rinse hydrolyzes any unreacted trichlorosilyl groups. Subsequent thermal curing facilitates the formation of a siloxane monolayer, resulting in a thin layer consisting of electrochemically-active moieties covalently anchored to the TCO surface. Deposition of the probe molecule onto single-crystal Si or quartz substrates reasonably proceeds via a similar chemisorption pathway. Thin-film characterization results are presented below.

3-2. Saturation of the electroactive self-assembled Fc-Si_1 monolayers on as-received ITO. Monolayer formation of Fc-Si_1 on as-received ITO and on cleaned single-crystal Si (111) or (100) surfaces was monitored by cyclic voltammetry (CV) and synchrotron x-ray reflectivity

(XRR), respectively. Cyclic voltammograms on ITO vs. chemisorption time are shown in Figure 1A and exhibit the characteristic response of surface-anchored species. Surface coverages of the ferrocenyl absorbate with varing deposition time (Table 1, Figure 1B) are calculated from the integration of the oxidation peak areas (eq 1).[52] Here, Q is the total charge required for oxidation of the bound absorbate, *n* is the number of electrons required for oxidation of a single absorbate molecule, *F* is Faraday's constant, *A* is the total electrode area, and Γ is the surface coverage of the absorbates per unit electrode area. Note here that *A* is the "real" electrode area, which is calculated using the AFM software and the measured RMS roughness of the as-received ITO surface.

$$Q = nFA\Gamma \qquad (1)$$

It is found that the self-assembled monolayer coverage reachs 5.3×10^{-10} mol/cm^2 (80% of the full coverage) after 5 h, and finally achieves a full saturation coverage of 6.6×10^{-10} mol/cm^2 after 9 h. The CV response and coverage of the film after 20 h are identical to those of the film after 9h as shown in Figure 1A, indicating that a saturated and fully-covered monolayer is obtained after 9 h.

The cyclic voltammetry curves obtained with sweep rates from 0.1 to 10 V/s for the saturated Fc-Si_1 monolayer on as-received ITO are shown in Figure 2. At a scan rate of 0.1 V/s, the oxidation/reduction line shapes are nearly symmetrical for the Fc-Si_1-based SAM-coated ITO electrode, indicating that the rate of electron transfer is rapid on the time scale of the experiment.[74] However, as the scan rate is increased, the redox peak potentials shift symmetrically in positive and negative directions, with broader peak shapes and greater separation between oxidation and reduction peak potentials, indicating that the electron transfer rate is less competitive at more rapid sweep rates.[75] The redox peak potentials ($E_{p,a}/E_{p,c}$) and maximum

widths at half-height of the oxidation peak ($\Delta E_{p,a,\,1/2}$) are summarized in Table 2. The electron-transfer rate for this surface-confined redox species on ITO is 6.65 s^{-1}, calculated as outlined by Laviron.[76]

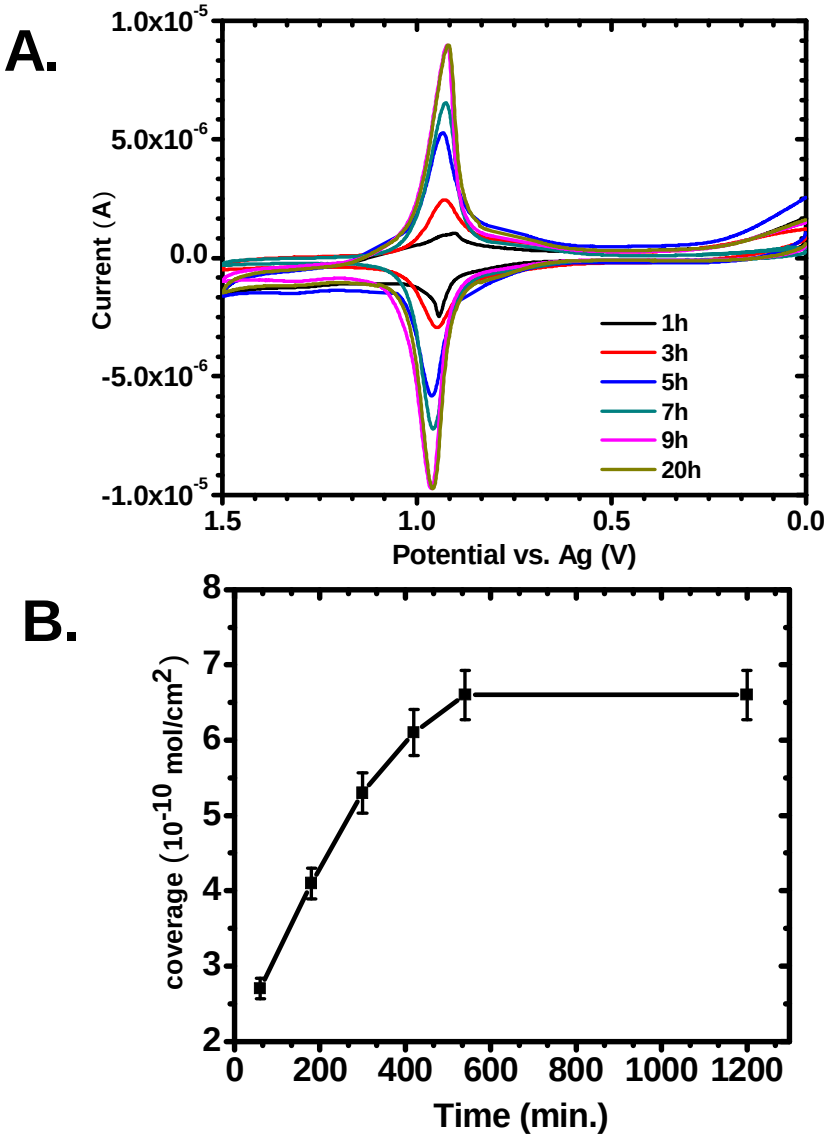

Figure 1. (A) Cyclic voltammograms of redox Fc-Si_1-based SAMs on as-received ITO vs. deposition time at a 0.1 V/s sweep rate. (B) Surface coverage of Fc-Si_1-based SAMs on as-received ITO vs. deposition time.

Deposition Time	1 h	3 h	5 h	7 h	9 h	20 h
Coverage ($\times 10^{-10}$ mol/cm^2)	2.7 ± 0.14	4.1 ± 0.21	5.3 ± 0.27	6.1 ± 0.31	6.6 ± 0.34	6.6 ± 0.40
Footprint for One Molecule (Å^2)	62	41	32	28	25	25
Aqueous Contact Angle(°)	47	60	71	80	90	90

Table 1. Surface coverages and advancing aqueous contact angle measurements on self-assembled Fc-Si_1 films on as-received ITO electrodes with various deposition times.

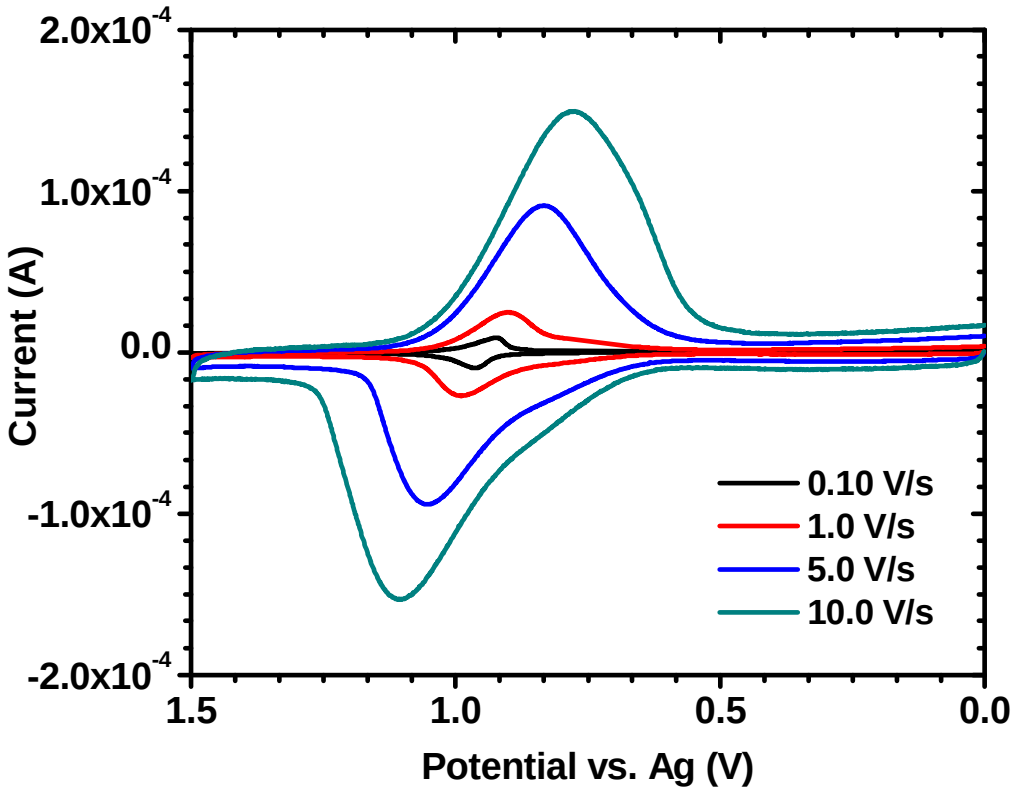

Figure 2. Cyclic voltammograms of the saturated Fc-Si_1-based SAM on as-received ITO with various sweep rates from 0.10 to 10.0 V/s.

Sweep rate	0.10 V/s	1.0 V/s	5.0 V/s	10.0 V/s
$E_{p,a}/E_{p,c}$ (V)	0.963/0.923	0.991/0.901	1.054/0.834	1.111/0.779
$\Delta E_{p,c,\,½}$ (V)	0.092	0.137	0.230	0.285
$\Delta E_{p,a,\,½}$ (V)	0.095	0.145	0.221	0.282
Ep,a-Ep,c (V)	0.040	0.090	0.220	0.332

Table 2. Cyclic voltammetric characteristics of self-assembled Fc-Si_1 films on as-received ITO electrodes with various sweep rates.

Advancing aqueous contact angle (CA) measurements (Table 1) reveal that the surface of the densely packed Fc-Si_1 monolayer is markedly hydrophobic, as evident from the observed maximum CA, $\theta_a \approx 90°$. The large wettability difference of $\Delta\ \theta_a \approx 70°$ between the hydrophilic ITO substrates and the fully functionalized substrates should allow reliable ex situ monitoring of the film formation versus reaction time. A rapid change from θ_a ~20° to ~47° in the surface polarity is observed during the first hour of the assembly process; the aqueous CA reaches a maximum after ~9 h, in accord with the formation of a densely packed film indicated by CV results, and then remains constant ~90° after 9 h.

Specular X-ray reflectivity (XRR) measurements were performed on Fc-Si_1 SAMs deposited on clean, single-crystal Si(111) or Si(100) surfaces with native SiO_2 coverage, using the self-assembly procedure described in the Experimental Section. By fitting of the X-ray reflectivity data, normalized to the Fresnel reflectivity, to a physically reasonable model, the specular time-dependent XRR studies provide fundamental information on the: (i) film thickness, (ii) surface morphology/roughness (= $\sigma_{film\text{-}air}$), (iii) electron density distribution perpendicular to the substrate surface, and (iv) surface coverage/probe footprint. In general, the reflectivity can be expressed in terms of the average electron density by eqs (2) and (3), [66]

$$R(k_z) = R_F(k_z)|\ \Phi(k_z)|^2, \qquad (2)$$

$$\Phi(k_z) = \int \frac{1}{\rho_\infty} \frac{d\langle\rho\rangle}{dz} e^{ik_z z}\, dz\,, \qquad (3)$$

where R_F is the theoretical Fresnel reflectivity for a smooth interface, k_z is the momentum transferred ($k_z = 4\pi/\lambda \sin\theta$), $d\langle\rho\rangle/dz$ is the derivative of the electron density along the surface normal direction, averaged over the in-plane coherence length of the x rays, and ρ_∞ is the electron density of the substrate (Si). The details of the XRR-data analysis procedure are described

elsewhere.[67-70] By fitting the XRR data for the self-assembled Fc-Si_1 film on Si/SiO_2, the thickness, electron density, molecular footprint, and roughness are determined. These data are compiled in Table 3. Here, the surface coverages are calculated as follows: first, the film electron density per unit substrate area, N_{film}, is calculated using electron density profiles obtained from the measurements. Then, the molecular footprint dimensions are calculated as $N_{mol}/N_{film,}$ where N_{mol} is the calculated number of electrons in one molecular unit. Finally, surface coverages are derived by dividing the unit substrate area by the molecular footprint.

The XRR data (Figure 3B) also show that the thickness and roughness of the metal-organic film (Fc-Si_1) on Si/ITO are 1.80 ± 0.09 nm and 0.20 ± 0.03 nm, respectively. The thickness and roughness of the IAD-derived ITO film on Si surface are 2.25 ± 0.31 nm and 0.70 ± 0.5 nm, respectively.

3-3. Characterization of electroactive Fc-Si_1-based SAMs on as-received ITO.

Atomic Force Microscopy. AFM images of the self-assembled ferrocenyl siloxane films on as-received ITO substrates are essentially indistinguishable from the bare ITO substrate image with no indication if island growth, film cracking, or pitting (Figure 4). The rms roughnesses of bare as-received ITO and Fc-Si_1 films on ITO were determined to be 2.13 and 1.56 nm, respectively. This argues that the present self-assembly process is capable of depositing smooth, conformal siloxane films with some degree of ITO substrate planarization.

Deposition Time (Hrs)	Electron density ρ_{film} ($eÅ^{-3}$)	Roughness σ_{film} (Å)	Thickness (Å)	Footprint $(Å)^2$	Coverage ($\times 10^{14}$ molecules/cm^2)	Coverage ($\times 10^{-10}$ mol/cm^2)
1	0.42-0.45	3.2 ± 0.1	7.6 ± 0.2	48 ± 2.5	2.1 ± 0.11	3.5 ± 0.18
5	0.42-0.45	4.0 ± 0.1	12.7 ± 0.3	30 ± 1.6	3.3 ± 0.17	5.5 ± 0.28
9	0.42-0.45	4.1 ± 0.2	13.5 ± 0.3	27 ± 1.4	3.7 ± 0.19	6.2 ± 0.31
20	0.42-0.45	6.3 ± 0.3	15.5 ± 0.5	27 ± 1.4	3.7 ± 0.19	6.2 ± 0.35
On Si/ITO Surface 15	0.42-0.45	2.0 ± 0.3	18.0 ± 0.9	25 ± 1.6	3.88 ± 0.24	6.50 ± 0.40

Table 3. X-ray reflectivity characterization of self-assembled Fc-Si_1 films on single-crystal Si (100) and Si (100)/ITO substrates with various deposition time.

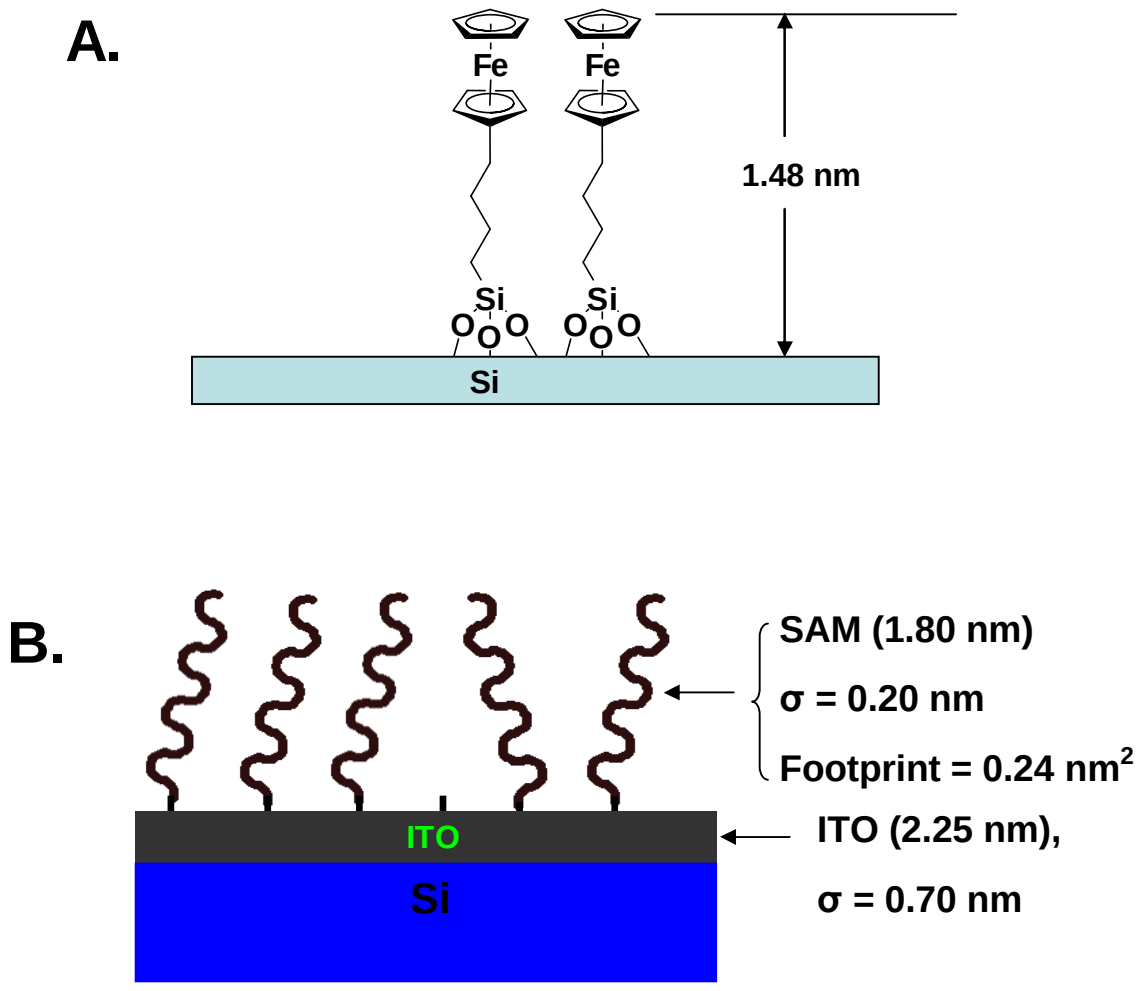

Figure 3. (A) Fc-Si_1 molecules self-assemble onto as-received ITO substrates. The semiempirical PM3 energy-minimized structure of hydrolyzed Fc-Si_1 has a molecular height of 1.48 nm. (B) A thin layer of ITO with 2.25 nm thickness grown on the Si (100) surface by the IAD technique. The probe molecule Fc-Si_1 is then self-assembled on the Si (100)/ITO surface with a 1.8 nm thickness and 0.2 nm roughness from the XRR data.

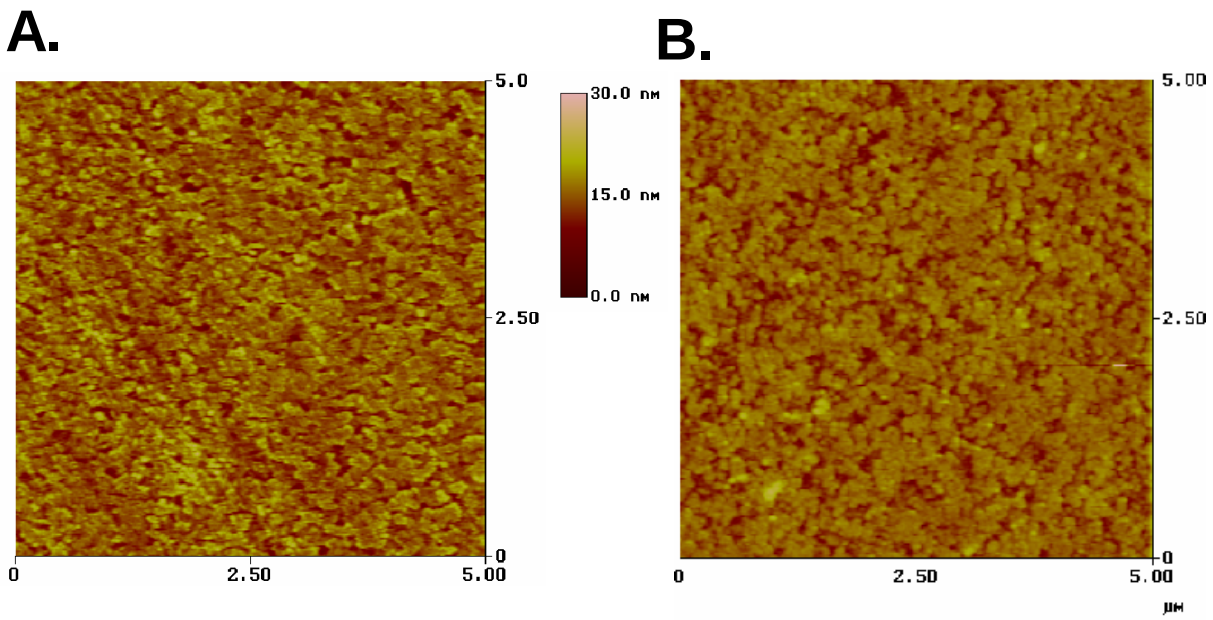

Figure 4. Tapping mode AFM images of: (A) Bare as-received ITO. RMS roughness = 2.13 nm. (B) Fc-Si_1 SAM self-assembled on the ITO surface. RMS roughness = 1.56 nm.

X-ray Photoelectron Spectroscopy. Figure 5 shows XPS spectra of bare ITO and Fc-Si_1 SAM/ITO surfaces. There is a clear decrease in both the In (3d) and Sn (3d) features, and an increase in the Si (2p), Si (2s) and Fe (2p) intensities on SAM deposition, which is attributable to the ferrocenyl functional group and Si-O linkages. With the self-assembled monolayer coverage, the In (3d) intensity decreases by ~50% with respect to the bare surface, as anticipated for a conformal film, where the emitted photoelectrons have a kinetic energy of ~1000eV (Al Kα excitation), hence an inelastic mean free path of ~30 Å.[73] The characteristic signatures of Cl (2p) photoelectrons at 200 eV[20] are below the detection limit, indicating completion of the silane hydrolysis/condensation. The O (1s) and C (1s) signals arise from the oxide, the alkyl chain, and adventitious carbon, and are therefore not useful in this characterization.

Second Ion Mass Spectrometry. The SIMS spectrum of the Fc-Si1-based SAM/ITO surface also confirms the elemental composition (Figure 6A). The peaks of new elements and organic/organometallic species, such as Fe (mass = 56), C_5H_5Fe (mass = 121), and $C_9H_{12}Si$ (mass = 147), can be clearly detected in the SIMS positive ion spectrum. The elements Na, K, In, and Sn are mapped to obtain the total ion image of the bare, as-received ITO (Figure 6B). In the total ion image of the redox Fc-Si_1-based SAM/ITO surface, all elements and organic/organometallic species, including Fe, Si, Na, K, In, Sn, C_5H_5Fe, and $C_9H_{12}Si$, are mapped. The change in color of the plotted total ion image from yellow to red is due to the new elemental and organic/organometallic species present on the Fc-Si_1-based SAM/ITO surface. From the image of the total ions on the surface determined using SIMS, it can be seen that the Fc-Si_1-based self-assembled monolayer coverage is spacially uniform on ITO at this level of resolution.

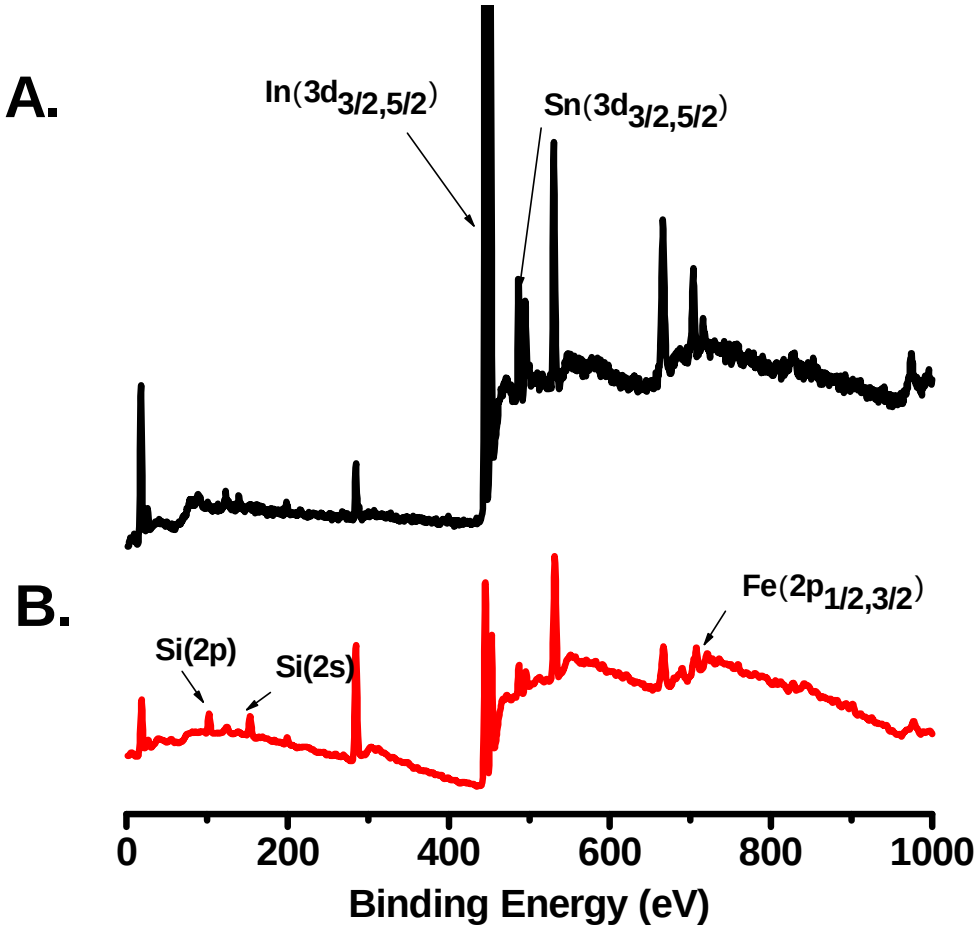

Figure 5. X-ray photoelectron spectroscopy of: (A) the bare ITO substrate and (B) the redox Fc-Si_1-based SAM self-assembled on the ITO surface.

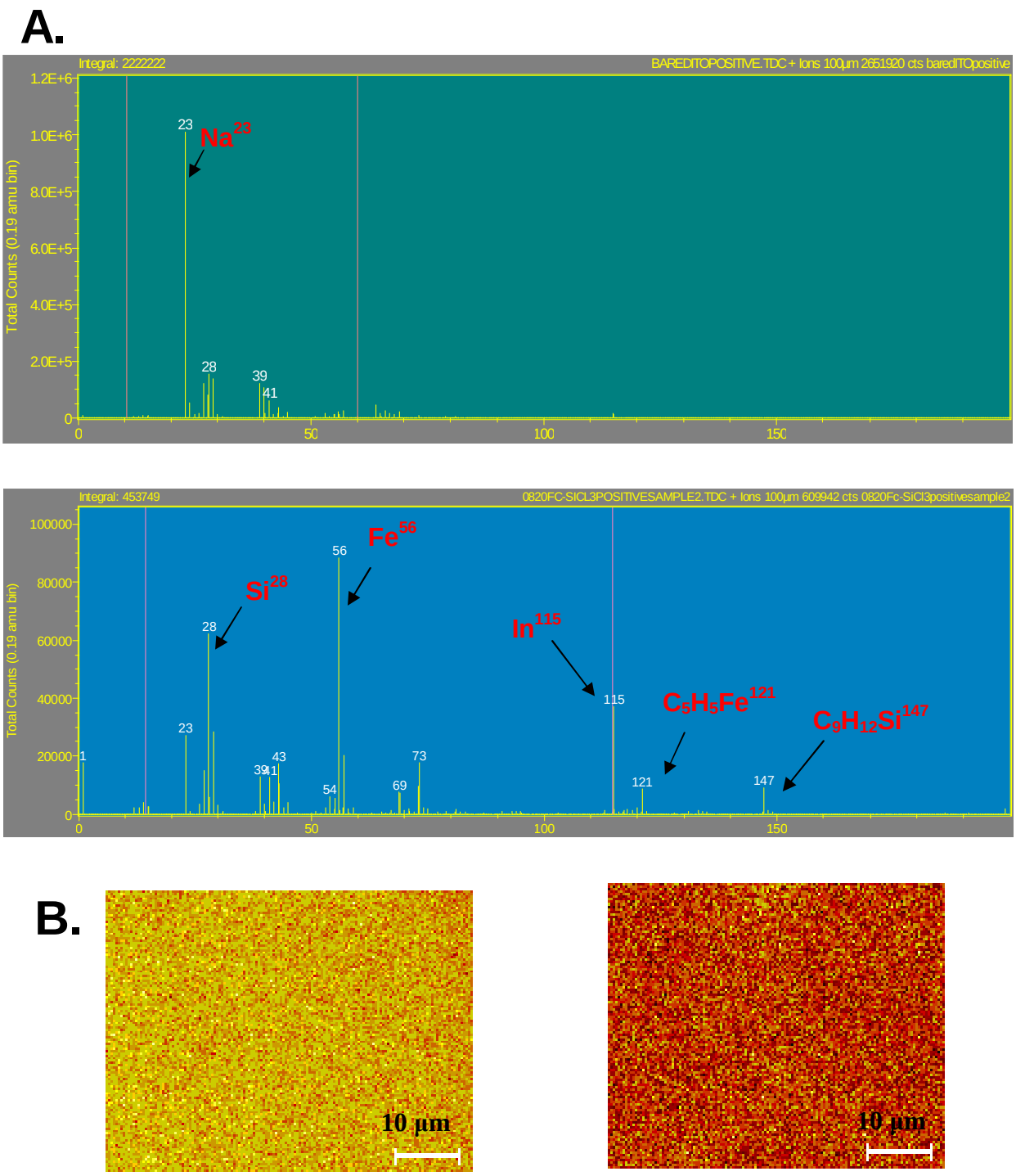

Figure 6. (A) SIMS positive ion spectrum of bare, as-received ITO (upper) and the Fc-Si_1-based SAM on the ITO substrate (lower). (B) Images of the total ions on the bare, as-received ITO surface (left) and the Fc-Si_1-based SAM/ITO surface (right).

3-4. Electrochemical property variations of ITO/Fc-Si_1 surfaces induced by different ITO surface pretreatments.

The probe molecule Fc-Si_1 was next self-assembled onto a series of ITO substrates subjected different surface pretreatments: chemical cleaning, piranha treatment, and oxygen plasma cleaning. Note here that the self-assembly time is held constant at 15 h to reasonably ensure formation of optimally saturated monolayers on the ITO surfaces. Figure 7 and Table 4 summarize the electrochemical data for the chemisorbed, saturated Fc-Si_1-based SAMs on the various ITO samples at a 0.1 V/s scan rate. The O_2 plasma-treated ITO shows the highest surface coverage of ferrocene adsorbate (7.9×10^{-10} mol/cm^2) and highest electron-transfer rate (9.23 s^{-1}), versus the lowest electroactive site coverage (5.1×10^{-10} mol/cm^2) and lowest electron-transfer rate (4.79 s^{-1}) on the piranha-treated ITO.

3-5. Electrochemical properties of non-ITO TCOs.

Cyclic voltammograms of the saturation coverage Fc-Si_1-based SAMs, obtained after a 15 h self-assembly process as described in Experimental Section, on as-received ITO, MOCVD-derived CdO and ZITO, and IAD-derived ITO and In_2O_3, are shown in Figure 8 (0.1 V/s scan rate). Relevant properties of these TCOs and electrochemical data are summarized in Table 5. It is expected that SAMs fabricated with the same redox probe molecule (Fc-Si_1) on various TCO surfaces will give rise to differing film microstructures and electrical/electrochemical properties. Indeed, this is observed in the thin-film CV characterization data presented here. First, different types of TCO lattices and surfaces profoundly affect the redox-SAM microstructure, as indicated by the different voltammetric behavior (e.g. $E_{p,a}$ and $E_{p.c}$, Table 5). These differences in apparent redox potentials and electron transfer rates doubtless arise in part from heterogeneity in

chemisorption sites and relative stability of the redox molecules chemisorbed on these sites. Second, the redox-active SAMs may have differing intermolecular interactions between neighboring ferrocene cores on the different surfaces. Cyclic voltammetry of the SAMs on the different TCO electrode surfaces at room temperature reveals that the full width at half-height of the oxidative wave ($\Delta E_{p,\,½}$) at a slow sweep rate (0.1 V/s) is 93 mV (as-received ITO), 96 mV (CdO), 94 mV (ZITO), 90 mV (IAD-ITO), and 165 mV (IAD-In_2O_3). These results argue that the intermolecular interactions of the redox SAMs on as-received ITO, CdO, ZITO and IAD-ITO are generally rather similar. However, the SAM on IAD-In_2O_3 shows the largest $\Delta E_{p,\,½}$ (165 mV), which suggests large intermolecular interactions/heterogeneity among the bound redox molecules on the IAD-In_2O_3 surface. Further comments about the effect of intermolecular interaction on rates of heterogeneous electron transfer are made below. Additionally, surface coverages of the redox ferrocene absorbate on various TCO films, determined from cyclic voltammetry measurements, follow the order: CdO (8.1×10^{-10} mol/cm^2) > ZITO (7.6×10^{-10} mol/cm^2) > IAD-ITO (7.2×10^{-10} mol/cm^2) > IAD-In_2O_3 (6.7×10^{-10} mol/cm^2) > as-received ITO (6.6×10^{-10} mol/cm^2). Note here that the "real" electrode area A is used to calculate the surface coverage, which in turn is calculated using the AFM software and the RMS roughnesses of the various TCO films.

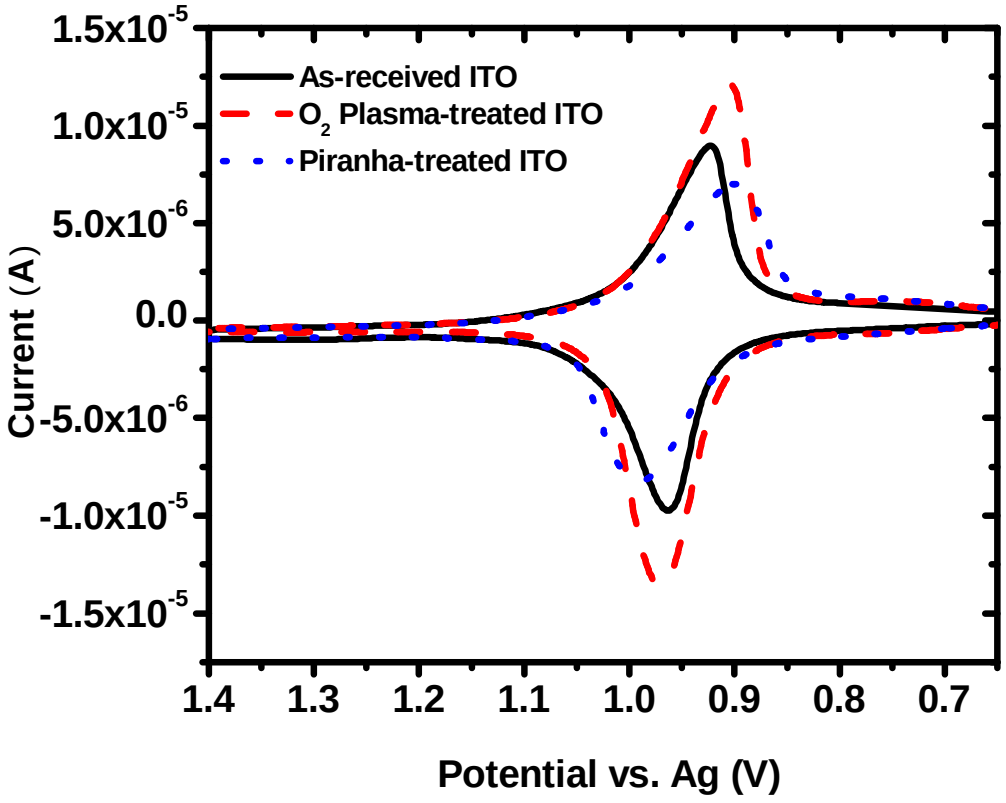

Figure 7. Cyclic voltammograms of the redox Fc-Si_1-based SAM (self-assembly time = 15 hr) on various ITOs treated by different cleaning protocols at a 0.10 V/s scan rate.

ITO Treatment	$E_{p,a}/E_{p,c}$ (mV)	$\Delta E_{p,½}$ (mV)	Coverage (mol/cm^2)	Footprint (Å^2)	Electron-transfer rate (s^{-1})
As-received ITO	963/923	93 ± 2	6.6×10^{-10}	25	6.65
O_2 Plasma	973/905	95 ± 3	7.9×10^{-10}	21	9.23
Piranha	993/900	100 ± 1	5.1×10^{-10}	32	4.79

Table 4. Cyclic voltammetry characteristics of self-assembled Fc-Si_1 films on various ITO electrodes treated with different cleaning protocols at a 0.1 V/s scan rate.

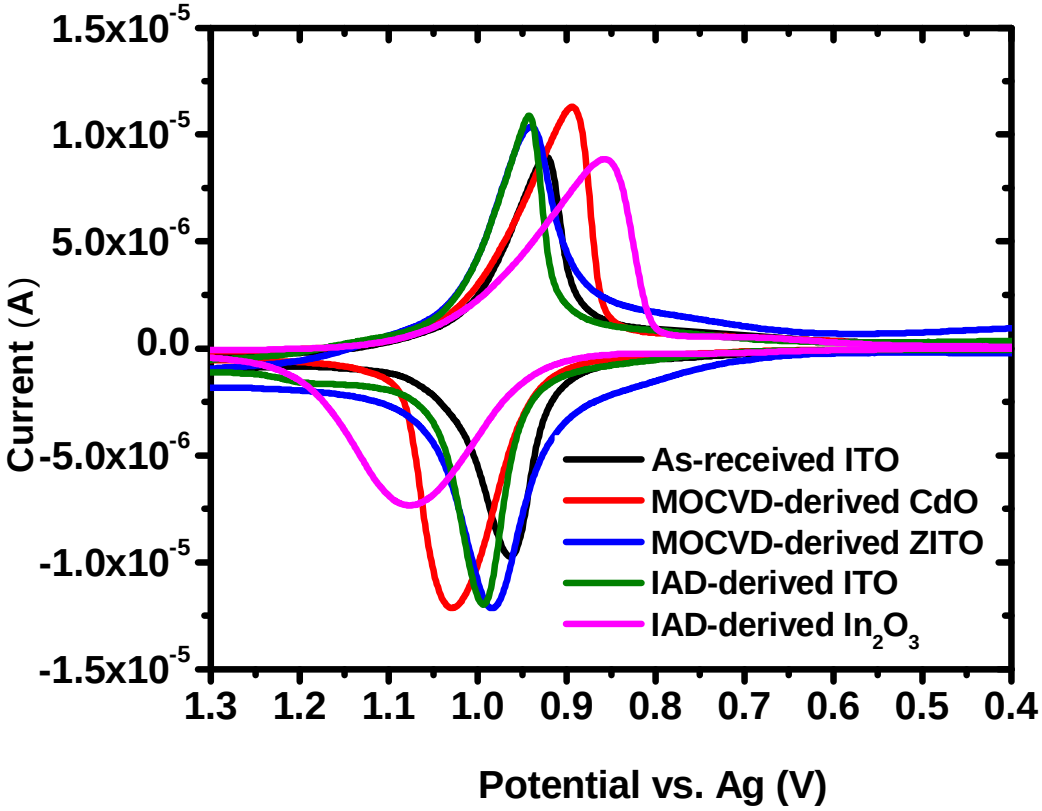

Figure 8. Cyclic voltammograms of Fc-Si_1-based SAMs (self-assembly time = 15 h) chemisorbed on various TCO surfaces at 0.1 V/s scan rate.

TCOs	Thick-ness (nm)	Conduc-tivity (S/cm)	Sheet resistance (Ω/□)	Roughness (nm)	$E_{p,a}$/ $E_{p,c}$ (mV)	ΔE_p (mV)	$\Delta E_{p,\,½}$ (mV)	Coverage (mol/cm^2) × 10^{-10}	Electron-transfer rate (s^{-1})
As-received ITO	130	5000	18	2	963/ 923	40	93 ± 2	6.6	6.65
MOCVD-derived CdO	300	5500	13	6	1028 /894	134	96 ± 1	8.1	0.42
MOCVD-derived ZITO	200	2500	24	5	984/ 944	40	94 ± 3	7.6	7.12
IAD-derived ITO	250	1400	29	1.1	994/ 942	52	90 ± 2	7.2	5.07
IAD-derived In_2O_3	220	1000	49	1.8	1076 /859	217	165 ± 2	6.7	0.03

Table 5. Relevant properties of various TCOs and cyclic voltammetry characteristics of self-assembled Fc-Si_1 films on various TCO surfaces at a 0.1 V/s scan rate.

4. Discussion

4-1. Saturation of the electroactive self-assembled Fc-Si_1 monolayers on as-received ITO.

The XRR data reveal an initial film thickness of ~0.76 nm after a 1.0 hour deposition time, which increases to ~1.27 nm during the next 5 hours. The film thickness reaches a maximum of ~1.35 nm after a 9 hour deposition time. PM3-level calculations indicate a theoretical molecular length of ~ 1.48 nm for the ferrocenyl siloxane film (Figure 3A), suggesting that the molecules must be tilted with respect to the surface normal. In time, the interplay between entropic (conformational and orientational degrees of freedom of the deposited molecules within the film) and enthalpic (additional incorporation of probe molecules into the film) factors ultimately leads to a preferred alignment of the probe molecules in the direction perpendicular to the substrate surface. The estimated average tilt angle varies from ~30° after a 1 h to ~65° after a 9 h deposition time (reasonably assuming that Fc-Si_1 the molecule behaves as a rigid rod). Similar tilt angles have been observed for self-assembling adsorption of fluorinated chlorosilanes on Si (100) substrate.[92] Note here that for a 20 h deposition time, the XRR-derived film coverage is identical to that of a 9 h deposited film, whereas the measured film thickness of ~1.5(5) nm is ~0.2 nm greater than that of a 9 h deposited film, which is due to the greater roughness ($\sigma_{film\text{-}air}$) of 0.22(1) nm (= 0.63(3) nm – 0.41(2) nm). That film thicknesses derived from XRR are less than or equal to the length of the self-assembled molecule computed by PM3 provides strong support for the contention that the layer self-assembled on ITO is largely if not exclusively a monolayer rather than a multilayer, and thus the CV-derived surface coverage of 6.6(4) × 10^{-10} mol/cm^2 represents essentially full monolayer coverage. Here we attribute any difference between the CV-derived full monolayer coverage of 6.6(4) × 10^{-10} mol/cm^2 on ITO and XRR-derived full coverage of 6.20(35)

$\times 10^{-10}$ mol/cm^2 on Si(100) to the differing nature of the respective substrate surfaces. The surface of single-crystal Si(100) (rms roughness = ~0.20 nm) is flatter, smoother, and has lower hydroxyl group coverage than does the ITO surface (rms roughness = ~2.0 nm). To obtain direct monolayer growth information on ITO substrates by XRR, a thin layer (2.25 nm) of ITO was grown on the Si(100) surface by IAD, and then the probe molecule Fc-Si_1 was self-assembled on the ITO surface. The XRR data (Figure 3B, Table 3) show that the thickness and roughness of the metal-organic film are 1.80(9) nm and 0.20(3) nm, respectively. The greater film thickness than the computed molecular length of the molecule is reasonably ascribed to the relatively rougher IAD ITO surface (rms roughness = ~0.70 nm), compared with that of the single crystal Si surface (rms roughness = ~0.20 nm).

The CV-derived fully-covered monolayer coverage of the present ferrocenyl trichlorosilane probe (Fc-Si_1; 6.6(4) $\times 10^{-10}$ mol/cm^2) is somewhat greater than the reported surface coverage of ferrocene dicarboxylic acid on ITO (4.5(5) $\times 10^{-10}$ mol/cm^2)[37,71], which suggests that the layers formed by carboxyl –terminated molecules on ITO are not as compact as those formed by the organosilane.[71] The Fc-Si_1 self-assembled monolayer strongly adheres to the hydrophilic substrate via covalent Si-O- bonds and cannot be easily detached by sonication or leached by organic solvents. The stability of the chemisorbed materials at the electro-active sites is further revealed by the fact that three consecutive scans produce almost identical voltammograms with only minor loss of the originally chemisorbed material (Figure 9). This result is in contrast to that for $Fc(COOH)_2$ chemisorbed on ITO through hydrogen-bonding interactions with surface hydroxyl groups. The latter system loses 20~25% of the chemisorbed $Fc(COOH)_2$ during the first oxidation/reduction cycle.[37a] Since organosilane-derived reagents can form conformal, smooth, contiguous, covalently coupled, pin-hole free, and electroactive monolayers by self-assembly, they

have been successfully used in OLED and OPV devices.[20-22,37,72] In both cases, modification of ITO surfaces with electroactive organosilane compounds provides enhanced wettability of organic active layers on the polar ITO surface, better matched work functions, and enhanced electrical contact between ITO anodes and organic active layers, as assessed by OLED hole-only devices[22] and OPV series resistance, *R*s data.[37,72]

For ideal Nernstian electrochemical reactions of identical, independent, anchored redox site ensembles at room temperature, $\Delta E_{p,\,½}$ of either of the symmetrically disposed cathodic or anodic peaks is expressed as in eq. 4,[77]

$$\Delta E_{\,p,\,½} = 90.6/n \text{ mV} \qquad (4)$$

Deviation from this ideal behavior, seen as broadening or distortion of the electrochemical waves, often indicates redox site-site interactions, and/or site heterogeneity.[74,75,78] The symmetrical voltammetry characteristics seen in Figure 2 at slow sweep rates indicate that the electron transfer between immobilized ferrocene cores and the electrode is rapid and reversible on the timescale of the experiment. Quantitatively, the value of $\Delta E_{\,p,\,½}$ is related to $g = \alpha_o + \alpha_R - 2\alpha_{OR}$, where α_o, α_R, α_{OR} are the interaction parameters for oxidative site-oxidative site, reductive site-reductive site, and oxidative site-reductive site interactions, with $\alpha > 0$ for attractive interactions; $\alpha < 0$ for repulsive ones. When $g = 0$, $\Delta E_{\,p,\,½} = 90.6/n$; when $g < 0$, $\Delta E_{\,p,\,½} > 90.6/n$.[77] Qualitatively, stronger redox site-redox site interactions result in larger deviations of $\Delta E_{\,p,\,½}$ from the ideal value.[79,80] The present full widths at half-height of the cathodic ($\Delta E_{\,p,c,\,½}$) and anodic ($\Delta E_{\,p,a,\,½}$) peaks are 92 mv and 95 mv at a 0.1 V/s scan rate, respectively. This is slightly larger than 90.6/*n* (*n* = 1) mV, which suggests some degree of redox site-redox site interaction and/or heterogeneity in the chemisorption sites.

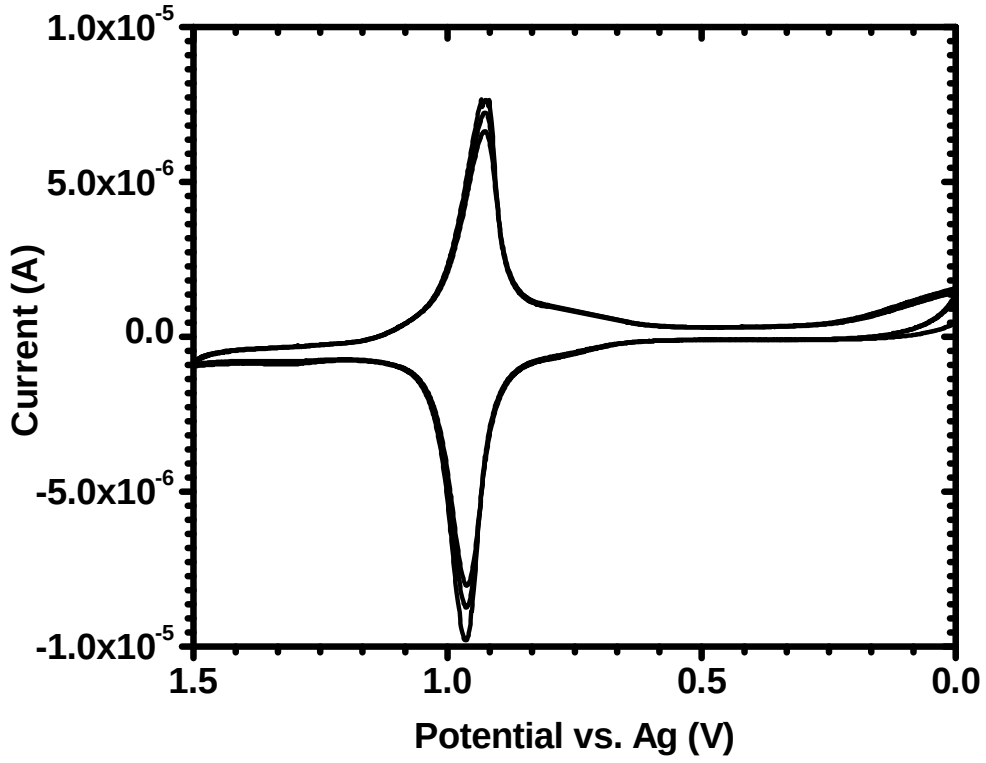

Figure 9. Cyclic voltammograms of a saturated Fc-Si_1-based SAM on as-received ITO at a 0.1 V/s sweep rate over 3 consecutive scans.

4-2. Electrochemical property variations of ITO samples induced by different surface pretreatments.

O_2 plasma-treated ITO shows the highest surface coverage of ferrocene absorbate (7.9 $\times 10^{-10}$ mol/cm^2) and highest apparent electron-transfer rate (9.23 s^{-1}), which may be attributed to the O_2 plasma being effective in removing a thin layer of insulating carbon-rich materials from the ITO surface, thereby increasing the conductance and improving the uniformity as reported by Liau and co-workers.[81] In contrast, piranha-treated ITO exhibits the lowest electroactive site coverage (5.1×10^{-10} mol/cm^2) and lowest electron-transfer rate (4.79 s^{-1}), which was also observed by Donley et al.[37d] This result strongly suggests that piranha-treated ITO samples may contain a large density of unstable surface hydroxides such as $In(OH)_3$-like species, which are not tightly incorporated into the ITO lattice, and the chemisorbed Fc-Si_1 may then be easily removed from the surface along with these sites during sonication, initial contact with electrolyte, or repeated cycling. These results also suggest that such ITO surfaces may contain electrochemical "hot spots" and electrochemical "dead regions", and that the hydrolysis products of the ITO surface, especially $In(OH)_3$-like species, my not be strongly bound to the metal oxide lattice.

4-3. Electrochemical properties of non-ITO TCOs.

Surface coverages of the ferrocene redox adsorbate on various TCO films, determined from cyclic voltammetry measurements, follow the order: CdO > ZITO > IAD-ITO > IAD-In_2O_3 > as-received ITO. Note here that the surface coverage of the redox molecule on CdO is ~ 20% greater than the coverage on as-received ITO, which may reflect the more conductive CdO film having fewer electrochemical "dead regions". ITO films produced by the IAD growth technique are much smoother and denser than the ITO films grown by other techniques, this may

give rise to more dense –OH group surface coverage, thus enhancing the surface coverage of ferrocenyl absorbate.

Cyclic voltammetry of the saturated, redox SAMs on the various TCO electrodes (scan rate = 0.1 V/s) reveals E_{ox}/E_{red} peak separations (ΔE_p) increasing in the order: 40 mV (ZITO) = 40 mV (as-received ITO) < 52 mV (IAD-ITO) < 134 mV (CdO) < 165 mV (IAD-In_2O_3). Such data can be used to estimate interfacial electron transfer rates for strongly absorbed redox-active sites.[76,82-84] In general, the observed peak potential separation depends on the relative scan rates and electron transfer rates. All other factors being equal, larger peak separations qualitatively correlate with slower interfacial electron transfer. Indeed, the calculated heterogeneous electrochemical electron-transfer rates between redox SAMs and the various TCO electrodes follow the order: 7.12 s^{-1} (ZITO) > 6.6 s^{-1} (as-received ITO) > 5.07 s^{-1} (IAD-ITO) > 0.42 s^{-1} (CdO) > 0.03 s^{-1} (IAD-In_2O_3). Note here that the electron-transfer rate of IAD-In_2O_3 is nearly two orders of magnitude less than the electron-transfer rate of as-received ITO, which may also reflect strong intermolecular interactions of the Fc-Si_1 sites on the IAD-In_2O_3 surface and the low TCO conductivity of 1000 S/cm. Because the carrier mobility is lower in semiconducting electrodes versus that in commonly used metal electrodes, a non-negligible lag is expected between the potential at the voltage source and that at the electrode/Fc-Si_1 SAM interface. Since all potentials experience this "lag", the peaks are shifted to more extreme potentials, thus giving the CV a well-documented stretched appearance.[93-95]

In the scenario of surface-confined redox couples, the electron-transfer rate between the redox species and an electrode can be described in a simplified form (eq. 5),[62a,75, 85,86]

$$k_{et} = \exp[-(\lambda + \Delta G°)^2/4\lambda RT] \qquad (5)$$

where λ is the reorganization free energy, and ΔG° is the reaction free energy and equal to *e* (E-E^0) (*e* is the electron charge, E is the electrode potential, and E^0 is the formal potential of the redox couple[62a]). Generally, electron transfer between a redox couple and an electrode is described via a superexchange interaction[87] where electronic coupling is dominated by through-bond electron tunneling.[88] The effect of intermolecular interactions on electron transfer involving SAMs is often observed in electrochemical studies,[77,89] and is attributable to intermolecular electronic coupling which also affects the electron-transfer rates.[84,88] In addition, the redox SAMs on various TCO surfaces may have different reorganization energies, which should also affect electrochemical electron transfer rates, as described by Marcus theory.[90,91] The present results on SAM electrochemical properties on various TCO surfaces suggest new criteria for evaluating TCO materials as alternative anodes to ITO in OLEDs and organic thin film OV cells, such as high electro-active surface coverage and rapid electron-transfer rates between adsorbed monolayers of organic small molecules/polymers and the anode surface. It was observed in our previous work that OLEDs containing ITO/SAM/HTL (hole-transporting layer) configurations with a series of silyltriarylamine SAMs, have dramatically varied hole-injection magnitudes and OLED responses, which can be correlated with electrochemically-derived heterogeneous electron-transfer rates for the same triarylamine fragments.[22b]

5. Conclusions

An electrochemically-active small molecule has been designed, synthesized at high yield, and self-assembled onto the "universal" transparent electrode, ITO, and other TCO surfaces as a molecular probe, forming a nanometer-scale monolayer. A saturated redox SAM with a surface coverage 6.6×10^{-10} mol/cm^2 is obtained at room temperature after 9 hr reaction in a 1mM self-

assembly solution. Methods combining cyclic voltammetry, synchrotron X-ray reflectivity, AFM, SIMS, XPS, and advancing aqueous contact angle have been applied to characterizing the self-assembled redox monolayer. The redox SAM probes chemisorption process on various TCO surfaces, the presence of "dead layers", and how this varies with TCO identity, surface cleaning protocol etc. Results show that O_2 plasma-treated ITO exhibits the greatest surface coverage of the ferrocene absorbate (7.9×10^{-10} mol/cm^2) and the greatest electron-transfer rate (9.23 s^{-1}) among different pretreatment treated ITOs. Furthermore, it is demonstrated that MOCVD-derived CdO shows the greatest surface electro-active coverage (8.1×10^{-10} mol/cm^2), and MOCVD-derived ZITO shows the greatest electron transfer rate (7.12 s^{-1}) among five TCOs. The slowest electron-transfer rate (0.03 s^{-1}) between the redox SAM and a TCO electrode (IAD-derived In_2O_3) is explained by large intermolecular interactions and heterogeneity within the chemisorbed redox SAM and the low In_2O_3 conductivity.

CHAPTER TWO

Air-Stable, Cross-Linkable Hole-Injecting/Transporting Interlayers for Improved Charge Injection in Organic Light-Emitting Diodes

1. Introduction

Small-molecule and polymer organic light-emitting diodes (OLEDs) show promise of revolutionizing display technology due to distinctive attractions over conventional cathode ray tube and liquid crystal displays such as lower materials cost, superior brightness and color purity, markedly lower drive voltages, as well as increased viewing angles.[1-7] Improving OLED electroluminescent characteristics has been the focus of an extensive worldwide research effort with notable success in both device fabrication techniques and materials development.[8-17] OLEDs are "dual-injection" devices in which holes and electrons are injected from the anode and cathode, respectively, under application of an electric field, into an active molecular/macromolecular medium. Some fraction of the electron-hole pairs recombine to form excitons, which in turn radiatively decay to ground states and emit light.[6,18] To achieve optimum device performance, it is desirable to have multilayer structures[5] having discrete-hole transport layer (HTL),[19] emissive layer (EML), and electron-transport layer (ETL)[20] functions (Figure 1). With such multilayer structures, high-performance devices[8,12] have been realized for small-molecule-based OLEDs fabricated via vacuum deposition. Typical small-molecule HTLs are triarylamine-based materials such as NPB or TPD (Scheme 1), which are known to have appreciable hole-transporting and electron-/exciton-blocking capacity because of their relatively high-lying lowest-unoccupied molecular orbital (LUMO) levels and large highest-occupied molecular orbital (HOMO)-LUMO gaps.

To date, increasing evidence indicates that the anode (usually tin-doped indium oxide, ITO)–HTL interface is crucial to hole injection in a common scenario where ITO–HTL contact rather than HTL bulk mobility limits charge injection.[21-25] To tune the electronic properties at an anode surface has been a crucial issue because electronic profiles at the anode/organic interface

strongly affect electron/hole injection fluence and recombination of the charge carriers that are central factors for enhacing OLED efficiency.[9,11,26,27] A variety of interfacial engineering approaches have been applied to the anode–HTL junction, including introduction of π-conjugated polymers,[28] such as polyaniline-camphorsulfonic acid (PANI-CSA)[29,30] and poly(3,4-ethylenedioxythiophene)-poly(styrenesulfonate) (PEDOT-PSS) (Scheme 1),[31-33] copper phthalocyanine,[34,35] organic phosphonic[36,37] and carboxylic acids,[38] a thin-layer of platinum,[39] self-assembled polar molecules to manipulate surface dipoles,[40,41] self-assembled siloxanes,[42-44] and plasma treatment of the ITO surface.[45] All of these approaches have non-negligible effects on hole injection and yield varying degrees of improved device performance in terms of turn-on voltage, luminance, stability, and/or current efficiency. In previous work from this laboratory, we demonstrated that small-molecule OLED performance and durability can be significantly enhanced using triarylamine-based siloxane hole-transporting materials such as TPD-Si_2 (Scheme 1) as an anode hole injection/adhesion interlayer.[8-12, 43,44, 46-51] (TPD-Si_2 combines the hole-transport capacity of TPD , the covalent-bonding capacity of chlorosilyl/silanol groups, and can enhance OLED hole injection and device durability as a hole injection/adhesion interlayer). However, these trichorosilane-based molecules are sensitive to moisture and air. Thus, they are not easily adapted to conventional large-area process conditions, such as roll-to-roll and ink-jet patterning processes.

In this contribution, we report the synthesis, characterization, and implementation of a new interlayer material, TPD-$[Si(OCH_3)_3]_2$, which has relatively air-stable trimethoxysilyl linkers. A robust, smooth, conformal, adherent, and essentially pinhole-free monolayer or multilayer films can be deposited by self-assembly and simple spin-casting this molecule, respectively, via covalent In-O-Si/Sn-O-Si linkages. Both of these approaches afford Alq (tris(8-hydroxyquinolato)aluminum(III), Scheme 1)-based small-molecule OLEDs with superior

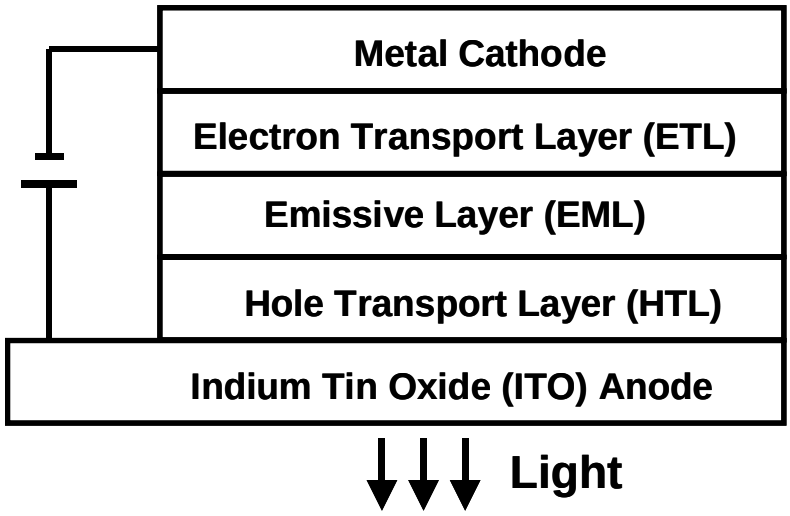

Figure 1. Cross-section of a typical multilayer OLED structure.

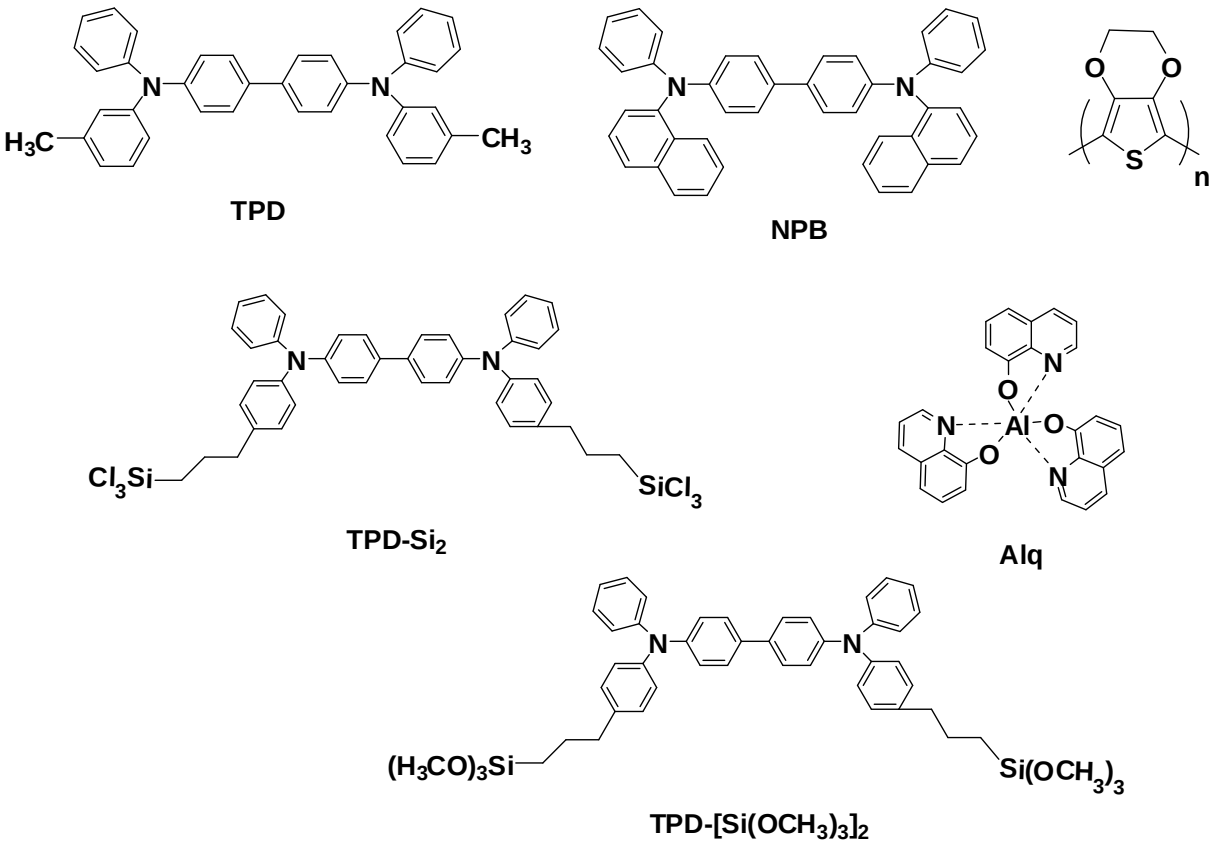

Scheme 1. Structure of Multilayer OLED Constituent Materials: TPD (HTL), NPB (HTL), PEDOT (HTL), Alq (EML/ETL), TPD-Si_2 and TPD-$[Si(OMe)_3]_2$.

performance versus devices relying on simple ITO–NPB interfaces without an interlayer, and performance comparable to that of TPD-Si_2 interlayer-based OLEDs.

2. Experimental

2-1. Materials and Methods. ITO glass sheets (20 Ω/o, rms roughness = 2.5 nm) were purchased from Colorado Concept Coating. All chemical reagents were used as received unless otherwise indicated. All manipulations of air/moisture-sensitive materials were carried out on a dual-manifold Schlenk line or in a nitrogen-filled glovebox. Ether and THF were distilled before use from sodium/benzophenone ketyl. Methylene chloride was distilled before use from calcium hydride. Toluene was dried using activated alumina and Q5 columns and tested with benzyphenone ketyl in ether solution. TPD and Alq were purchased from Sigma-Aldrich and purified via vacuum gradient sublimation. NPB was synthesized according to the literature,[52] and was purified by recrystallization followed by vacuum gradient sublimation. The synthesis of TPD-Si_2 was reported elsewhere.[11] NMR spectra were obtained on Varian VXR-400 or 500 MHz NMR instruments. MS analyses were conducted on a Micromass Quattro II Triple Quadrupole HPLC/MS/MS mass spectrometer. Elemental analyses were carried out by Midwest Microlabs. Cyclic voltammetry was performed with a BAS 100 electrochemical workstation (SAM-coated ITO with ~1cm ^{2} area working electrodes, Ag wire pseudo-reference electrode, Pt wire counter electrode, 0.1 M TBAHFP in anhydrous MeCN supporting electrolyte, and 0.001 M ferrocene as the internal pinhole probe. Scan rate = 0.1 V/s.). TBAHFP was recrystallized from an ethyl acetate/hexanes mixture and dried in vacuo at 100 ^{o}C for 10 h. Ferrocene was purchased from Sigma-Aldrich and purified via vacuum gradient sublimation. AFM images were obtained on a Nanoscope III AFM under ambient conditions in the contact mode with Si_3N_4 cantilevers.

Specular x-ray reflectivity experiments on coated single-crystal Si (111) substrates were performed on the National Research Laboratory X23B beamline at the National Synchrotron Light Source. Data were acquired and analyzed as described previously.[11,44] The thickness of spin-cast films was measured with a Tencor P-10 profilometer. XPS measurements were performed at Northwestern U. with an Omicron ESCA probe, which was equipped with EA125 energy analyzer. Photoemission was stimulated by a monochromatic Al Kα radiation (1486.6 eV) with the operating power of 300 W, and a low-energy electron flood gun was employed for charge neutralization. Binding energies of spectra were referenced to the C 1s binding energy set at 284.8 eV.

2-2. Synthesis of 4,4′-*bis*[(*p*-bromophenyl)phenylamino)]biphenyl (Scheme 2) (1). To a toluene solution (50 mL) of tris(dibenzyldeneacetone)dipalladium (0.55g, 0.60 mmol) and bis(diphenylphosphino)ferrocene, (0.50g, 0.90 mmol), was added 1,4-dibromobenzene (18.9g, 0.0800 mol) at 25 ^{o}C. Following stirring under an N_2 atmosphere for 10 min, sodium *tert*-butoxide (4.8g, 0.050mol) and N,N'-diphenylbenzidine (6.8g, 0.020 mol) were added. The reaction mixture was then stirred at 90°C for 12h, followed by cooling to 25 ^{o}C. The reaction mixture was then poured into water and the organic and aqueous layers separated. The aqueous layer was extracted with toluene (3 ×100 mL) and the resulting extracts were combined with the original organic layer. The solvent was removed *in vacuo* giving a crude product which was purified by chromatography on a silica gel column (6:1 hexane: ethylene chloride eluent) to yield pure **1** as a colorless solid (6.9g) in 50% yield.^{1}H NMR ($CDCl_3$): δ 6.99(d, J = 8.8 Hz, 4H), 7.02-7.16(m, 10H), 7.28(t, J = 7.6Hz, 4H), 7.34(d, J = 8.8Hz, 4H), 7.45(d, J = 8.4Hz, 4H).

2-3. Synthesis of 4,4′-*bis*[(*p*-allylphenyl)phenylamino]biphenyl (2). Using standard Schlenk techniques, 1.6 mL (3.5 mmol) *n*-butyl lithium (2.5 M in hexanes) was added dropwise under inert atmosphere to a stirring ether solution (10 mL) of **1** (1.02g, 1.58mmol) while maintaining the temperature at 25 ^{o}C. The mixture was stirred for 2 h after which time CuI (0.76g, 4.0 mmol) was next added. Upon cooling the reaction mixture to 0 °C, allyl bromide (0.60g, 5.0 mmol) was added in one portion and the mixture stirred for 14 h, followed by quenching with saturated aqueous NH_4Cl solution (100mL), and extraction with ether (3 ×100mL). The combined ether extracts were washed with water (2 ×100mL), brine (2 ×100mL), and dried over anhydrous Na_2SO_4. Filtration and removal of solvent *in vacuo* afforded a yellow oil, which was further purified by chromatography on a silica gel column (4:1 hexane: methylene chloride) to yield 0.63 g of pure **2** as a colorless solid. Yield, 70%. ^{1}H NMR ($CDCl_3$): δ 3.40(d, J = 10Hz, 4H), 5.10- 5.20(m, 4H), 6.02(m, 2H), 6.99-7.10(m, 2H), 7.10-7.20(m, 16H), 7.28(t, J = 7.6Hz, 4H), 7.46(d, J = 8.8Hz, 4H). Anal. Calc'd for $C_{42}H_{36}N_2$: C 88.68, H 6.39, N 5.23 Found, C 87.50, H 6.35, N 4.93.

2-4. Synthesis of 4,4′-*bis*[(*p*-trimethoxysilylpropylphenyl)phenylamino]biphenyl (TPD-[Si(OCH$_3$)$_3$]$_2$, 3). Under inert atmosphere at 25 ^{o}C, few grains of Cp_2PtCl_2, followed by $HSi(OMe)_3$ (2.15 g, 17.6 mmol) was added to a dry toluene solution (50 mL) of **2** (0.32 g, 0.55 mol) and the reaction mixture stirred at 80 ^{o}C and monitored by NMR until the completion of reaction after 60 h. Removal of the solvent in vacuo yielded a dark-yellow oil, which was triturated with a mixture of 50mL anhydrous pentane and 10 mL anhydrous toluene to yield a solid which was removed by filtration. The filtrate was concentrated in vacuo to yield **3** as a pale-yellow oil. Yield: 94%. ^{1}H NMR ($CDCl_3$): 0.71 (t, *J* = 7.6 Hz, 4H), 1.73 (t, *J* = 7 Hz, 4H), 2.60

(br s, 4H), 3.57 (s, 9H), 6.80-7.80 (m, 26H). ^{13}C NMR ($CDCl_3$) δ 9.4, 16.9, 38.9, 50.2, 123.2, 125.7, 126.8, 128.1, 128.8, 129.0, 129.6, 136.4, 138.2, 143.2, 144.8, 145.9. HRMS Calcd for $C_{48}H_{56}N_2O_6Si_2$: 812.37. Found: 812.40.

2-5. Self-assembly of TPD-[Si(OCH$_3$)$_3$]$_2$ on ITO Substrates. ITO substrates were cleaned in an ultrasonic detergent bath, followed by methanol, isopropanol, and finally acetone. The substrates were subsequently treated in an oxygen plasma cleaner for 1 min to remove any residual organic contaminants. Following strict Schlenk protocol, clean ITO substrates were immersed in a 1.0 mM dry toluene solution of TPD-[Si(OCH$_3$)$_3$]$_2$, respectively. After heating at ~90 ^{o}C for 4 h, the toluene solution was removed by cannula and the substrates were rinsed with dry toluene (2 x 50 mL) and wet acetone in the ultrasonic bath for 3 min each., followed by transferring to a 120 ^{o}C vacuum oven for 2 h to expedite crosslinking. Longer thermal curing yields films with similar properties, and the coating procedure has negligible effects on the measured sheet resistance of the underlying ITO.

2-6. Self-assembly of TPD-[Si(OCH$_3$)$_3$]$_2$ on silicon substrates. Silicon (111) substrates (Semiconductor Processing Co.) were subjected to a cleaning procedure as follows. First, the substrates were immersed in "piranha" solution (4:1 H_2SO_4/H_2O_2) at 80°C for 1 h. After cooling to room temperature, the substrates were rinsed repeatedly with de-ionized (DI) water followed by an RCA-type cleaning protocol (H_2O: 30% H_2O_2: NH_3; 5:1:1 v/v/v; sonicated at room temperature for 40 min). The substrates were finally rinsed with copious amounts of DI water, heated to 125°C for 15 min, and dried *in vacuo*. TPD-[Si(OCH$_3$)$_3$]$_2$ was then self-assembled onto the clean silicon substrates following the procedure described above for ITO substrates

2-7. Spin-casting of TPD-[Si(OCH$_3$)$_3$]$_2$ on ITO Substrates. A toluene solution of TPD-[Si(OCH$_3$)$_3$]$_2$ (4 mg/mL) was spin-coated onto clean ITO substrates at 1500 rpm in air, followed

by curing in a vacuum oven at 110 ^{o}C for 2h.[10] To improve the cross-linking reaction of TPD-$[Si(OMe)_3]_2$, another facile method was used. A 95% ethanol-5% water solution was adjusted to pH = 4.5-5.5 with acetic acid. TPD-$[Si(OCH_3)_3]_2$ was added with stirring to yield a 2% final concentration. The aqueous alcohol solution of TPD-$[Si(OCH_3)_3]_2$ was then spin-coated onto the clean ITO surfaces at 1000 rpm in air, followed by curing in a vacuum oven at 110 ^{o}C for 2h.[10,56] Note here that the TPD-$[Si(OCH_3)_3]_2$ solution was distributed evenly on the ITO plate from a syringe with a 0.2 μm HPLC filter and exposed in the air for 5 min before spinning, to optimize hydrolysis and silanol formation. The appropriate concentration of building block solution and the spinning speed was obtained after a few experiments.

2-8. Fabrication of OLED Devices. The bare and modified ITO substrates were loaded into a bell jar deposition chamber housed in a nitrogen-filled glove box. A typical deposition procedure is as follows: At 1×10^{-6} Torr, a 20 nm layer of NPB was first deposited, followed by 60 nm of Alq. Both organic layers were grown at a deposition rate of 2 -3 Å/sec. Finally, 1nm LiF and a 100 nm thick Al cathode were deposited through a shadow mask. This metallic layer was patterned to give four devices, each with an area of 0.10 cm^2. OLED device characterization was carried out with a computer-controlled Keithley 2400 source meter and IL 1700 Research Radiometer equipped with a calibrated silicon photodetector at 25 °C under ambient atmosphere. Current efficiency was estimated from current density vs. voltage and luminance vs. current density response characteristics.

2-9. Fabrication of Hole-Only Devices. Bare and modified ITO substrates were loaded into a bell jar deposition chamber housed within a nitrogen-filled glove box. At a base pressure of $1x10^{-6}$ Torr, NPB (400 nm) was vapor deposited at a rate of ~3Å/sec, followed by sputter-coating of a 6 nm of Au layer through the same shadow mask employed for the OLED fabrication

described above. Single-carrier device assembly was subsequently completed with the masked thermal vapor deposition of Al (150 nm). Device behavior was evaluated using the computer-controlled Keithley 2400 sourcemeter.

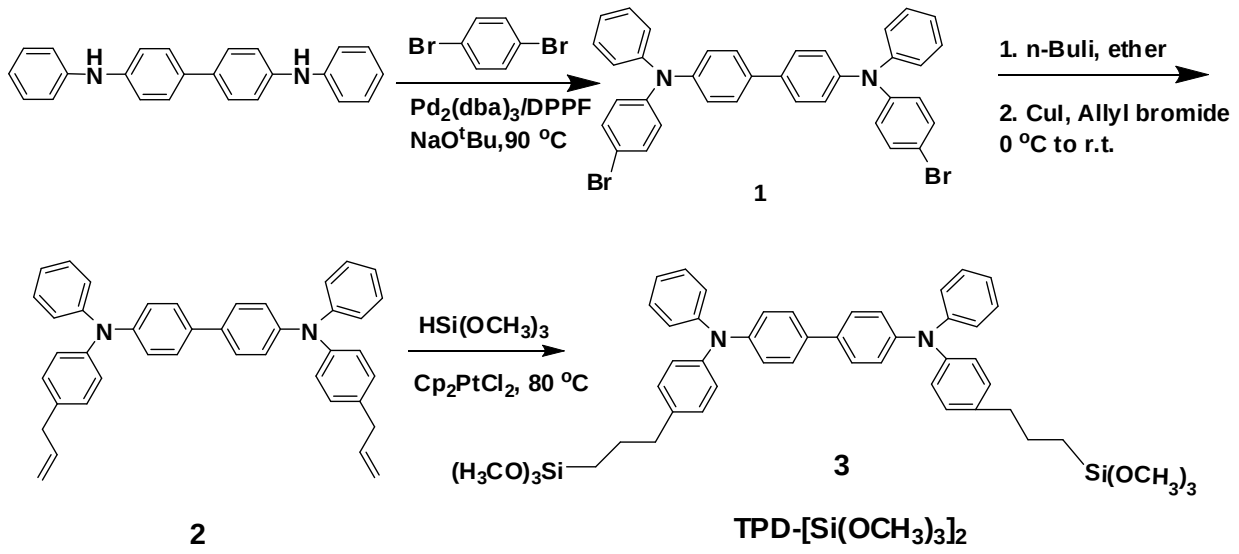

Scheme 2. Synthetic Route to TPD-[Si$(OCH_3)_3]_2$.

3. Results and Discussion

In Section 3.1, we discuss the deposition and characterization of self-assembled monolayers (SAMs) or spin-coated films of TPD-$[Si(OMe)_3]_2$ on glass/ITO substrates. In Section 3.2, SAMs or spin-coated films of TPD-$[Si(OMe)_3]_2$ are used as ITO anode – NPB interlayers, and the effect on OLED EL response compared to SAMs or spin-coated films of TPD-Si_2, having $–SiCl_3$ linkers, and which is much more reactive than $–Si(OMe)_3$, is analyzed here. It will be seen that Alq -based small-molecule OLEDs with SAMs or spin-coated films of TPD-$[Si(OMe)_3]_2$ interlayers exhibit superior performance versus devices relying on simple ITO–NPB interfaces without an interlayer, and performance comparable to that of TPD-Si_2 interlayer-based OLEDs.

3-1. Deposition and Characterization of TPD-$[Si(OMe)_3]_2$ on ITO substrate

3-1.1. Anhydrous and Hydrolytic Depositions of TPD-$[Si(OMe)_3]_2$ on ITO substrate.

The synthetic pathway to TPD-$[Si(OMe)_3]_2$ is summarized in Scheme 2, while detailed procedures and characterization data are presented in the Experimental Section. Utilizing a self-limiting, anhydrous solution-based chemisorption process, TPD-$[Si(OMe)_3]_2$ is self-assembled onto hydrophilic glass/ITO substrate surfaces with nanoprecise control in thickness. As illustrated in Scheme 3, clean ITO-coated glass surface possesses hydroxyl functionalities which are reactive towards methoxysilanes, thereby affording covalent binding of the silanes to the surface.[53-55] The process of anhydrous deposition is described in Scheme 3A,[56] through which a monolayer of siloxane (~ 1.75 nm) forms. For organo-SiX_3 precursors, approximately 3 bonds are formed from each silicon to hydroxylated surfaces.[53-55] Further exposure to air and moisture in the following wet acetone rinse hydrolyzes any unreacted methoxysilyl groups. Subsequent thermal curing facilitates formation of crosslinked siloxane networks, resulting in a thin layer consisting of hole transporting moieties covalently anchored to the ITO surface.

Spin-casting TPD-$[Si(OMe)_3]_2$ from toluene solution or acidic aqueous alcohol solutions blended with acetic acid affords thicker films (~ 40 nm, measured by profilometer) on glass/ITO substrates (Scheme 3B),[56] which is different from the anhydrous deposition described above, given that the spin-coating parameters such as solution concentration and spinning speed are carefully controlled (see Experimental for details). During the hydrolytic deposition, the TPD-$[Si(OMe)_3]_2$ methoxy groups are hydrolyzed to form silanol-containing species. This reaction mode of TPD-$(Si(OMe)_3)_2$ likely involves four steps: (1) hydrolysis, (2) condensation, (3) hydrogen bonding, and (4) surface bond formation.[56] Initially, hydrolysis of the Si-OCH_3 groups occurs. Water for hydrolysis may come from several sources. It may be added, it may be present on the substrate surface, or it may come from the atmosphere. Condensation to oligomers follows. The oligomers then hydrogen bond with OH groups of the substrate. Finally, during drying or curing, a covalent linkage is formed to the substrate with concomitant loss of water. Although described sequentially, these reactions can occur simultaneously after the initial hydrolysis step. The microstructural characterization of these layers is presented below.

3-1.2 Characterization of TPD-$[Si(OMe)_3]_2$-derived Films by Advancing Aqueous Contact Angles and X-ray Photoelectron Spectroscopy (XPS).

Aqueous advancing contact angles were measured before and after self-assembly/spin-casting. Because the hydroxyl groups of the oxide layer create a hydrophilic surface, bare ITO exhibits a very low contact angle value ($\theta \leq 15°$), however, after TPD-$[Si(OMe)_3]_2$ self-assembly or spin-casting, relatively high values ($\theta = 77°$ for SAM-modified ITO and $\theta = 85°$ for spin-coated film-modified ITO) are observed, indicating that the ITO surfaces become hydrophobic. In addition to these contact angle measurements, an XPS study was also performed to investigate the surface atomic composition. Figure 2 shows the XPS spectra of the TPD-$[Si(OMe)_3]_2$-derived

SAM (Fig. 2a) and spin-coated film (Fig. 2b) on ITO. Two new features characteristic of Si (2p) at 101.0 eV and N (1s) at 400 eV are attributable to TPD-$[Si(OMe)_3]_2$ hydrolysis products. Note here that In and Sn peaks can no longer be detected on the spin-coated TPD-$[Si(OMe)_3]_2$ films, since the thickness of the spin-casting film is significantly beyond 10 nm. Note that standard XPS techniques measure the kinetic energies and numbers of electrons escaping from the upper 1-10 nm of the material being analyzed.[57]

3-1.3 Characterization of TPD-$[Si(OMe)_3]_2$-Derived Films by Specular X-ray Reflectivity and Profilometry.

X-ray reflectivity (XRR) measurements on TPD-$[Si(OMe)_3]_2$ SAMs deposited on single-crystal Si (111) substrates yield a thickness of 1.75 nm (close to the value of ~1.45 nm estimated by an approximate AM1-level calculation), suggesting that most TPD-$[Si(OMe)_3]_2$ molecules are chemisorbed on the substrate in an approximately "upright" orientation. The thicknesses of TPD-$[Si(OMe)_3]_2$ films spin-cast from toluene solution or from the aqueous alcohol + acetic acid blend solution are ~37 nm and ~ 43 nm, respectively, determined by profilometry measurements. Similarly, the thickness of a spin-cast TPD-Si_2 film is around 35 nm.

3-1.4 Characterization of TPD-$[Si(OMe)_3]_2$-Derived Films by Atomic Force Microscopy.

Tapping mode AFM imaging was carried out on three spots randomly chosen on each TPD-$[Si(OMe)_3]_2$-derived film on ITO substrates, self-assembled or spin-cast from toluene solution or the aqueous alcohol + acetic acid blend solution, respectively. Uniform films with no evidence of cracks or pinholes are observed over a 5 × 5 μm scan area (Figure 3). The rms

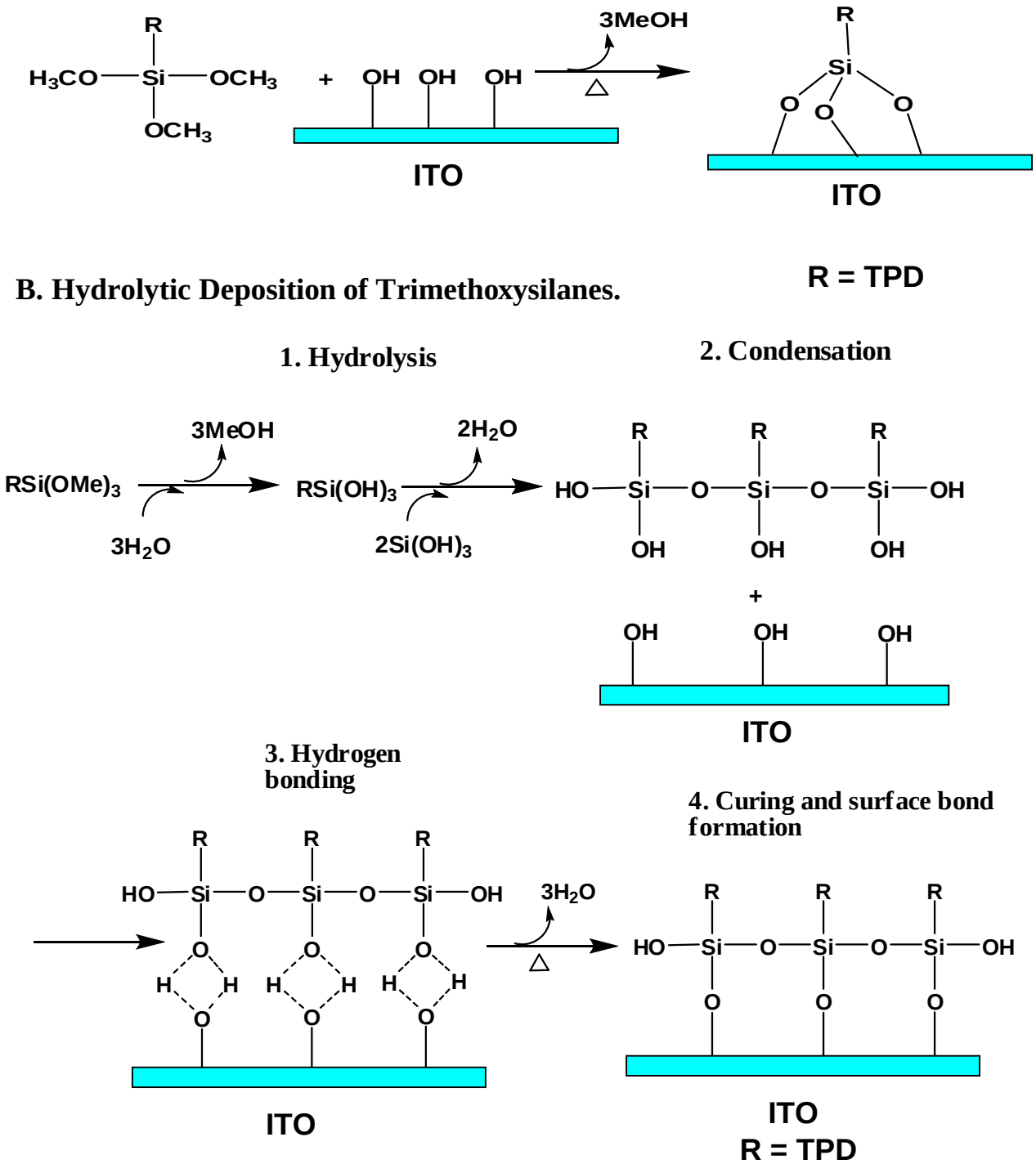

Scheme 3. Mechanisms of ITO Surface Modification by Trimethoxysilane Reagents to Form Thin Film HTL Materials: A. Anhydrous Deposition, B. Hydrolytic Deposition.

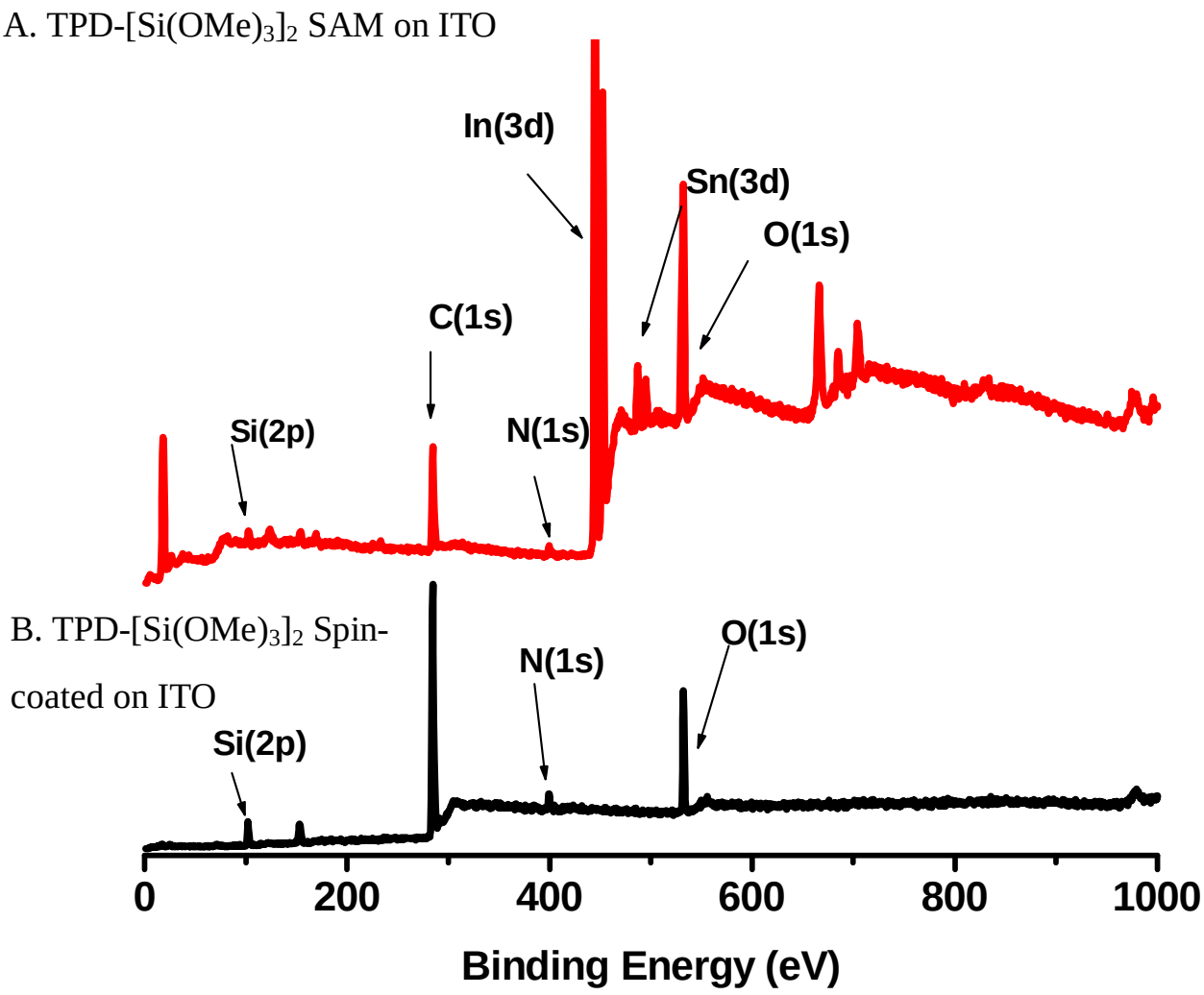

Figure 2. XPS spectra of a TPD-[Si(OMe)$_3$]$_2$-derived SAM and spin-coated film on glass/ITO substrates.

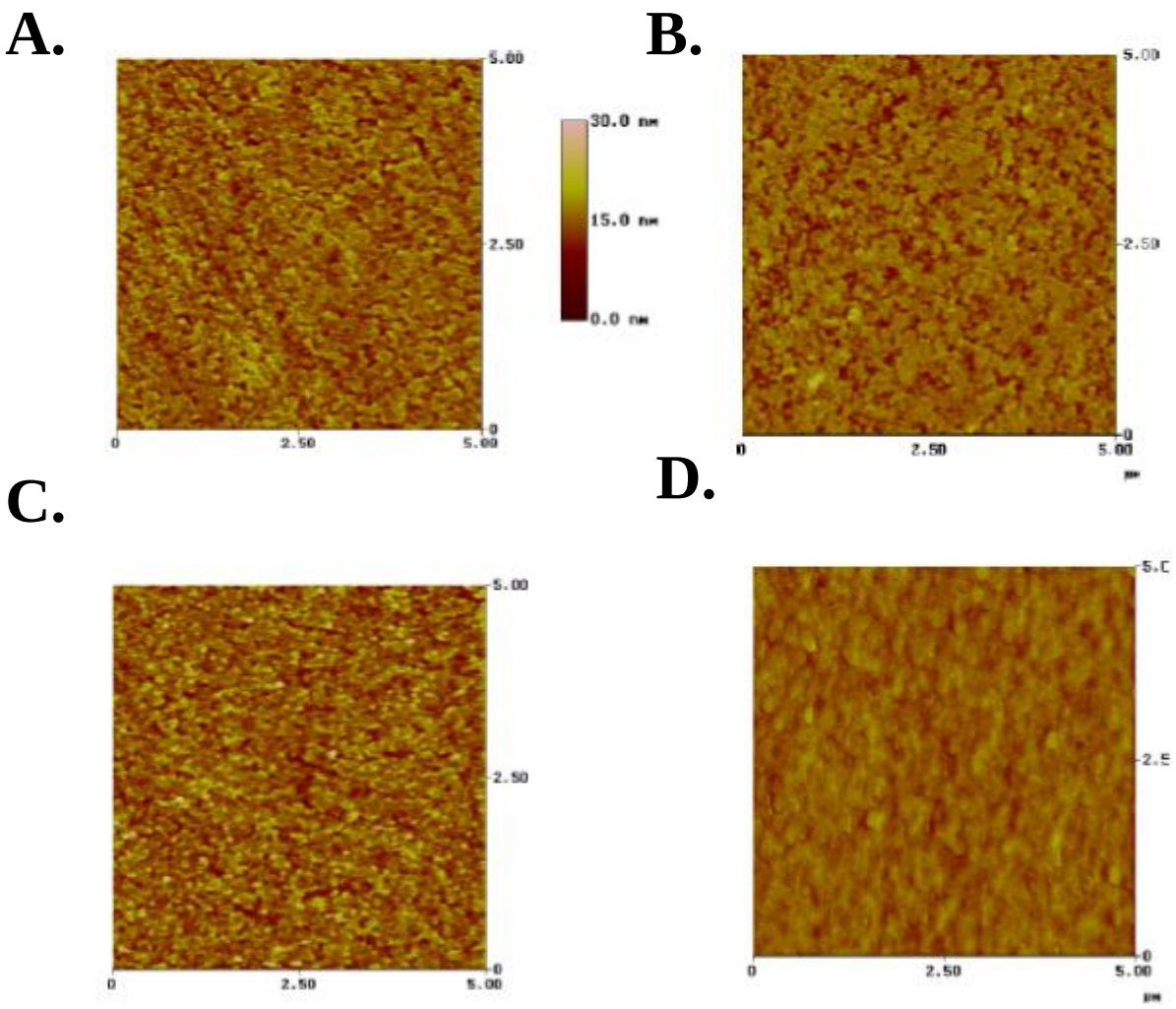

Figure 3. Tapping mode AFM images of self-assembled or spin-cast TPD-$[Si(OMe)_3]_2$-derived films, deposited from toluene solution or aqueous alcohol + acetic acid blend solution on ITO substrates. A. Bare ITO. RMS roughness = 2.5 nm. B. TPD-$[Si(OMe)_3]_2$ SAM on ITO. RMS roughness = 2.0 nm. C. TPD-$[Si(OMe)_3]_2$ spin-coated film from toluene solution on ITO. RMS roughness = 2.8 nm. D. TPD-$[Si(OMe)_3]_2$ spin-coated film from aqueous alcohol + acetic acid blend solution on ITO. RMS roughness = 1.5 nm.

roughness is 2.0 nm for the TPD-$[Si(OMe)_3]_2$ SAM, and 2.8 and 1.5 nm, respectively, for spin-coated TPD-$[Si(OMe)_3]_2$ films from toluene solution and from the aqueous alcohol + acetic acid blend solution, as compared to bare ITO substrates which have an rms roughness of 2.5 nm.

3-1.5 Characterization of TPD-$[Si(OMe)_3]_2$-derived Films by Cyclic Voltammetry .

Redox Property Assessment by Cyclic Voltammetry. Glass/ITO substrates covered with TPD-$[Si(OMe)_3]_2$-derived SAMs or spin-coated films, a silver wire, and a Pt wire were used as the working electrode, reference electrode, and counter electrode, respectively, in a 0.1 M acetonitrile solution of tetrabutylammonium hexafluorophosphate as the electrolyte without ferrocene. The cyclic voltammetry plots obtained at a scan rate of 0.1 V/s are shown in Figure 4A. The cyclic voltammetry of self-assembled or spin-coated TPD-$[Si(OMe)_3]_2$ films on ITO electrodes indicates that they are electroactive, capable of efficient hole transport, and electrochemically stable. The densely crosslinked nature of TPD-$[Si(OMe)_3]_2$ films is evident in the relatively large separation of oxidative and reductive peaks (250 mV), suggesting kinetically hindered oxidation/reduction processes with retarded counterion mobility.[58] Also, the full widths at half-height of oxidative and reductive waves at the sweep rate of 0.1 mV/s are 423 mV and 235 mV, respectively, which suggest the heterogeneity in the N environments.[63]

Integration of the oxidative peak area and assuming two electron oxidation/reduction events per molecular unit yields a monolayer surface coverage of 3.5×10^{-10} mol/cm^2 for the TPD-$[Si(OMe)_3]_2$ SAM.[58] Analogously, a close-packed monolayer of ferrocene dicarboxylic acid adsorbed on ITO yields a 4.0×10^{-10} mol/cm^2 surface coverage.[59] In addition, the apparent surface coverages of spin-coated TPD-$[Si(OMe)_3]_2$ films from toluene solution and aqueous alcohol + acetic acid blend solution are 6.1×10^{-9} mol/cm^2 and 7.5×10^{-9} mol/cm^2, respectively,

which indicate the formation of thicknesss beyond monolayer dimensions in these spin-coated films. The higher apparent surface coverage of the spin-coated TPD-$[Si(OMe)_3]_2$ films from aqueous alcohol + acetic acid blend solution than from toluene solution suggests a qualitatively different crosslinking pattern within the latter films, allowing a greater extent of oxidation.

Pinhole Assessment by Ferrocene Cyclic Voltammetry. To examine the present TPD-$[Si(OMe)_3]_2$-derived films for pinholes over the entire ITO substrate area (1 cm^2), cyclic voltammetry experiments using ferrocene as an internal redox probe were carried out.[60] Here the self-assembled and spin-coated siloxane film-coated ITO substrates were used as working electrodes with bare ITO substrates used as references to calibrate the ferrocene redox potential for each measurement. The results are shown in Figure 4B. The ferrocene oxidation peak potential is ~1.0 V with the bare ITO substrate as the working electrode, and is shifted to 1.8 V (TPD-$[Si(OMe)_3]_2$ SAM), 2.4 V (spin-coated TPD-$[Si(OMe)_3]_2$ film from toluene solution), and 2.75 V (spin-coated TPD-$[Si(OMe)_3]_2$ film from aqueous alcohol + acetic acid blend solution), respectively, with the self-assembled and spin-coated film-coated ITO substrates as working electrodes. The lack of significant current flow near the formal oxidation potential of ferrocene indicates an inhibition of ferrocene oxidation, resulting from conformal and largely pinhole-free film coverage of the ITO. As the triarylamine oxidation potentials are reached, an electrocatalytic current response is observed, indicating that ferrocene is oxidized at an essentially diffusion-controlled rate, meaning that facile triarylamine group oxidation at the ITO/HTL interface (hole injection), and rapid hole migration (presumably accompanied by counteranion migration) through the nanoscopic film occurs such that ferrocene oxidation takes place at the film-solution interface.[61,62]

The reduction of the ferricenium cation on the return sweep is partially blocked by the TPD-$[Si(OMe)_3]_2$ SAM, and more completely blocked by the spin-coated TPD-$[Si(OMe)_3]_2$ films, suggesting that the latter films are somewhat more pinhole-free.[63] The larger separations of ferrocene oxidative and reductive peak potentials at the self-assembled and spin-coated siloxane film-coated ITO electrodes *vs.* on the bare ITO ones (2.8 V, spin-coated TPD-$[Si(OMe)_3]_2$ film from aqueous alcohol + acetic acid blend solution; 2.1 V, spin-coated TPD-$[Si(OMe)_3]_2$ film from toluene solution; 1.30 V, TPD-$[Si(OMe)_3]_2$ SAM; 0.4V, bare ITO) may also indicate that in the redox processes, counterion penetration and diffusion in the siloxane films is retarded, presumably due to the densely packed, crosslinked networks.[64-67] It is likely that the spin-coated TPD-$[Si(OMe)_3]_2$ films from aqueous alcohol + acetic acid blend solution, due to the water and acetic acid in the solvent, which accelerate hydrolysis of the methoxysilane groups,[56] are more heavily cross-linked compared to the spin-coated TPD-$[Si(OMe)_3]_2$ films from toluene solution, resulting in somewhat more densely packed films.

3-2. Self-Assembled and Spin-Cast TPD-$[Si(OMe)_3]_2$ Films in OLEDs

3-2.1 Applying TPD-$[Si(OMe)_3]_2$ SAM as ITO anode – NPB Interlayer.

Self-assembled TPD-$[Si(OMe)_3]_2$-derived and TPD-Si_2-derived monolayers were applied as interlayers between the ITO anode and a conventional vapor-deposited NPB HTL in OLEDs having structures: ITO/HTL SAM/NPB (20 nm)/Alq(60 nm)/LiF (1 nm)/Al (100 nm). Insertion of these interlayers between the anode and the NPB HTL dramatically enhances OLED EL

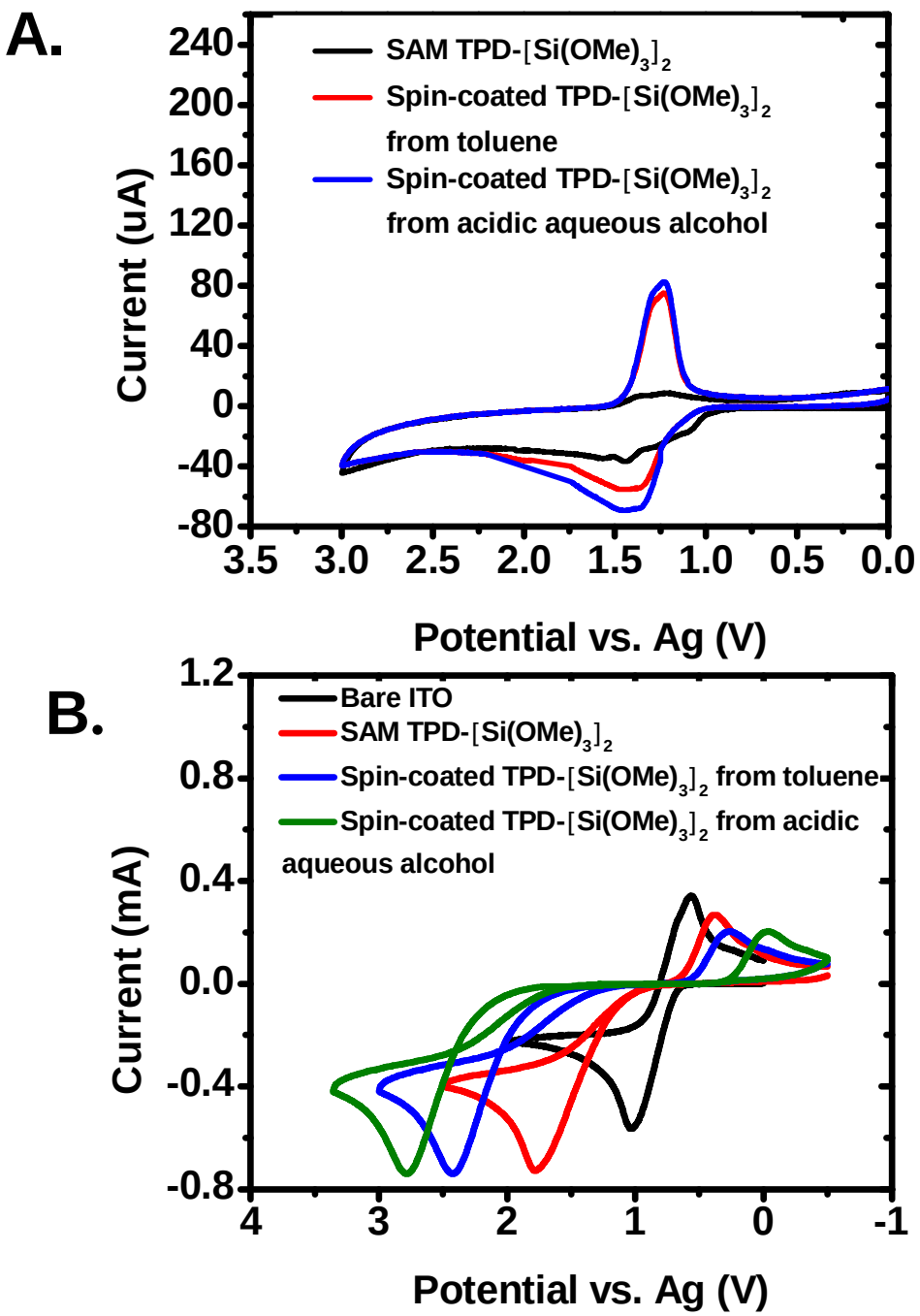

Figure 4. A. Cyclic voltammetry of TPD-$[Si(OMe)_3]_2$-derived SAM and spin-coated films on galss ITO with 0.1 M TBAHFP electrolye at a 0.1 V/s scan rate. B. Cyclic voltammetry of SAM and spin-coated TPD-$[Si(OMe)_3]_2$ films on ITO with 1mM ferrocene as an internal probe in 0.1 M TBAHFP electrolye at a 0.1 V/s scan rate.

response compared to devices without the interlayers (Figure 5 and Table 1). As compared to OLEDs using an NPB-only HTL, which is in direct contact with the ITO anodes, the maximum light output is enhanced by an order of magnitude both for TPD-$[Si(OMe)_3]_2$ -based and TPD-Si_2-based devices: ~1,900 cd/m^2 (NPB only) à 26,500 cd/m^2 (TPD-$[Si(OMe)_3]_2$/NPB) and 25,900 cd/m^2 (TPD-Si_2/NPB), respectively. Likewise, the maximum current efficiency is increased by a factor of ~4 × for both devices: 4.41 cd/A (TPD-$[Si(OMe)_3]_2$/NPB) and 4.10 cd/A (TPD-Si_2/NPB) vs. 1.17 cd/A (NPB alone). Also, TPD-$[Si(OMe)_3]_2$ and TPD-Si_2 SAM-based OLEDs have lower turn-on and operating voltages. For instance, the operating voltage at 300 cd/m^2, a standard brightness for displays, is 6.1 V, 6.3 V, and 8.0 V for TPD-$[Si(OMe)_3]_2$/NPB, TPD-Si_2/NPB, and NPB-only, respectively. These results indicate a substantial increase in hole-injection via ITO anode – NPB HTL interfacial modification.

In the anhydrous toluene deposition of TPD-$[Si(OMe)_3]_2$-derived SAMs, a siloxane monolayer forms on the ITO surface via covalent bonds, a presumably very similar SAM-forming process to that undergone by the trichrolosilane analogue, TPD-Si_2. Indeed, the TPD-$[Si(OMe)_3]_2$ SAM-based devices exhibit almost identical EL response to the TPD-Si_2 SAM -based devices, which can be seen in Figure 5. The substantial OLED EL response enhancement obtained by inserting the siloxane nanostructures between the ITO anode and the NPB HTL, compared to ITO/NPB, can be explained based on the current understanding of ITO anode-HTL interfacial function.[8-12] We propose that the TPD-$[Si(OMe)_3]_2$- and TPD-Si_2-derived materials as ITO anode-NPB interlayers increase hole injection principally by: (1) reducing the hole injection barrier from the ITO anode to NPB (HOMO ~ 5.5 eV) by providing an

Table 1. OLED EL response data for devices having the structure: ITO anode/interlayer/NPB/Alq/LiF /Al. The interlayer is TPD-$[Si(OMe)_3]_2$ SAM, a $TPDSi_2$ SAM, a spin-cast TPD-$[Si(OMe)_3]_2$ from toluene solution, a spin-cast TPD-$[Si(OMe)_3]_2$ from aqueous alcohol + acetic acid blend solution or a spin-cast $TPDSi_2$ film.

HTL	TPD-SiOMe SAM	TPD-Si_2 SAM	TPD-SiOMe (spin-coated -1)	TPD-SiOMe (spin coated -2)	TPD-Si_2 (spin-coated)	NPB-only
Maximum luminance (cd/m^2)	~ 26,500	~ 25,900	~28,900	~ 32,800	~29,800	~1,900
Maximum current efficiency (cd/A)	4.41	4.10	5.71	5.8	5.55	1.17
Turn-on voltage (V)	4.0	4.0	7.25	4.25	3.7	5.1
Operating voltage at 300 cd/m^2 (V)	6.1	6.3	10.4	7.0	6.8	8.0

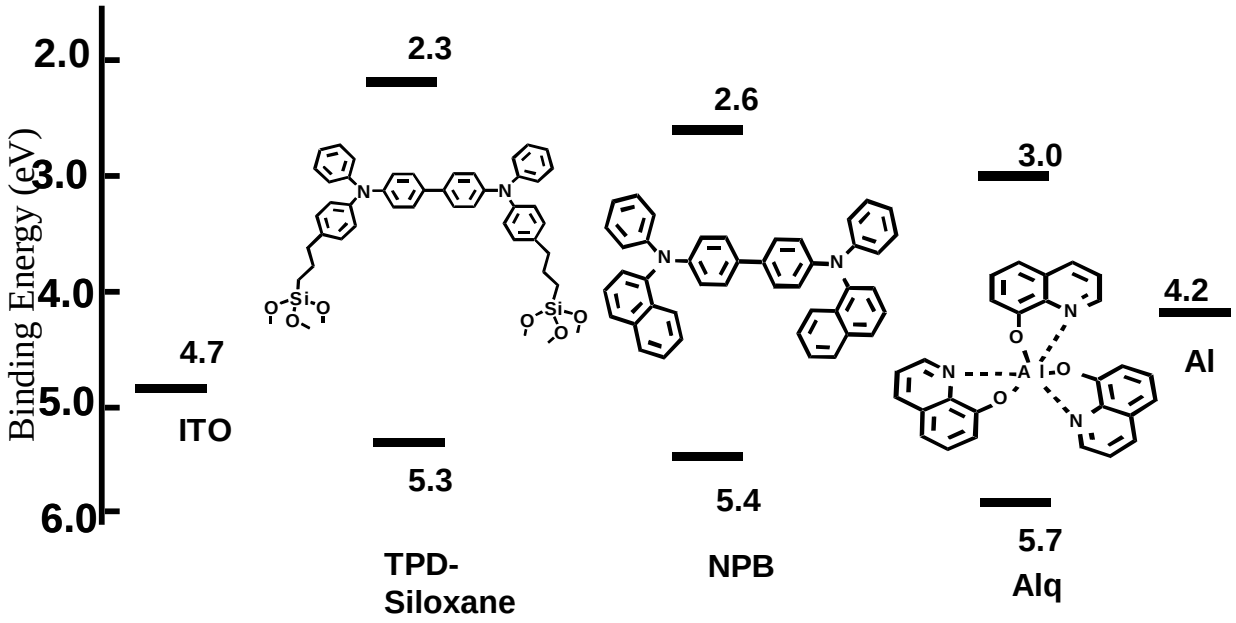

Scheme 4: Energy diagram for the electrodes and OLED organic layers utilized in this study (data taken from the literature)

Figure 5. Responses of OLEDs having the structures: ITO/HTL SAM/NPB (20 nm)/Alq (60 nm)/LiF (1 nm)/Al (100 nm), HTL SAM = TPD-$[Si(OMe)_3]_2$ SAM and TPD-Si_2 SAM. A. current density vs. voltage; B. luminance vs. voltage; C. external forward quantum efficiency vs. voltage.

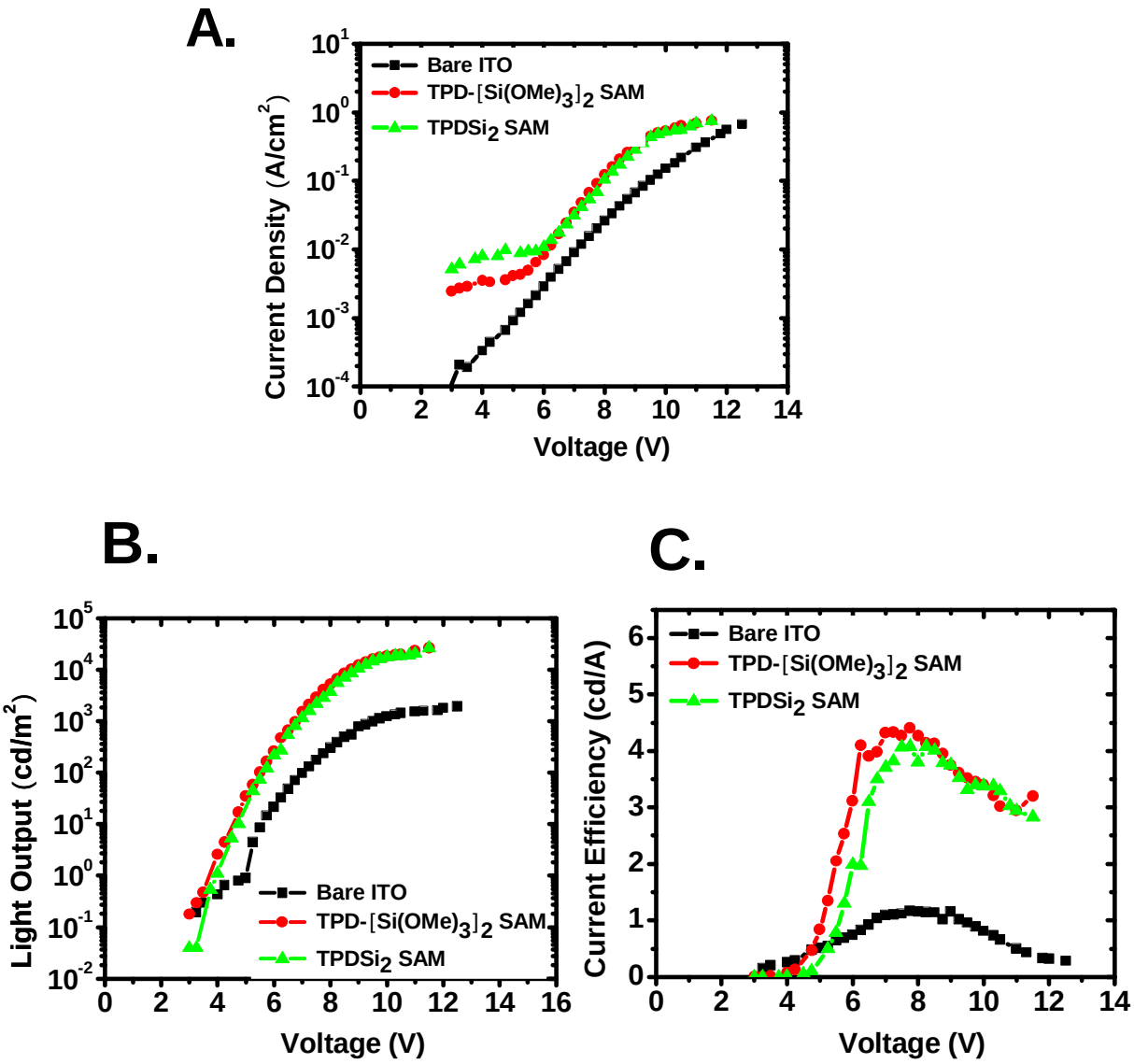

energy-mediating "step", as shown in Scheme 4; (2) enhancing ITO anode-NPB interfacial cohesion via eliminating the surface energy mismatch,[44] and creating more intimate ITO anode – HTL physical and electrical contact;[68] (3) contributing to electron blocking/confinement effects[69] in conjunction with NPB.

3-2.2 Applying Spin-coated TPD-$[Si(OMe)_3]_2$ Films as ITO Anode – NPB Interlayers.

Spin-casting TPD-$[Si(OMe)_3]_2$ layers onto ITO anodes, followed by vapor-deposition of NPB, was also investigated as an alternative approach to applying this arylaminomethoxysilane as the anode-NPB interlayer. To assess the properties of the different TPD-$[Si(OMe)_3]_2$ interlayers spin-coated from different solutions and to allow the comparison with spin-coated TPD-Si_2 interlayers in EL devices, we fabricated OLEDs having three different configurations, where SC = spin-coated: ITO/SC-TPD-$[Si(OMe)_3]_2$ cast from toluene solution//NPB/Alq/LiF/Al (Device 1), ITO/SC-TPD-$[Si(OMe)_3]_2$ cast from aqueous alcohol + acetic acid blend solution /NPB/Alq/LiF/Al (Device 2), and ITO/SC-TPD-Si_2 cast from toluene solution/NPB/Alq/LiF/Al (Device 3). The EL response metrics of current density, luminance, and current efficiency versus operating voltage for these devices are compared in Figure 6 and Table 1. Again, enahnced EL response is observed versus that of OLEDs without interlayers and versus devices fabricated with SAMs as ITO anode-HTL interlayers: maximum light output, ~ 28,900 cd/m^2 (Device 1), ~ 32,800 cd/m^2 (Device 2), ~29,800 cd/m^2 (Device 3) vs. ~ 26,500 cd/m^2 (TPD-$(Si(OMe)_3)_2$ SAM), ~ 25,900 cd/m^2 (TPD-Si_2 SAM), ~ 1,900 cd/m^2 (NPB-only); maximum current efficiencies, 5.71 cd/A (Device 1), 5.8 cd/A (Device 2), 5.5 cd/A (Device 3) vs. 4.41 cd/A (TPD-$(Si(OMe)_3)_2$ SAM), 4.1 cd/A (TPD-Si_2 SAM), 1.17 cd/A (NPB-only). The improved EL response of spin-coated siloxane film-based OLEDs versus that of OLEDs without interlayers can be explained in

the same way as described above for the OLEDs with SAM interlayers. The devices with spin-coated interlayers exhibit greater maximum light output and maximum current efficiency than OLEDs with SAM interlayers, suggesting the more effective electron-blocking properties for the ~ 35-45 nm thick spin-coated interlayers versus that of self-assembled monolayers with only ~ 1-2 nm thickness.[49-51]

The relatively high turn-on voltages in devices having the TPD-$[Si(OMe)_3]_2$ interlayers spin-coated from toluene solution can be seen in Figure 6, and may reflect ITO anode – siloxane film contact differences and incomplete intermolecular crosslinking in the siloxane network because of the less reactive trimethoxysilyl functional groups. This increased turn-on voltage effect is resolved in device 2, in which the TPD-$[Si(OMe)_3]_2$ interlayer was spin-coated from a aqueous alcohol + acetic acid blend solution. The turn-on voltage is 4.25 V for device 2, which is about 3V less than that for device 1, 7.25 V. The result argues that denser crosslinking of the methoxysilane with the ITO surface and intermolecular crosslinking within the TPD-$[Si(OMe)_3]_2$ siloxane network is expedited by the water and acetic acid from the solvent, consistent with the film redox properties and pinhole assays by cyclic voltammetry as described above. The enhancement of maximum luminance and current efficiency in Device 2 indicates increased hole-injection efficiency via increased ITO anode –HTL physical/electrical/chemical contact. This effect was investigated further by fabricating hole-only devices with structures of ITO/SC-TPD-$(Si(OMe)_3)_2$ siloxanes/NPB (400 nm)/ Au (6 nm)/ Al (120 nm) (Figure 7). Because of the high work function of gold (5.2 eV), electron injection from the Al cathode into NPB is largely blocked, so that hole currents dominate the charge transport in the above devices. Because the only difference in the two types of hole-only devices is in the spin-coated TPD-$[Si(OMe)_3]_2$

Figure 6. Responses of OLEDs having the structures: ITO/ spin-coated-TPD-$[Si(OMe)_3]_2$ from toluene solution/NPB (20 nm)/Alq(60 nm)/LiF (1 nm)/Al (100 nm) (Device 1), ITO/ spin-coated-TPD-$[Si(OMe)_3]_2$ from aqueous alcohol + acetic acid blend solution/ NPB (20 nm)/Alq(60 nm)/LiF (1 nm)/Al (100 nm) (Device 2), and ITO/ spin-coated-TPD-Si_2 from toluene solution/ NPB (20 nm)/Alq(60 nm)/LiF (1 nm)/Al (100 nm) (Device 3). A. current density vs. voltage; B. luminance vs. voltage; C. external forward quantum efficiency vs. voltage.

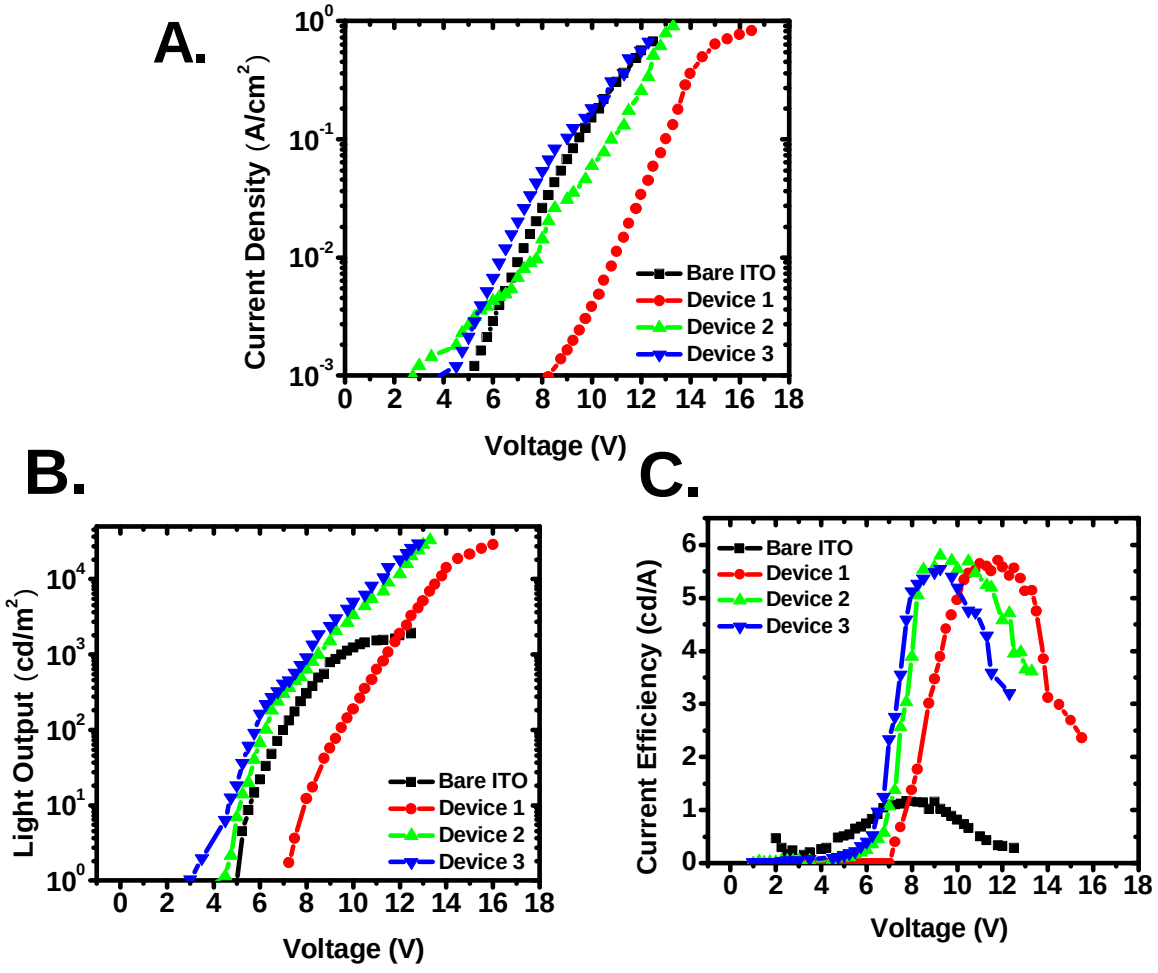

Figure 7. Evaluation of hole injection properties of anode spin-coated functionalization layers, comparing the I-V response for hole-only devices having the structure ITO/spin-coated siloxane/NPB (400 nm)/Au (6 nm)/Al (120 nm). Spin-coated siloxane = SC-TPD-$[Si(OMe)_3]_2$ from toluene solution (hole-only device-1) and SC-TPD-$[Si(OMe)_3]_2$ from aqueous alcohol + acetic acid blend solution (hole-only device-2).

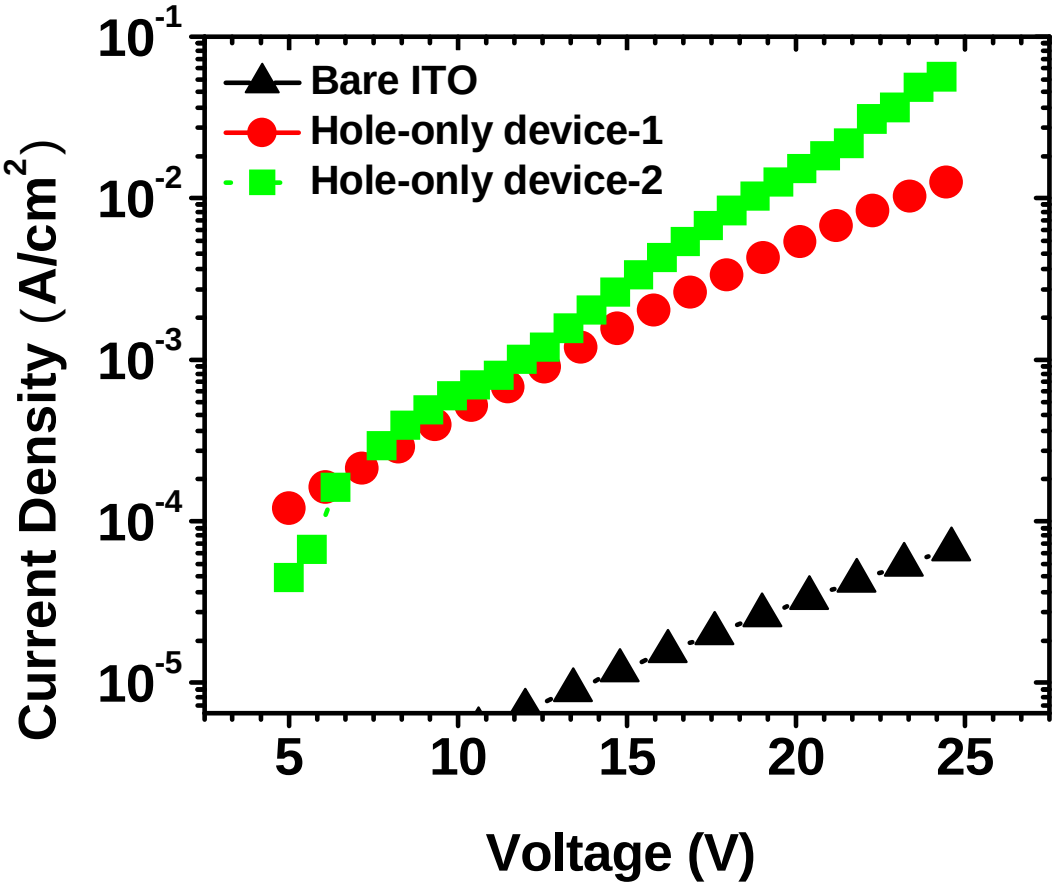

films, the results clearly reveal the significant hole injection enhancement by modifying the anode with the spin-coated TPD-$[Si(OMe)_3]_2$ films from the aqueous alcohol + acetic acid blend solution. For example, hole current densities at 20 V are ~0.00004 A/cm^2 (bare ITO) < ~0.0054 A/cm^2 (hole-only Device-1) < ~0.015 A/cm^2 (hole-only Device-2). The slightly higher turn-on voltage of Device 2, 4.25 V, versus that of OLEDs with spin-coated TPD-Si_2-derived interlayers, 3.75 V, is likely due to the greater thickness of spin-coated TPD-$[Si(OMe)_3]_2$ films (~ 43 nm) from the aqueous alcohol + acetic acid blend solutions compared to TPD-Si_2 films spin-coated from toluene solution with ~ 35 nm thickness.[10]

4. Conclusions

An arylaminotrimethoxysilane functionalized hole-transporting triphenylamine (TPD-$[Si(OMe)_3]_2$) was synthesized and can be self-assembled or spin-coated onto ITO surfaces, enhancing ITO–HTL contact via robust covalent bonding. Various aspects of the SAM and multilayer crosslinked siloxane films were characterized and OLED devices based on SAM and spin-coated multilayer film-modified glass/ITO substrates were fabricated. The unique contact effects result in dramatic OLED device performance enhancement compared to that of devices without an interlayer. It is also demonstrated here that the crosslinking reaction between TPD-$[Si(OMe)_3]_2$ and ITO substrates as well as the intermolecular crosslinking within the TPD-$[Si(OMe)_3]_2$ siloxane network can be expedited by the presence of water and acetic acid in aqueous alcohol + acetic acid blend spin-coating solutions. The new relatively air-stable interlayer material developed here represents a effective approach to fabricating OLEDs with high brightness (maximum ~32, 800 cd/m^2), low operating voltage (~ 7 V at 300 cd/m^2), and high current efficiency (~ 5.8 cd/A), and should be suitable for real-world large-area coating conditions, such as roll-to-roll and ink-jet patterning processes.

CHAPTER THREE

Organic Light-Emitting Diodes Having Carbon Nanotube Anodes

1. Introduction

The exceptional electrical and mechanical properties of single-wall carbon nanotubes (SWNTs) have now been firmly established through extensive experiments[1-6] performed on individual SWNTs. Nevertheless, key manufacturability and system integration challenges must be surmounted before full exploitation of the unique SWNT attributes is possible. A two-dimensional random network of such SWNTs is one obvious – and perhaps the most straightforward – avenue whereby statistical averaging leads to highly reproducible networks that can be fabricated at precisely tuned NT densities. For this reason, SWNT thin films cast from aqueous solutions containing various surfactants have attracted much recent attention.[7-13] These networks are transparent and highly conducting with excellent mechanical properties. Hence, there is growing interest in SWNT thin films for applications in the area of macroelectronics and optoelectronics where flexible, transparent, and conductive coatings together with simple and cheap room temperature fabrication are required. To date, several types of devices based on thin SWNT films such as flexible transparent transistors,[14-17] optical modulators,[10] LEDs with SWNT films as p-type ohmic contacts,[18] and flexible emitter arrays[19] have been fabricated.

Theoretical and experimental studies have also established the work function of SWNT networks to be in the 4.7-5.2 eV range.[20,21] Such high work functions meet the requirement for anodes in several types of photonic devices, such as organic light-emitting diodes and organic solar cells. These characteristics and the simple room temperature fabrication avenue, together with other attributes such as excellent mechanical flexibility, indicate that this type of novel anode is a promising candidate material for next-generation photonic device applications.

Polymer and small molecule-based organic light-emitting diodes (OLEDs) are rapidly approaching large-scale commercialization, driven by attractions such as low cost, fast response,

applications in large-area flexible displays, and propelled by advances in efficiencies and operational lifetimes.[22-25] OLEDs are "dual-injection" devices in which holes and electrons are injected from the anode and cathode, respectively, into an active molecular/macromolecular medium to produce, via exciton decay, light emission.[24] Although tin-doped indium oxide (ITO) is used in numerous opto-electronic applications, it has significant limitations for current and future generation OLEDs. Diffusion of oxygen into proximate organic charge transporting/emissive layers,[26,27] significant absorption in the blue region,[28] a relatively low work function (~4.7 eV),[29] and corrosion susceptibility[29] are just a few of the limitations. Note also that In is in relatively short supply and therefore expensive, presenting significant challenges for large-scale introduction of next-generation display and photovoltaic technologies.[30]

In this paper, we describe the fabrication of flexible polymer-based OLEDs using SWNT films as anodes. We examine the response characteristics and report that for polymer-based OLEDs, the luminous performance is close to that required for applications such as home television. Recently, a polymer-based OLED using an oriented *multiwalled* nanotube film anode on glass or polymer substrates was reported. The performance is well below what we report here.[31]

2. Experimental

2-1. Fabrication of Transparent, Conducting Single-Walled Carbon Nanotube Films on PET.

The process for fabricating transparent, conducting single-walled carbon nanotube films on PET substrates by filtration and transfer printing has been described previously.[32] SWNT powders purchased from Carbon Solutions Inc. are suspended in water with the surfactant SDS,

followed by sonication and filtering. Washing with de-ionized water removes the SDS. A PDMS-based method[32] is then applied to transfer the nanotube films onto PET substrates.

2-2. Polymer-based OLED Fabication Having Carbon Nanotube Anodes.

For polymer-based OLED fabrication, a polymer blend hole-transporting layer (HTL) composed of a cross-linkable, hole-transporting organosiloxane material such as TPD-Si_2[34] and a hole-transporting polymer such as TFB (Fig. 2), which also serves as an effective PLED electron-blocking layer (EBL),[35,36] was spin-coated onto a clean carbon SWNT film or onto a PEDOT-PSS-coated carbon SWNT film to form a double-layer HTL. These HTL films were then dried in a vacuum oven at 90ºC for 1-2 hr. PEDOT-PSS (Baytron P) was spin-coated onto the SWNT film at 2500 rpm for 1 min, followed by drying at 120ºC for 8 min. Alternatively, a mixture of PEDOT-PSS and methanol (Baytron P: MeOH = 1:2)[37] was spin-coated onto the SWNT film at 600 rpm for 1 min, then at 2500 rpm for 1 min, followed by drying at 120ºC for 2 hr in a vacuum oven. Next, a well-balanced charge transport/emissive layer (EML), a TFB + BT blend (TFB:BT = 1:4), or a electron-dominated EML, BT, was spin-coated onto the HTL-coated substrates from xylene solution, resulting in an EML thickness of ~70 nm.[35] The resulting films were then dried in a vacuum oven at ~ 90ºC overnight. Inside an inert-atmosphere glove box, CsF and Al were thermally evaporated onto the EML at $<10^{-6}$ Torr using a shadow mask to define the 2 mm × 5 mm electrode areas. The resulting PLEDs were characterized inside a sealed aluminum sample container under a dry N_2 atmosphere using a computer-controlled Keithley 2400 source meter and an IL 1700 Research Radiometer equipped with a calibrated photodetector.[35,36] PLED lifetime measurements were carried out using a computer-controlled Keithley 2400 source meter and an IL1400A International Light Radiometer/Photometer inside a sample container continuously purged with N_2 gas at room temperature.

3. Results and Discussion

In section 3.1, we discuss the characterization of transparent, conducting carbon nanotube films. In section 3.2, EL responses of four different PLED devices having carbon nanotube anodes are discussed. The PLED EL responses are improved by addition of PEDOT-MEOH hole injection/transport layer and electron-rich emissive layer. At last, the life time measurement of PLEDs having carbon nanotube anode is shown here, and the advantages of this novel type of anode over conventional ITO are discussed.

3-1. Characterization of Carbon Nanotube Films. *Morphology, Sheet Resistance, and Transmittance.* Fig. 1A shows an AFM image of a transferred SWNT film on PET. The films have highly nanoporous structures, with specific surface areas as large as 1500 m^2/g. The RMS roughness is 8-10 nm.

Transmittance measurements in the visible and infrared were carried out with a Beckman Coulter DU 640 spectrophotometer. Transmittance is only weakly dependent on the wavelength (Fig. 1B), in accord with the neutral color of the film. For SWNT sheets having different thicknesses, sheet resistance and transmittance are related by eq. 1[11]:

$$T = \left(1 + \frac{1}{2R_s}\sqrt{\frac{\mu_0}{\varepsilon_0}}\frac{\sigma_{op}}{\sigma_{dc}}\right)^{-2} = \left(1 + \frac{188(\Omega)}{R_s}\frac{\sigma_{op}}{\sigma_{dc}}\right)^{-2} \qquad (1)$$

where the sheet resistance $R_s = 1/\sigma_{dc}t$, t is the film thickness, and the optical conductivity σ_{op} = 200 S/cm[33]. It has been shown that the optical conductivity in the visible depends only on the overall network density, while dc conductivity – and thus the measured sheet resistance – is strongly dependent on factors such as nanotube-nanotube connectivity, tube length, etc. The sheet resistance and transmittance of films at 550 nm having varying thickness (Fig. 1C) are

Figure 1. (A) AFM image of a transferred SWNT film on a PET substrate, showing the high pore density. The average diameter of each bundle is ~ 4-6 nm. (B) Transmittance vs wavelength in the visible and near-infrared regions for SWNT films. The inset shows a photograph of a transferred SWNT film on a flexible PET substrate with 120 Ω/□ sheet resistance. (C) DC sheet resistance vs transmittance of SWNT films at 550 nm for various NT densities; the line shows the fit to eq. 1 with $\sigma_{dc} = 12\sigma_{op}$, giving σ_{dc} = 2400 S/cm.

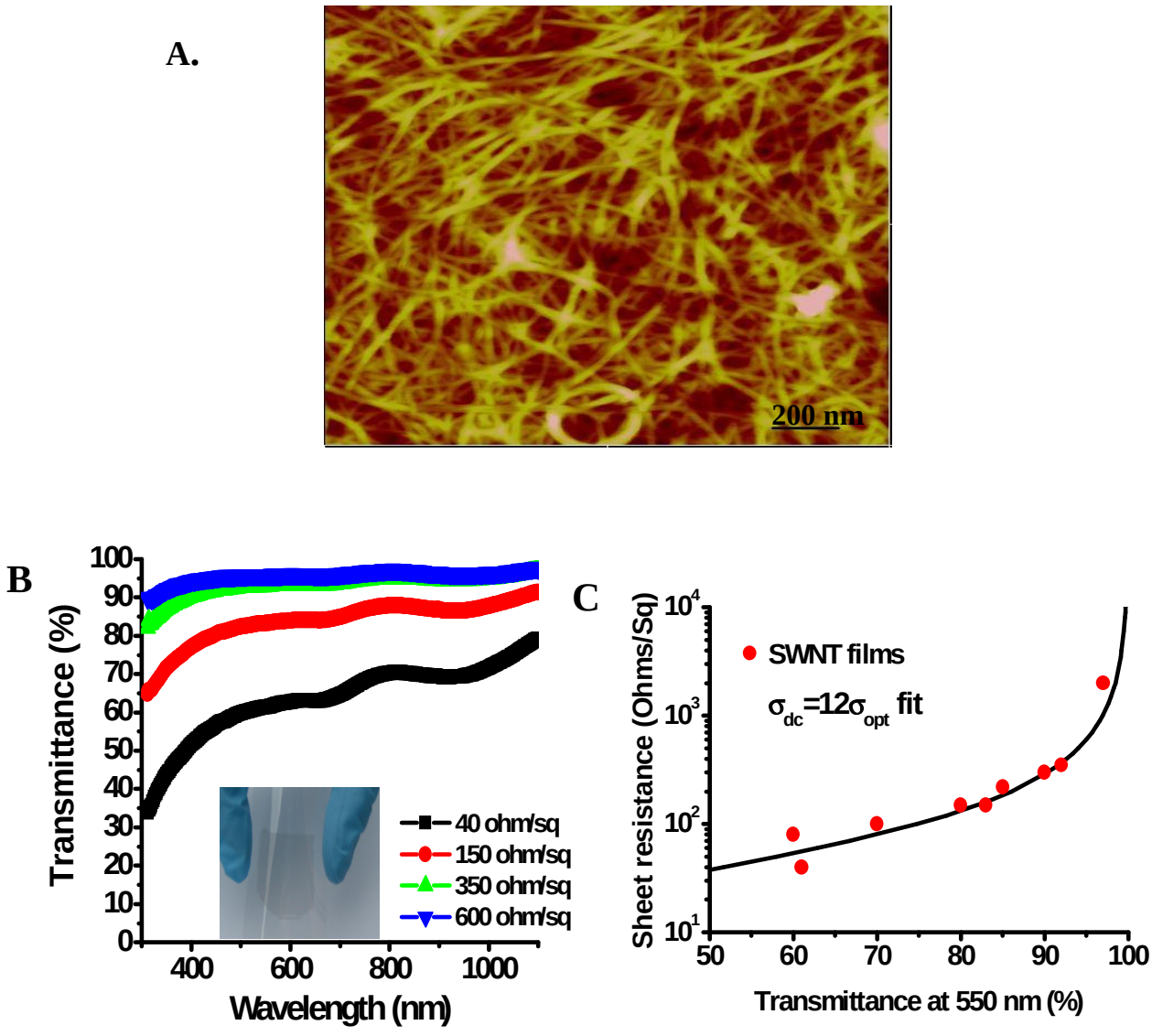

Figure 2. (A) Chemical structures of poly(9,9-dioctyl-fluorene-co-N-(4-butylphenyl) diphenylamine) (TFB), poly(9,9-dioctylfluorene-co-benzothiadiazole) (BT), poly(3,4-ethylenedioxythiophene) (PEDOT), and 4,4'-bis[(p-trichlorosilylpropylphenyl)phenylamino] biphenyl (TPD-Si_2). (B) Structure of a PLED device having a carbon SWNT film anode.

A.

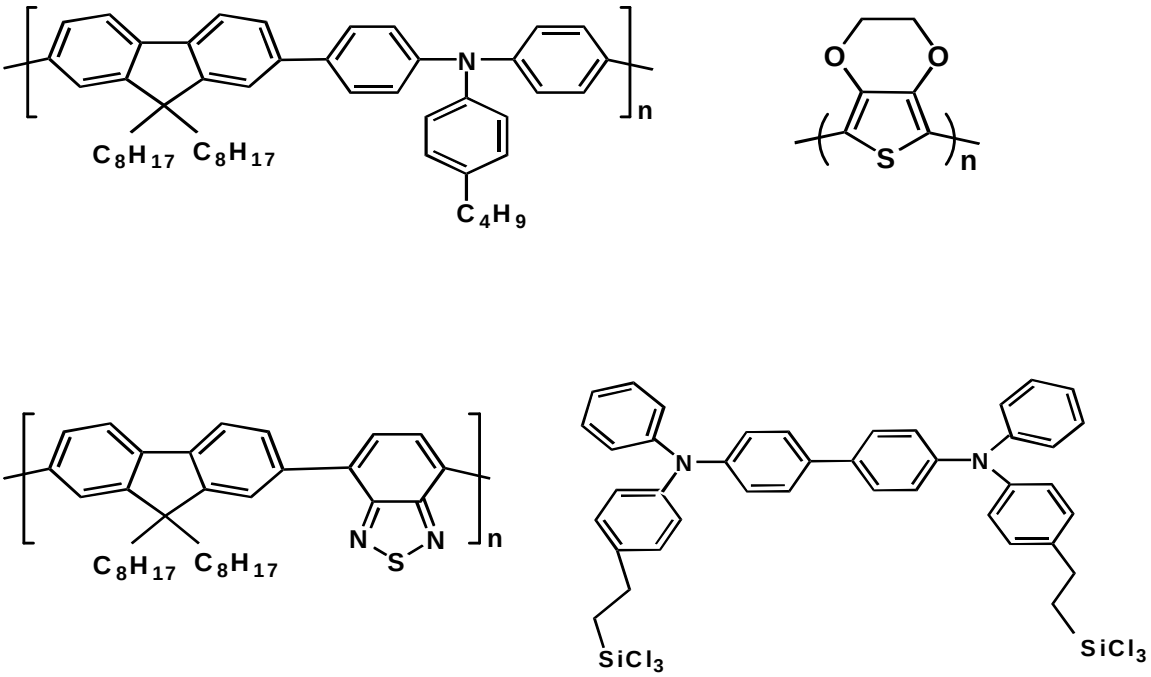

B.

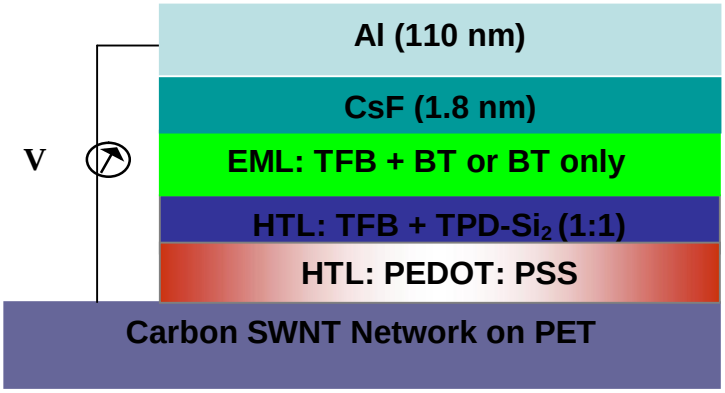

described well by eq. 1, leading to σ_{dc} = 2400 S/cm by using σ_{op} = 200 S/cm.

3-2. PLEDs Having Carbon Nanotube Anodes.

The four PLED device multilayer structures characterized in this work were: SWNT/TFB + TPD-Si_2/TFB + BT/CsF/Al (device 1), SWNT/PEDOT-PSS/TFB + TPD-Si_2/TFB + BT/CsF/Al (device 2), SWNT/PEDOT-PSS: MeOH/TFB + TPD-Si_2/TFB + BT/CsF/Al (device 3), and SWNT/PEDOT-PSS: MeOH/TFB + TPD-Si_2/BT/CsF/Al (device 4). The current density, luminance, and current efficiency vs. bias responses for these four device structures are compared in Figs. 4 and 5. The PLED with PEDOT-PSS: MeOH and TFB + TPD-Si_2 as a double-layer HTL (device 3) exhibits a low turn-on voltage of 5.0 V, a maximum luminance of 1000 cd/m^2, and a maximum current efficiency of 0.85 cd/A – a greater than 3-fold increase in maximum luminance, a ~50% lower turn-on voltage, and much greater current efficiency than the device having TFB + TPD-Si_2 only as the HTL (device 1). This may reflect the tendency of PEDOT-PSS to planarize the SWNT films while acting as a hole-transporting and buffer layer, decreasing the hole-injection barrier from the SWNTs (the PEDOT-PSS work function straddles that of SWNTs and TFB-TPD-Si_2) and minimizing device leakage currents. Furthermore, device 3 exhibits a 2 fold increase of maximum luminance and current efficiency compared with the device having spin-coated PEDOT-PSS only (device 2). This may reflect the greater tendency of PEDOT-PSS + MeOH to planarize and wet the SWNT films. The RMS roughness of the SWNT film spin-coated with PEDOT-PSS: MeOH is 0.96 nm by AFM (Figure 3) – significantly smoother than that of the SWNT film spin-coated with PEDOT-PSS only (4 nm).

For the SWNT/TFB + TPDSi_2/TFB + BT/CsF/Al structures, rectification in the J-V curve is clearly observed, with a maximum luminance of 10 cd/m^2 and a turn-on voltage of 12 V.

Figure 3. (A) AFM image of SWNT film with a spin-coated PEDOT-PSS overlayer. The RMS roughness is 4 nm from the AFM image. (B) AFM image of SWNT film with a spin-coated PEDOT-PSS: MeOH (1:2) overlayer. The RMS roughness is 0.96 nm from the AFM image.

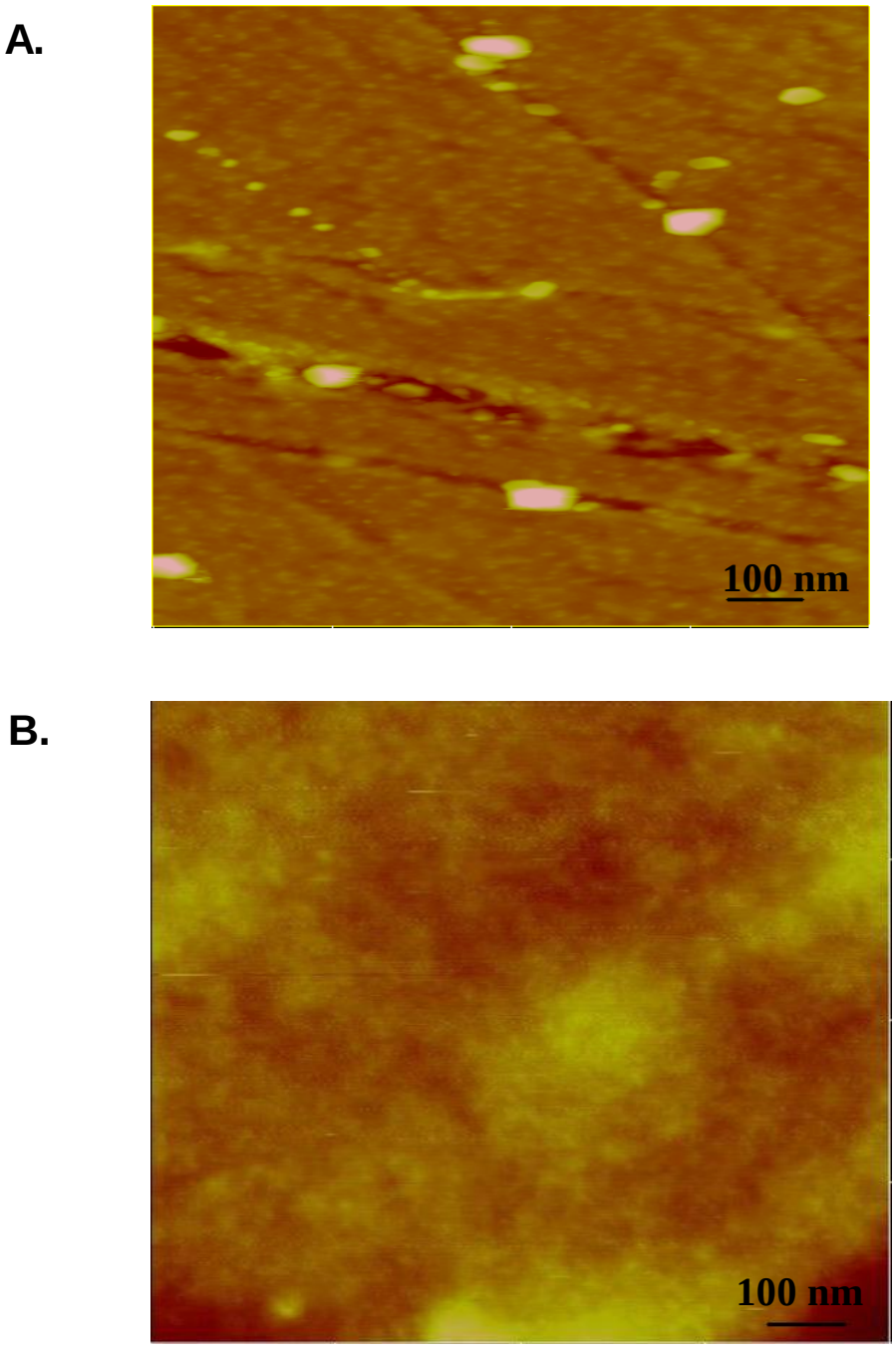

Figure 4. Response characteristics of PLEDs having the structures: (Device 1) SWNT(30 nm)/PEDOT-PSS:MeOH(30 nm)/TFB + $TPDSi_2$(25 nm)/TFB + BT(70 nm)/CsF/Al, (Device 2) SWNT(30 nm)/PEDOT-PSS(30 nm)/TFB + $TPDSi_2$(25 nm)/TFB + BT(70 nm)/CsF/Al, and (Device 3) SWNT(30 nm)/TFB + $TPDSi_2$ (25 nm)/TFB + BT (70 nm)/CsF /Al. (A) current density versus voltage; (B) luminance versus voltage; (C) current efficiency versus voltage.

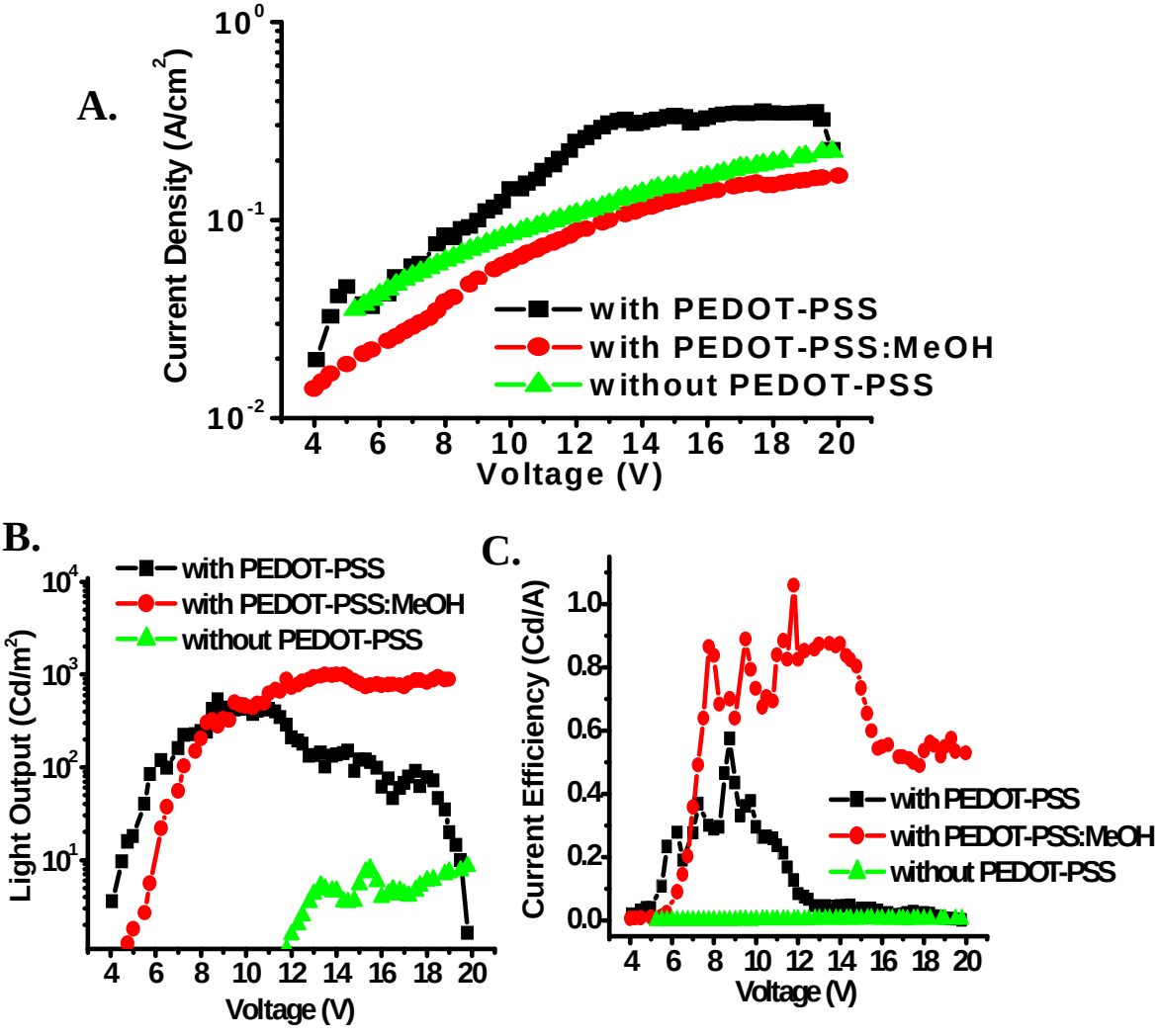

In contrast, SWNT/PEDOT-PSS: MeOH/TFB + $TPDSi_2$/TFB + BT/CsF/Al devices with spin-coated PEDOT-PSS as the hole injection layer exhibit orders of magnitude improvements in these parameters. The maximum luminance is 1000 cd/m^2, the turn-on voltage is ~ 5.0 V, and the maximum current efficiency is ~ 0.85 cd/A. This dramatic enhancement in device metrics with PEDOT-PSS incorporation is likely due to several factors. First, PEDOT-PSS better wets the SWNT films than does TFB-$TPDSi_2$; Second, PEDOT-PSS: MeOH better planarizes the SWNT films; and finally PEDOT-PSS, as hole transport layer, straddles the work functions of the SWNT films and TFB-$TPDSi_2$, thus facilitating hole injection.

In addition, as shown in Fig 5, the performance of PLED device 4 based on an electron-dominated EML (BT) and an electron-blocking HTL (the TPD-Si_2 + TFB + PEDOT-PSS double layer) affords a maximum luminance = 3500 cd/m^2, and a maximum current efficiency = 1.6 cd/A, surpassing that of PLED device 3 based on a TFB+BT blend EML (TFB+BT blends are known to exhibit better balanced electron-hole transport than the BT-only EMLs). This result can be understood as follows. First, better balanced electron and hole fluences may be obtained in these PLED devices with BT-only EMLs. SWNT anode films have large surface areas, resulting in greatly enhanced hole injection.[37] Hence, greater electron-hole recombination density at the HTL/EML interface in the BT-based devices vs. the TFB+BT-based devices should yield greater current efficiency and luminance. It will be seen below that longer device lifetimes are also achieved in the charge-balanced PLED device with the BT-only EML, consistent with more efficient electron-hole recombination. Furthermore, the peak recombination zone of the TFB+BT-based device should be located near the middle of the TFB+BT EML, and the relatively short distance between the peak recombination zone and the Al cathode may lead to cathode–induced exciton quenching. For the BT-based device, however, the peak recombination zone

Figure 5. Response characteristics of PLEDs having the structures: (Device 3) SWNT(30 nm)/ PEDOT-PSS:MeOH(30 nm)/TFB + $TPDSi_2$ (25 nm)/TFB + BT (70 nm)/CsF/Al and SWNT(30 nm)/ PEDOT-PSS:MeOH(30 nm)/TFB + $TPDSi_2$ (25 nm)/ BT (70 nm)/CsF/Al. (A) current density versus voltage; (B) luminance versus voltage; (C) current efficiency versus voltage.

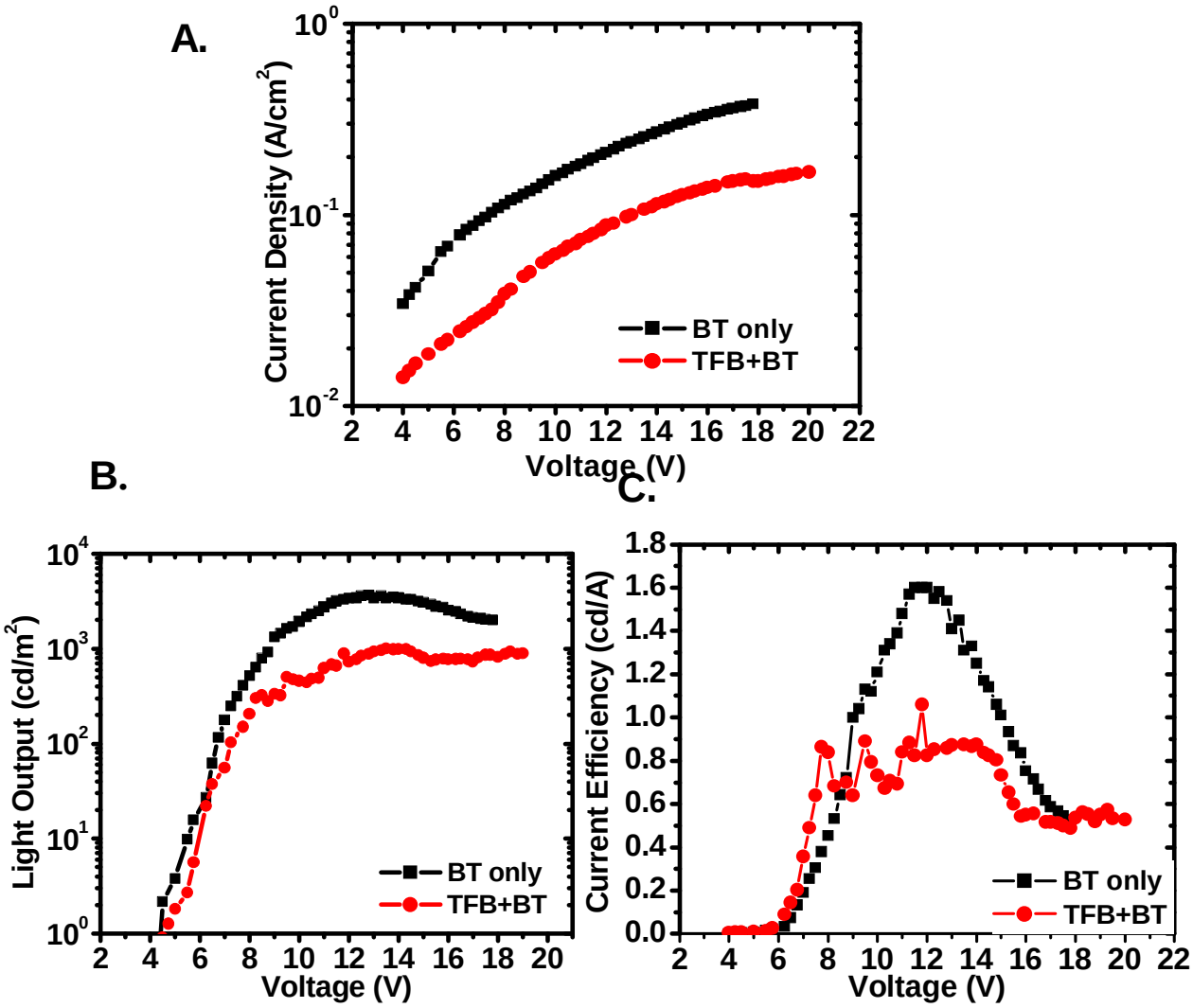

should be located nearer the TPD-Si_2 + TFB/BT interface, leading to less cathode-induced exciton quenching.

The light output of 3500 cd/m^2 achieved by the present SWNT-based PLED meets the requirements for many display applications, where light intensities of 100-300 cd/m^2 are required.[38] Although the present device metrics (luminance and current efficiency) do not match those found for devices using ITO anodes in similar structrues[36], the low turn-on voltage and brightness achieved are encouraging, especially taken together with the three-dimensional nature of hole injection and the SWNT film mechanical flexibility.

3-3. Life Time Measurement of PLEDs Having Carbon Nanotube Anodes

We evaluated the lifetimes of the SWNT-based PLEDs. The operational lifetime of device 4 was obtained under DC (continuously ON) conditions with a 0.12 A/cm^2 constant current density at room temperature, under a dry N_2 purge. The lifetime was found to be ~ 55 hrs with 1200 cd/m^2 initial luminance (L_0; Fig. 6 A). For comparison, an ITO/PET-(purchased from CP Films Inc., sheet resistance = 200 Ω/□, ~ 3 nm RMS roughness) based PLED device having the same configuration as device 4 was fabricated in parallel. The ITO/PET-based control device, which has a maximum light output of 20,000 cd/m^2 and a maximum current efficiency of 6 cd/m^2, exhibits a comparable operational lifetime of ~ 52 hr with L_0 = 1400 cd/m^2 (Fig. 6B) under identical measurement conditions. Note that all lifetime data were obtained from unencapsulated devices.

Although the output parameters of the present SWNT-based PLEDs are modest at this stage compared to ITO-based PLEDs,[36] our results suggest potential as ITO alternatives for several reasons. 1) SWNT films on PET exhibit sheet resistances of 120 Ω/□ with 80%

Figure 6. Life time characterization of PLEDs having the structures: (A) SWNT on PET/PEDOT-PSS:MeOH(30 nm)/TFB + $TPDSi_2$(25 nm)/BT(70 nm)/CsF(1.8 nm)/Al, and (B) ITO on PET/PEDOT-PSS:MeOH(30 nm)/TFB + $TPDSi_2$(25 nm)/BT(70 nm)/CsF(1.8 nm)/Al.

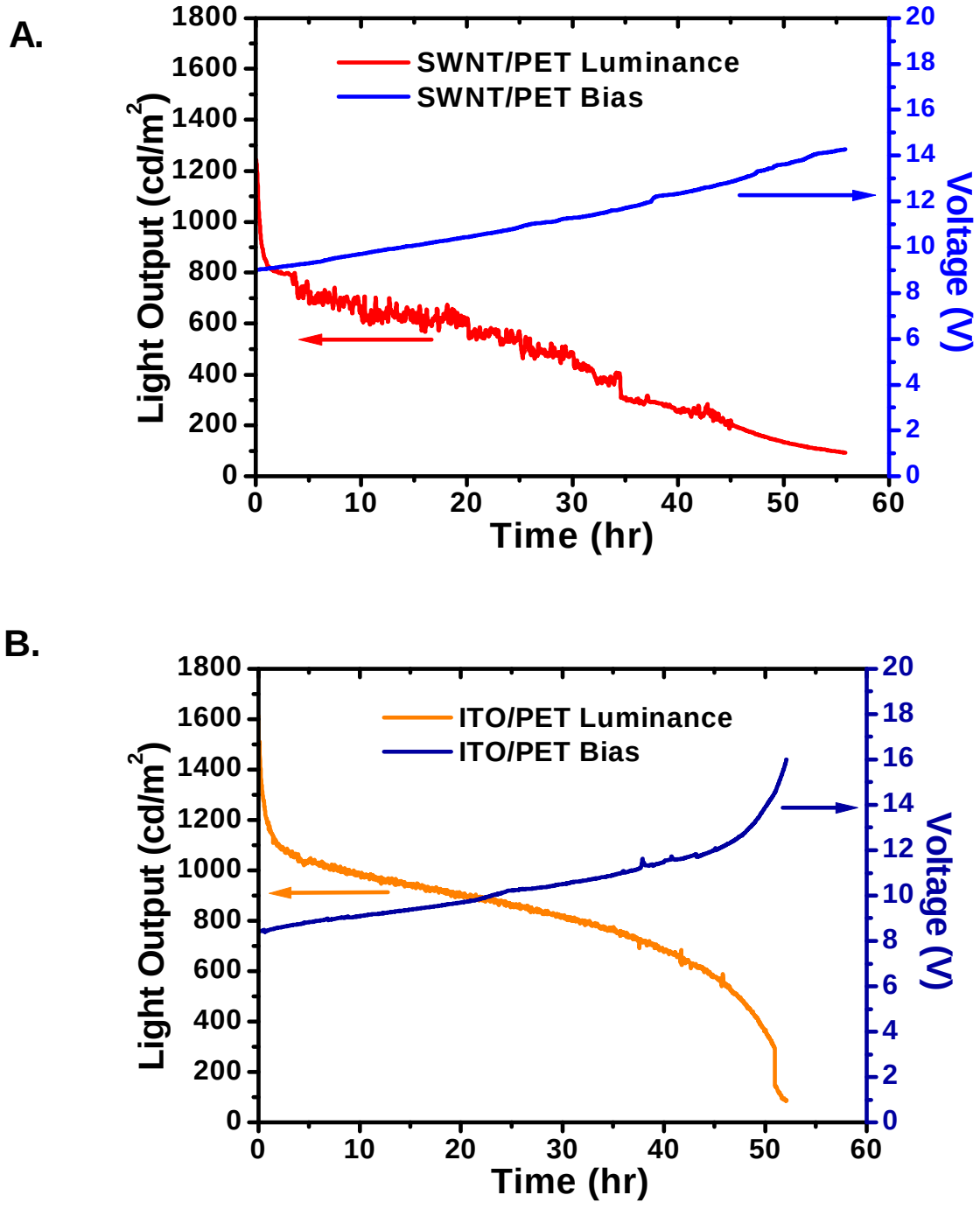

transmittance, metrics comparable to commercial ITO on plastic. By doping SWNT films with NO_2, a 3-fold decrease in sheet resistance without change of transparency can be expected.[39] 2) The exceptional mechanical flexibility of SWNT films has been demonstrated[15,16]. In contrast, ITO films on plastic crack after repeated bending. As shown by Sarran et al.[12] and also by us, SWNT films on PET do not crack or crease after bending, while ITO films become insulating. 3) SWNT films on PET exhibit good acid resistance, while ITO is quickly corroded, even by PEDOT-PSS solutions.[22,29] 4) Due to excellent surface energy matching, SWNT films adhere strongly to PET and PMMA, passing the "Scotch tape" decohesion test. 5) SWNT films, due to the nanoporous structure, have surface areas as great as 1500 m^2/g, offering hole injection potential. 6) SWNT film fabrication on PET, starting from SWNT powders, is a room temperature process and relatively simple, while ITO deposition on flexible substrates requires vacuum and elaborate process equipment. Room temperature processing renders the SWNT films suitable for use with a wide range of substrates for both top and bottom emission devices.

4. Conclusions

Single-walled carbon nanotube (SWNT) films on flexible PET (polyethyleneterephthalate) substrates are used as transparent, flexible anodes for organic light-emitting diodes (OLEDs). For polymer-based OLEDs having the structure: SWNT/PEDOT-PSS: MeOH/TFB (poly(9,9-dioctyl-fluorene-co-N-(4-butylphenyl)diphenylamine)) + TPD-Si_2 (4,4'-bis[(p-trichlorosilylpropylphenyl)phenylamino]biphenyl) /BT (poly(9,9-dioctylfluorene-co-benzothiadiazole))/CsF/Al, a maximum light output of 3500 cd/m^2 and a current efficiency of 1.6 cd/A have been achieved. The device operational lifetime is comparable to that of devices with Sn-doped In_2O_3 (ITO)/PET anodes. The advantages of this novel type of anode over conventional ITO are discussed.

CHAPTER FOUR

Highly Transparent and Conductive Carbon Nanotube-Indium Tin Oxide Double-layer Thin Films as Anodes for Organic Light-Emitting Diodes

1. Introduction

Small-molecule organic and polymer light-emitting diodes (OLEDs) are generating excitement due to their applicability in large-area flat panel displays and solid state lighting.[1] It is well known that the performance, lifetime, and durability of OLEDs are greatly influenced by charge injection from the anode and cathode.[2] Tin-doped indium oxide (ITO), with electrical conductivity and visible range transparency of $3\text{-}5\times10^3$ S/cm and 85-90%, respectively, is currently the most widely used transparent anode material for OLEDs. However, the rising cost of In and other significant ITO limitations raise challenges for large-scale introduction of next-generation optoelectronics.[3-6] Therefore, extensive efforts are being dedicated to finding superior low/no-In anode materials having high conductivity and a broad transparency window, comparable to that of ITO.[7-10]

Recently, a class of electronic thin-film materials based on random carbon nanotube (CNT) networks having excellent optical transparencies (40%-90%) and electrical conductivity (~1×10^4 S/cm), has been explored[11,12] for applications where low sheet resistance (*Rs*) and high optical transparency (*T*) are essential. These films are fabricated by solution processing, use abundant materials, and are mechanically flexible. Moreover, their intrinsic work function (4.5-5.2 eV)[13,14] is similar to that of ITO (4.4-4.9 eV)[15]. Previous work demonstrated CNT films as anodes for OLEDs[16-18] and organic photovoltaics (OPVs)[19,20] due to their high work function. In OPVs, CNT film anodes exhibit superior mechanical performance with comparable light harvesting efficiency to devices using conventional ITO anodes.[20] However, in OLEDs, CNT-based devices exhibit less than optimum performance versus ITO-based controls. For example, the maximum light output intensity in OLEDs with CNT anodes is at least 10× less than those with ITO

anodes,[16,18] which may reflect the relatively high CNT film sheet resistance, poor wetting and adhesion of the deposited active organic layers on the hydrophobic CNT surface, and non-uniform charge injection efficiency from the relatively rough CNT surfaces (RMS roughness ~ 10 nm), which may lead to shorting. The conducting polymer PEDOT-PSS[16] (a doped polythiophene polystyrene sulfonate) and a parylene-C[17] buffer layer have been applied to address these issues for CNT anodes in polymer and small-molecule OLEDs, respectively, and significantly enhance CNT-based device performance.

To achieve greater conductivity with greater transparency and multifunctionality, double-layer electrodes have been incorporated in optoelectronics. For example, Au/ITO-double layer electrodes facilitate ohmic contact and therefore decrease OLED turn-on voltage.[21] Kawashima, *et al*. reported that F-doped SnO_2-coated ITO exhibits improved thermal stability versus ITO, with conductivity retained during solar cell processing at 400-600 °C.[22] For CNT electrodes, ITO is a natural choice for fabricating double-layer anodes due to perfect matching of work functions. Here we report a simple/efficient double-layer strategy for ITO/CNT thin film growth. The attractions of such double-layer materials include: (1) lower sheet resistance with great optical transparency, (2) smoother surface morphology, (3) tunable work function, (4) better wettability and charge injection uniformity, (5) encapsulation of potentially non-benign materials, (6) greater environment stability, (7) lower materials cost, and (8) simple film growth process applicable to other double-layer transparent conducting oxide (TCO)/CNT structures.

To avoid damaging single-walled carbon nanotube (SWNT) films on flexible PET (polyethyleneterephthalate) substrates, a low-temperature ITO film deposition technique is required. In contrast to simple room temperature oxide sputtering, which typically produces

amorphous films with poor conductivity, transparency, and adhesion properties, ion-assisted deposition (IAD) is a unique growth technique which employs two ion beams to simultaneously achieve film deposition, oxidation, and crystallization, resulting in smooth, adherent and microstructurally dense oxide thin films on a variety of substrates at room temperature.[23] In addition, ITO thin film microstrctural, electrical, and optical properties can be finely tuned by the growth system O_2 partial pressure and ion beam power.[23]

To date, there have been no reports of OLED fabrication with TCO layer-modified CNT double-layer anodes. We report here the growth, electrical, and optical properties of double-layer ITO/CNT thin films. A thin ITO layer is overcoated on CNT thin films by IAD to "engineer" CNT surface properties and to tune the work function. These double-layer films are then implemented in polymer light-emitting diodes (PLEDs). It is found that ITO/CNT thin films, with a lower sheet resistance, smoother surface, and higher figure of merit ($\Phi = T^{10}/R_{sheet}$, where T = average transmittance from 400 to 700 nm) than that of CNT films, yield enhanced PLED performance versus CNT-only-based devices and comparable PLED performance to commercial ITO-based devices having similar structures.

2. Experimental

The process of fabricating transparent, conducting SWNT films on PET substrates by filtration and transfer printing has been described previously.[24] SWNT powders are suspended in water with the surfactant SDS, followed by sonication and filtering. Washing with de-ionized water removes the SDS. A PDMS-based method is then applied to transfer the nanotube films onto PET substrates. The SWNT films have highly nanoporous structures, with specific surface areas as large as 1500 m^2/g. Scanning electron microscopy of a continuous SWNT thin film

deposited on PET (Fig. 1) reveals that the SWNTs are distributed uniformly on the PET surface, while the presence of voids illustrates the 3-dimensional nature of the film. The RMS roughness is ~12 nm, as determined by the AFM (Fig. 2a). The as-deposited SWNT films were then transferred to an IAD chamber for ITO overcoating using an In_2O_3: SnO_2 = 9:1 target purchased from Sputtering Materials Inc. During ITO deposition, the O_2 partial pressure and the thin film growth rate were optimized at 1.1×10^{-4} Torr and 1.8 nm min^{-1}, respectively. [23] ITO film thickness was monitored in situ using a calibrated quartz crystal balance.

The as-deposited CNT/ITO bilayer and CNT thin films on PET were next implemented in PLED fabrication using the structure, PET/CNT or CNT/ITO double-layered anode /PEDOT-PSS/TFB + $TPDSi_2$/BT/CsF/Al.[26] Here the poly (3,4-ethylenedioxy-thiophene)-polystyrene sulfonate (PEDOT-PSS) hole-injection/hole transport layer (HIL/HTL), which also can planarize the CNT and CNT/ITO bilayer surfaces, was first spin-coated onto the CNT/ITO bilayer and CNT anodes and cured at 120ºC overnight under vacuum. Next, a cross-linkable, HTL/electron-blocking layer (EBL) consisting of TPD-Si_2 (4,4'-bis[(p-trichlorosilylpropylphenyl) phenylamino]biphenyl) blended with the hole-transporting polymer TFB (poly(9,9-dioctyl-fluorene-co-N-(4-butylphenyl)diphenylamine)) (1:1 mass ratio) was spin-coated onto the PEDOT-PSS-coated anodes, followed by cross-linking to afford a robust, insoluble film. A third layer of the emissive polymer BT (poly(9,9-dioctylfluorene-co-benzothiadiazole)) was then spin-coated onto the HTL/EBL to form a multilayer heterostructure. Finally, inside an inert-atmosphere glove box, CsF and Al were thermally evaporated onto the EML at $< 10^{-6}$ Torr using a shadow mask to define the 2 mm × 5 mm electrode areas. Details of device fabrication are described elsewhere.[26]

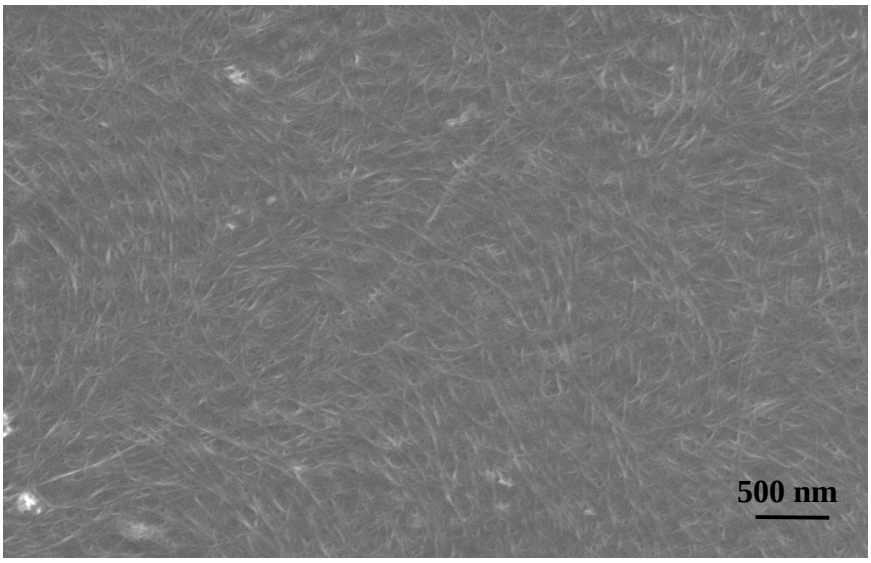

Figure 1. SEM image of a transferred SWNT film on a PET substrate, showing the high pore density. The presence of voids illustrates the 3-dimensional nature of the network.

3. Results and Discussion

3-1. Characterization of CNT/ITO-bilayer films. Morphology, Sheet Resistance, and Transmittance.

Smooth surface morphologies are required for OLED anodes both because "spikes" can cause breakdown/shorting and because subsequent upper device layers will assume the irregular anode morphology, adversely influencing stability and performance.[25] Figure 2 shows AFM images of the surface morphologies of CNT (30 nm), bilayer CNT/ITO-1 (CNT = 30 nm, ITO = 14 nm), bilayer CNT/ITO-2 (CNT = 30 nm, ITO = 30 nm), and bilayer CNT/ITO-3 (CNT = 30 nm, ITO = 45 nm) films. The root-mean-square (RMS) roughnesses of the CNT/ITO bilayer surfaces decreases with increased ITO film thickness. For example, the RMS roughness of CNT/ITO-3 surface is ~ 7 nm, less than that of CNT/ITO-1, ~ 11 nm. This may reflect the marked tendency of IAD-derived ITO to planarize the SWNT films, as shown in Table 1.

Figure 3 shows optical transmittance spectra of CNT, bilayer CNT/ITO-1, CNT/ITO-2, CNT/ITO-3 films. The CNT/ITO-3 film exhibits an average optical transmittance of 80.5% in the visible range (400-700 nm), somewhat less than that of an as-deposited CNT film, 86.2%. The average transmittance of CNT/ITO bilayers decreases as the ITO thickness increases. Optical transmittance, sheet resistance, and figure of merit ($\Phi = T^{10}/R_{sheet}$, T = average transmittance from 400 to 700 nm) data are summarized in Table I. The CNT/ITO bilayers sheet resistance decreases significantly as the ITO thickness increases. However, CNT/ITO-1 exhibits almost the same sheet resistance as CNT films, which may indicate that the 14 nm ITO film is not sufficiently thick to form a continuous, conductivity-enhancing film on the relatively rough CNT surface (RMS

roughness = ~11-13 nm). Note here that the CNT/ITO-3 double-layer films exhibit the highest figure of merit among all CNT/ITO bilayer and CNT films.

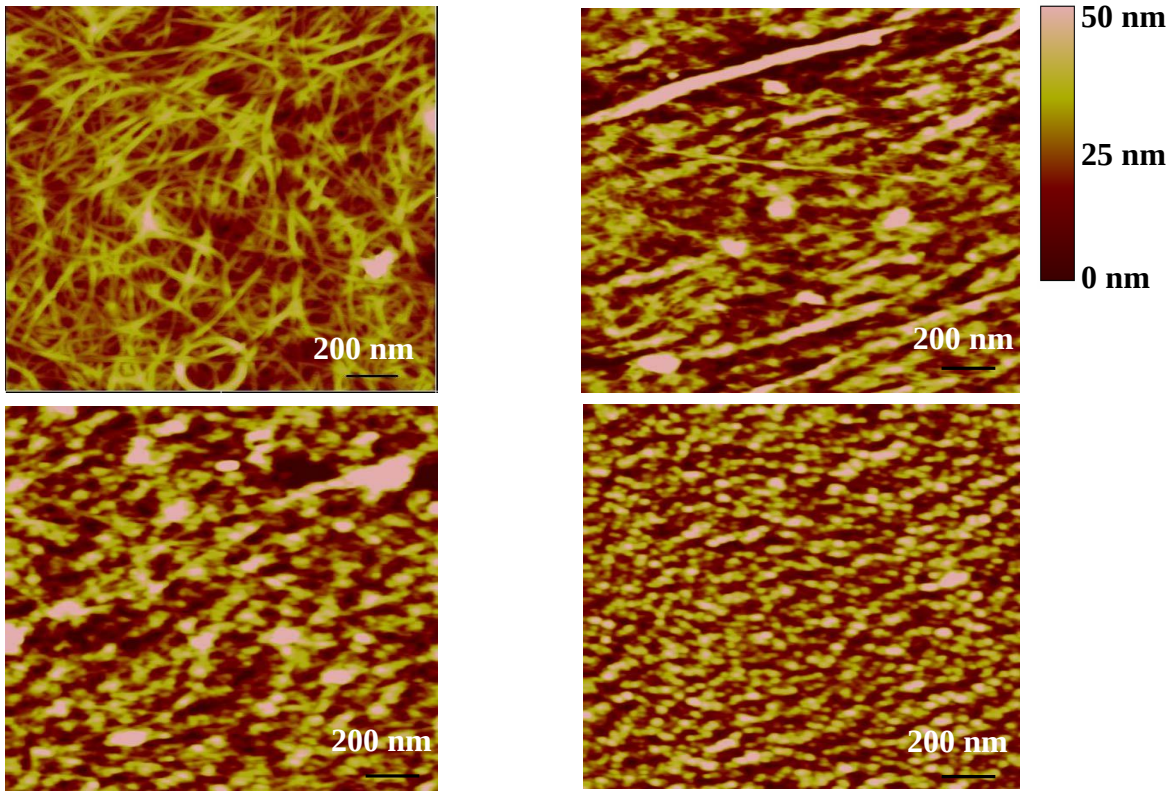

Figure 2. AFM images of : (a) a pristine SWNT film, (b) a SWNT film coated with a 14 nm IAD-derived ITO layer (CNT/ITO-1), (c) a SWNT film coated with a 30 nm IAD-derived ITO layer (CNT/ITO-2), and (d) a SWNT film coated with a 45 nm IAD-derived ITO layer (CNT/ITO-3).

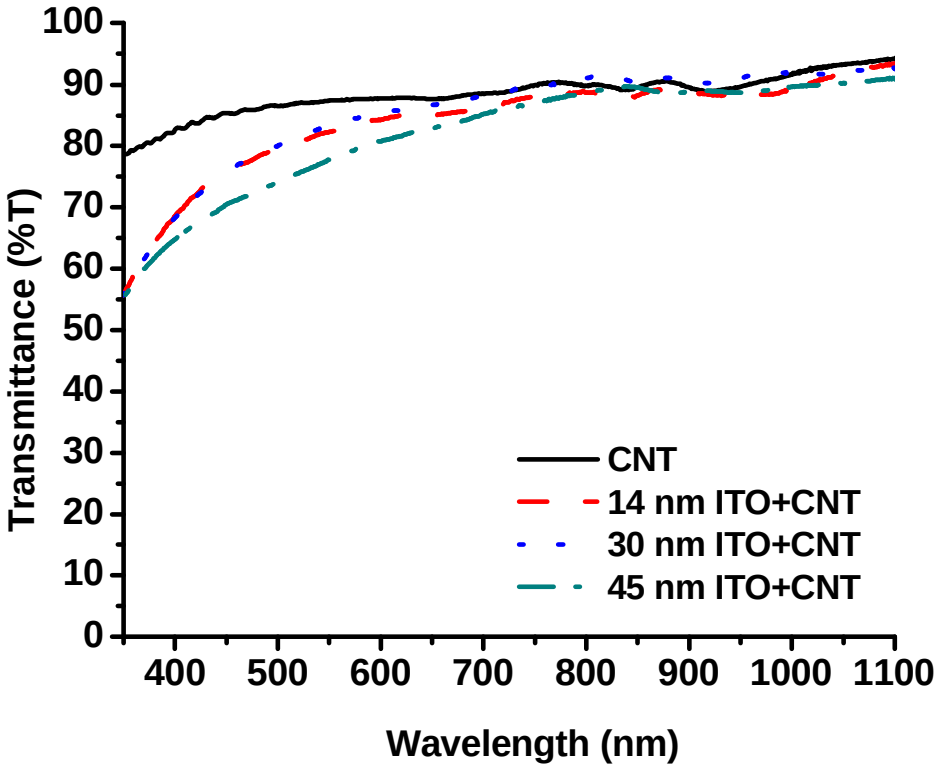

Figure 3. Optical transmittance spectra of CNT (30nm), CNT (30 nm)/ITO-1 (14 nm), CNT (30 nm)/ITO-2 (30 nm), and CNT (30 nm)/ITO-3 (45 nm) films.

Table 1. Properties of single-layered CNT and double-layered CNT/IAD-derived ITO thin films, and operating characteristics of PLEDs having the structure: CNT or CNT/ ITO double-layered anode /PEDOT-PSS/TFB + $TPDSi_2$/BT/CsF/Al.

Sample	Thickness (nm)	Sheet resistance (Ω/□)	Average Transmittance in 400-700 nm (%)	Figure of Merit $\Phi = T^{10}/R_{sheet}$ ($10^{-4}\Omega^{-1}$)	Surface Roughness (nm)	Turn-on Voltage (V)	Maximum Light output (cd/m^2)	Maximum current efficiency (cd/A) [voltage (v)]
CNT	30	350	86.2	6.3	11-13	4.3	3,050	1.6 (11.0)
CNT/ITO-1	30/14	345	83.1	4.5	~11	4.7	2,430	0.97 (11.5)
CNT/ITO-2	30/30	215	82.7	6.5	~8	4.0	4,380	2.1 (10.8)
CNT/ITO-3	30/45	150	80.5	8.1	~7	3.7	8,900	4.5 (10.5)

Figure 4. Response characteristics of PLEDs having the structures: SWNT(30 nm) or CNT/IAD-derived ITO double-layered anode /PEDOT-PSS(30 nm)/TFB + $TPDSi_2$(25 nm)/BT(70 nm)/CsF(1.8 nm)/Al. (a) current density versus voltage; (b) luminance versus voltage; (c) current efficiency versus voltage. Lines through the data points are drawn as a guide to the eye.

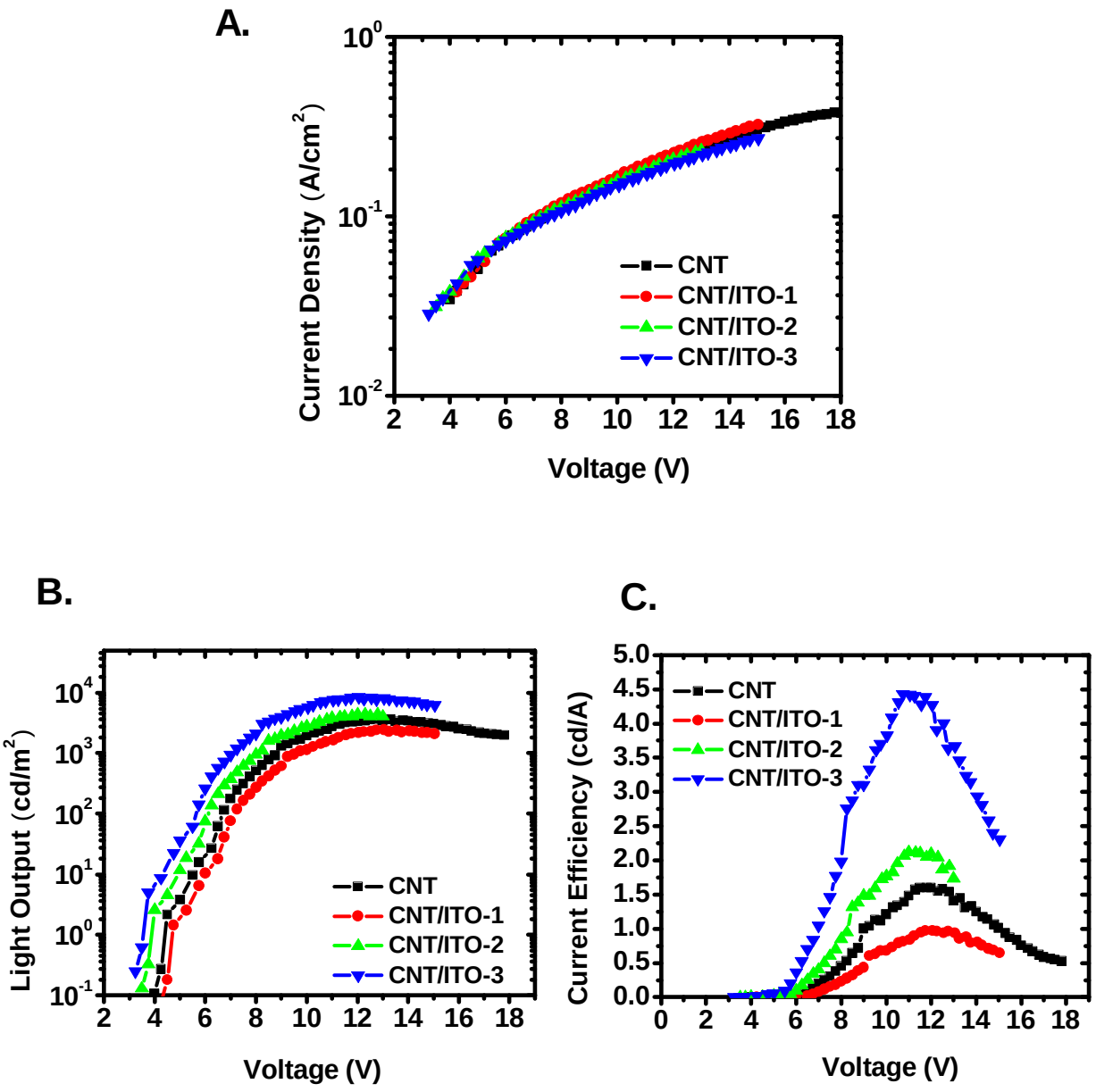

3-2. PLEDs Having the CNT/ITO Double-layered Anodes.

In parallel, PLEDs with an identical structure were fabricated using CNTs, CNT/IAD-derived ITO bilayers, and commercial ITO films (CP Films Inc., sheet resistance = 200 Ω/□, ~ 3 nm RMS roughness) on PET for comparison. Device steady-state light outputs and *J-V* characteristics of the PLED devices were measured under ambient atmosphere using instrumentation described elsewhere.[9,10] Current density, luminance, and current efficiency vs bias responses for PLEDs based on CNT and various CNT/ITO double-layered anodes are compared in Figure 4. Differences between various CNT/ITO bilayer and CNT control devices are attributed to differences in anode characteristics since all devices were fabricated simultaneously in a parallel. As seen in Fig. 4, CNT/ITO-3 anode PLEDs exhibit a turn-on voltage of 3.7 V, lower than that of the CNT/ITO-2 and CNT-based devices, 4.0 and 4.3 V, respectively, which may reflect the low CNT/ITO-3 sheet resistance. Note that CNT/ITO-3 has a 150 Ω/□ sheet resistance, lower than that of 215 and 350 Ω/□ for CNT/ITO-2 and CNT films, respectively. The PLED with CNT/ITO-3 as a double-layer anode exhibits maximum luminance of 8,900 cd/m^2, and maximum current efficiency of 4.5 cd/A at 10.5 V – a 3-fold increase of maximum luminance and current efficiency vs. the device having a CNT-only anode. This dramatic enhancement in device metrics likely reflects several factors. First, the wettability and adhesion of PEDOT-PSS on hydrophilic ITO surface are much greater than on the hydrophobic CNT surface. PEDOT-PSS, as hole transport/injection layer, straddles the work functions of the SWNT/ITO films and TFB-TPDSi$_2$, thus facilitating hole injection. Second, IAD-derived ITO planarizes the CNT surface, affording uniform hole injection from the CNT/ITO anode. CNTs with 50 nm ITO films exhibit the lowest rms roughness of 7 nm. Finally, IAD-derived ITO improves the conductivity of CNT

film. CNT/ITO-3 exhibits a sheet resistance of 150 Ω/□, which is ~60% lower than that of 350 Ω/□ for the CNT film. Note that the performance of CNT/ITO-3-based devices is approaches that of a commercial PET/ITO-based control device, which has a maximum light output of 13,000 cd/m^2 and a maximum current efficiency of 5.5 cd/A in the same device structure.

The performance of the PLED with CNT/ITO-1 double-layer anode is comparable to or inferior in performance of devices having CNT-only anodes, with a turn-on voltage of 4.7 V, a maximum luminance of 2,430 cd/m^2, and a maximum current efficiency of 0.97 cd/A. The presence of voids is an important factor in understanding this result. Close scrutiny of the SEM image in Fig. 1 reveals voids in the SWNT thin film 3-D network, indicating that 14 nm of IAD ITO is insufficient to form a continuous, conductive lattice on the relatively rough SWNT surface to improve the conductivity, while the film optical transmittance decreases with 14 nm ITO. As expected, CNT/ITO-based PLED performance is enhanced with increased IAD-derived ITO thickness.

4. Conclusions

In summary, double-layer transparent conducting CNT/ITO films were used as transparent anodes for PLED fabrication. The overall film figure of merit with 30 nm CNT and 50 nm IAD-derived ITO (CNT/ITO-3) is significantly greater than that of CNT-only films. Furthermore, CNT/ITO-3-based PLEDs exhibit superior performance to that of a CNT-only control and comparable performance to that of a commercial ITO device. Note that the CNT/ITO films have a lower In content than ITO, rendering them promising for large-area optoelectronics. In addition, high work function ITO alternative TCOs such as ZITO,[9,27] could be employed to further modify CNT film properties.

CHAPTER FIVE

Cyan and Green Light-emitting Diodes from a Fluorene-Based Copolymer

1. Introduction

Since the first polymer light-emitting diode (PLED) was made in 1990,[1] fluorescent conjugated polymers have attracted considerable interest because of their potential applications in flat-panel displays.[2-4] Extensive interdisciplinary research has been performed by scientists all over the world to develop high-efficiency, long lifetime, good color-purity light-emitting polymers. Solution processing of semiconducting polymers has the advantage of allowing spin-coating and printing methods to be utilized for the fabrication of large-area-display devices. In addition, PLEDs offer the flexibility of fine-tuning the luminescent properties of the device through manipulation of chemical structures. Many conjugated polymers whose emission wavelengths can be tuned to span the entire visible spectrum have been synthesized as components of potential polymer-based LEDs through simple copolymerization of appropriate monomers.[5-7]

Polyfluorene and derivatives have emerged as the dominant class of polymers for commercial PLED applications.[8,9] and there has been great success in producing highly efficient PLEDs using alternating copolymers having fluorene moieties. Indeed, a wide range of fluorene copolymers with fluorescence spanning the entire visible spectrum has been synthesized. No other class of fluorescent polymers offers such a wide range of color emission and has been incorporated into LEDs with high efficiency, low operating voltages, and long lifetimes.

In this work, we report the synthesis and characterization of a novel cyan emitting copolymer poly(2,5-N-*n*-octyl-3,4-cyclicimidothienyl-*co*-2',7'-9',9'-di-*n*-octylfluorene) (C8F8), consisting of electron-deficient cyclicimidothiophene and fluorene moieties. Here, we present the optical and luminescence properties of C8F8 and the blending of C8F8 with the electron-rich

copolymer poly(9,9-dioctyl-fluorene-co-N-(4-butylphenyl)diphenylamine) (TFB). We also discuss the performance of PLEDs fabricated with such films.

2. Experimental

2-1. Materials and Methods. All chemical reagents were used as received unless otherwise indicated. All manipulations of air/moisture-sensitive materials were carried out on a dual-manifold Schlenk line or in a nitrogen-filled glovebox. Ether and THF were distilled from sodium/benzophenone ketyl. Methylene chloride was distilled from calcium hydride. Toluene was dried using activated alumina and Q5 columns and was regularly tested with benzyphenone ketyl in ether solution. NMR spectra were obtained on Varian VXR-400 or 500 MHz NMR instruments, and MS analyses were conducted on a Micromass Quattro II Triple Quadrupole HPLC/MS/MS mass spectrometer. Elemental analyses were carried out by Midwest Microlab. UV-visible absorption spectra of SAM-coated quartz plates were obtained on a Cary 1E UV-vis spectrometer. Cyclic voltammetry was performed with a BAS 100 electrochemical workstation (polymer-coated Pt working electrodes, Ag wire pseudo-reference electrode, Pt wire counter electrode, 0.1 M TBAHFP in anhydrous MeCN supporting electrolyte, and 1.0×10^{-3} M ferrocene as an internal standard probe). TBAHFP was recrystallized from an ethyl acetate/hexanes mixture and dried in vacuo at 100 ^{o}C for 10 h. Ferrocene was purchased from Sigma-Aldrich and purified via vacuum gradient sublimation. Thermogravimetric analysis (TGA) was carried out on an SDT 2960 simultaneous DTA-TGA instrument (TA Instruments) with a scan rate of 10 °C/min under N2. Molecular weights of the polymers synthesized were measured vs polystyrene (PS) standards using a Waters room-temperature gelpermeation chromatography (GPC) system equipped with a

Waters 2410 refractive index detector and a Waters 515 HPLC pump. PL and EL spectra were recorded using a Photon Technology International model QM-2 fluorescence spectrometer.

2-2. Synthesis of 3,4-dicyanothiophene (1). A stirred suspension of 3,4-dibromothiophene (24.2 g, 0.1 mol) and copper(I) cyanide (26.0g, 0.29 mol) in dry DMF (25 mL) was refluxed under N_2 for 4 hr. The dark mixture was poured into a solution of hydrated ferric chloride (100 g) in hydrochloric acid (175 mL, 1.7 M) and maintained at 60-70°C for 1 hr. The mixture was let to cool down to room temperature, and methylene chloride (125 mL) was added and the layers were separated. The aqueous phase was extracted four times with 125 mL portions of methylene chloride. Organic phase was combined and was washed successively with two 100 mL portions of hydrochloric acid (6 M), water, saturated sodium bicarbonate solution, and finally with distilled water, followed by drying over MgSO4 over night. Solvent was evaporated to dryness to afford a pale yellow solid. Recrystallization from acetonitrile provided a white crystal (12.0 g, 90%). ^{1}H NMR (CDCl3) δ 8.0; 13C NMR (CDCl3) δ 136.8, 113.1, 111.8.

2-3. Synthesis of 2,5-dibromo-thiophene-3,4-dicarboxylic acid (2). A suspension of **1** (9.2 g, 68.6 mmol) in 100 mL concentrated HCl was refluxed for 6 hrs. Heating was removed and colorless crystal formed was collected via vacuum filtration. Recrystalization from water afforded a colorless crystal (9.85 g, 83%). To the crystal (1.0 g, 5.8 mmol) in 10 mL glacial acetic acid was added bromine (1.8 mL, 35 mmol) dropwise. The mixture was stirred over night and a colorless crystal was formed. The bromine was removed by adding saturated $NaHSO_3$ solution, and the precipitate was collected by filtration. Recrystalization from hot water followed by drying gives a colorless crystal (1.2 g, 63%). ^{13}C NMR ($CDCl_3$) δ 163.13, 134.63, 114.67.

2-4. Synthesis of 2,5-dibromothiophene-3,4-dicarboxylic acid dichloride (3). To 3 (1.0 g, 3.03 mmol) in 5 mL anhydrous benzene was added oxalyl chloride (1.1 mL, 12.2 mmol) and one drop of dry DMF. The mixture was heated to reflux for 1 hr, and allowed to cool to room temperature. The volatiles were removed *in vacuo* to afford 4 (1.0 g, 90%). The crude material was used without any further purification.

2-5. Synthesis of 3,4-N-(n-octylimido)-2,5-dibromothiophene (4a). 3 (1.0 g, 2.7 mmol) was mixed with n-octylamine (0.45 mL, 2.7 mmol) in a Schlenk reaction tube and heated to 140ºC for 30 min under vigorous stirring. The preparation was cooled to room temperature and chromatographed over silica gel with CH_2Cl_2:hexane (10:1) to afford a white powder (0.35 g, 31%). ^{1}H NMR ($CDCl_3$) δ3.59 (2H), 1.63 (2H), 1.30 (10H), 0.88 (3H); ^{13}C NMR ($CDCl_3$) δ 160.6, 135.0, 113.1, 39.0, 32.0, 29.3, 28.4, 27.0, 22.8, 14.3.

2-6. Synthesis of 3,4-N-(n-dodecylimido)-2,5-dibromothiophene (4b). 3 (1.0 g, 2.7 mmol) was mixed with n-dodecylamine (0.5 g, 2.7 mmol) in a reaction tube and heated to 140ºC for 30 min under vigorous stirring. The preparation was cooled to room temperature and chromtographed over silica gel with CH_2Cl_2:hexane (10:1) to afford a white powder (0.45 g, 50%). ^{1}H NMR ($CDCl_3$) δ3.55 (2H), 1.60 (2H), 1.20 (18H), 0.83 (3H); ^{13}C NMR ($CDCl_3$) δ 160.8, 134.9, 113.1, 38.7, 32.2, 29.8, 29.78, 29.7, 29.5, 29.4, 28.7, 27.1, 22.8, 14.3.

2-7. Poly(2,5-N-*n*-Octyl-3,4-cyclicimidothienyl-*co*-2',7'-9',9'-di-*n*-octylfluorene) (**9**). To a mixture of 9,9-di-*n*-octylfluorene-2,7-bis(ethyleneboronate) (0.53 g, 1.0 mmol), **4a** (0.42 g, 1.0 mmol) in toluene (8 mL) under nitrogen is added tetrakis(triphenylphosphine)palladium (20 mg), Aliquat 336 (85 mg), and 2M aqueous sodium carbonate (2 mL, 4 mmol). The mixture is stirred vigorously and heated at reflux 24 h. The highly viscous reaction mixture is poured into acetone (40 mL), precipitating a greenish polymer. The polymer is collected by filtration and

washed with more acetone, dissolved in toluene, and precipitated by methanol twice, and dried in vacuum to give a green solid (420 mg, 64%). GPC: M_w =15460, PD = 2.3; Anal. For $(C_{43}H_{57}NO_2S)_n$, calcd: C, 79.21; H, 8.81; N, 2.15; Found: C, 78.99; H, 8.91; N, 2.16; ^{1}H NMR ($CDCl_3$): δ 8.29, 8.24, 7.87, 7.39, 3.76, 2.19, 1.76, 1.58, 1.40, 1.30, 1.20, 1.13, 0.90, 0.80 ppm.

2-8. Fabrication of Light-emitting Devices. ITO glass sheets (20 Ω/ο, rms roughness = 2.5 nm) were purchased from Colorado Concept Coating. For PLED fabrication, a polymer blend hole-transporting layer (HTL) composed of a cross-linkable, hole-transporting organosiloxane material such as TPD-Si_2 and a hole-transporting polymer such as TFB, which also serves as an effective PLED electron-blocking layer (EBL), was spin-coated onto a PEDOT-PSS-coated Sn-doped In_2O_3 (ITO) film on glass to form a double-layer HTL. These HTL films were then dried in a vacuum oven at 90ºC for 1-2 h. Prior to this, the PEDOT-PSS (Baytron P) had been spin-coated onto the ITO film at 2500 rpm for 1 min, followed by drying at 120ºC for 2 h. Next, a well-balanced charge transport/emissive layer (EML), a TFB + C8F8 blend (TFB: C8F8 =1:4), or an electron-dominated EML, C8F8, was spin-coated onto the HTL-coated substrates from chlorobenzene solution. The resulting films were then dried in a vacuum oven at ~ 90ºC overnight. Inside an inert-atmosphere glove box, CsF and Al were thermally evaporated onto the EML at $<10^{-6}$ Torr using a shadow mask to define 2 mm × 5 mm electrode areas. The resulting PLEDs were characterized inside a sealed aluminum sample container under a dry N_2 atmosphere using a computer-controlled Keithley 2400 source meter and an IL 1700 Research Radiometer equipped with a calibrated photodetector.

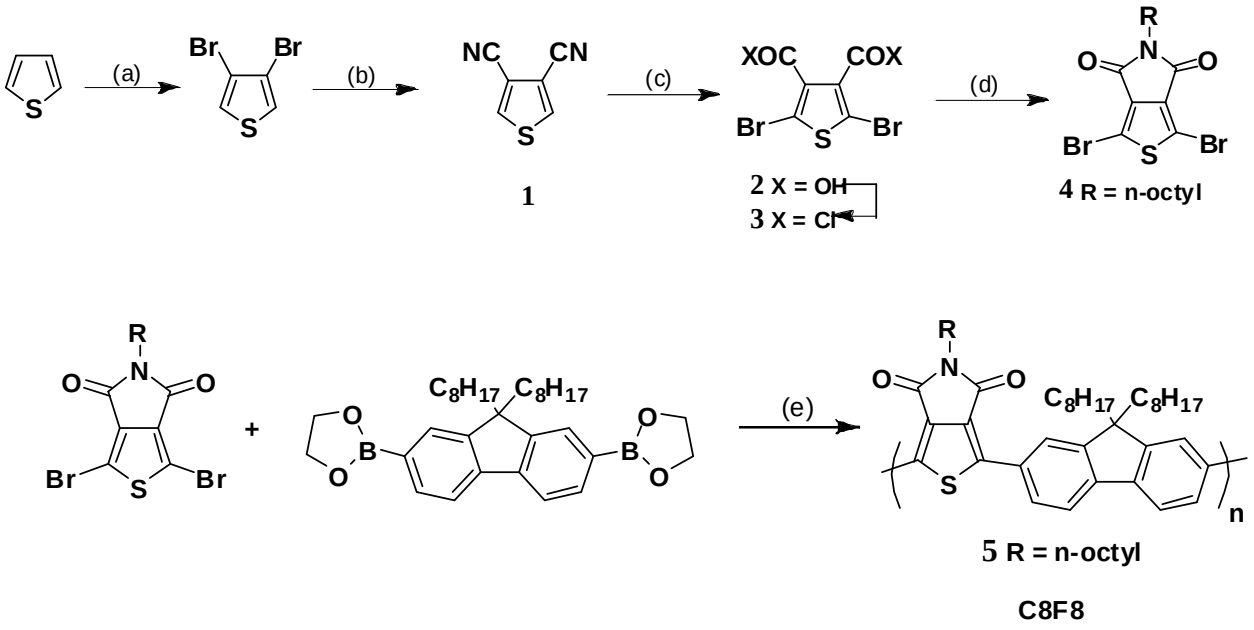

Reagents and conditions: (a) 1. $Br_2/CHCl_3$, 60 °C; 2. KOH/ethanol, reflux; 3. Zn/AcOH, reflux; (b) CuCN/DMF, reflux; (c) 1. HCl/H_2O, reflux; 2. Br_2/AcOH; (d) alkylamine, 140 °C; (e) Na_2CO_3, $Pd(Ph_3P)_4$/THF/Aliquat 336, reflux.®

Scheme 1. Synthesis of polymer C8F8.

3. Results and Discussion

3-1. Characterization of C8F8 Films. *UV-Vis Optical Absorption, Photoluminescence (PL) Emission, Cyclic Voltammetry, and Thermal Stability.*

The copolymer C8F8 (**5**) was synthesized according to the procedures in Scheme 1. The Suzuki polycondensation of the dibromide **4** with the fluorene bis(ethyleneboronate) was carried out under basic conditions with the $Pd(Ph_3P)_4$ catalyst in a system of THF and Aliquat 336 to afford poly(2,5-N-*n*-octyl-3,4-cyclicimidothienyl-*co*-2',7'-9',9'-di-*n*-octylfluorene) (**5**) in 64% yield; the molecular weight of **5** was determined by GPC analysis with polystyrene standards, M_w = 15460 (PD = 2.3). The copolymer is completely soluble in common organic solvent, such as chloroform, chlorobezene and THF. Thermogravimetric analysis (Figure 1) showed a high onset decomposition temperature (T_d): 410 °C. The high T_d suggest robust thermal stability of amorphous thin films for devices.

The normalized optical absorption and photoluminescence (PL) emission spectra of the C8F8 polymer as a dilute (10^{-5} M) chlorobenzene solution and as a thin film are shown in Figure 2. The principal photophysical properties of C8F8 are collected in Table 1. The C8F8 polymer has a strong optical absorption with a maximum (λ_{max}^{abs}) at 459 nm in dilute solution. The absorption spectra of C8F8 thin films are generally similar in shape and peak position to that in dilute solution, which suggests comparable ground-state electronic structures of this copolymer with no significant change in conformation in the condensed state. The optical band gaps (E_g^{opt}) derived from the absorption edge of the solution and thin film spectra of C8F8 are 2.56 eV and 2.44 eV,

respectively. The PL emission spectrum of C8F8 has well-resolved vibronic structure in dilute chlorobenzene solution as shown in Figure 2. It emits a cyan light with an emission maximum at 486 nm and a vibronic sideband at 512 nm. The emission spectrum of a C8F8 thin film does not

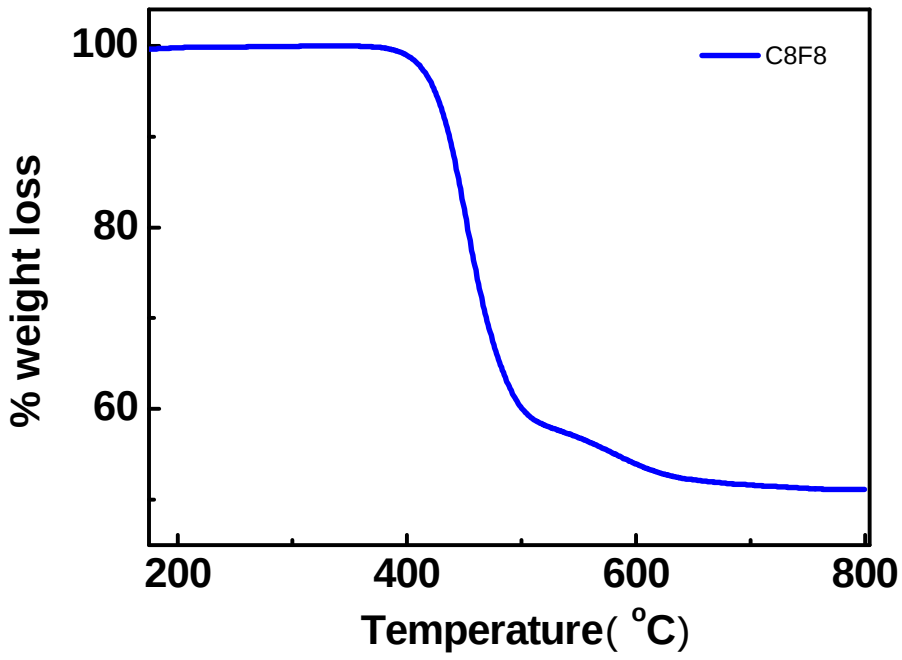

Figure 1. TGA of C8F8.

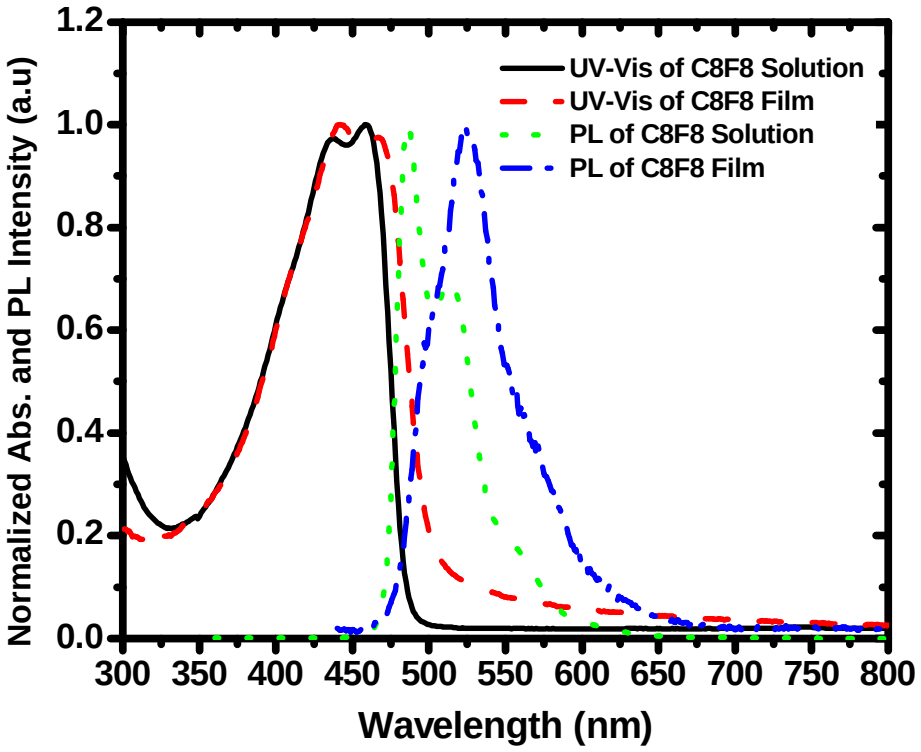

Figure 2. Absorption and PL emission spectra of C8F8 in solution and film.

Polymer	Abs.λ_{sol} (Eg)	Abs.λ_{film} (Eg)	PLλ_{sol}	PLλ_{film}	$E_{Ox,\ onset}$ /$E_{Red,\ onset}$ (v.s. SCE)	HOMO/LUMO
C8F8	459 nm (2.56 eV)	441 nm (2.44 eV)	486 nm	524 nm	1.39 V/--	5.79/3.35 eV

Table 1. Photophysical Properties of C8F8

have vibronic structure and shows an emission peak at 524 nm, suggesting a decrease of intrachain order in the copolymer. To test the thermal stability, films of C8F8 were annealed under air and ambient light, and the UV-Vis absorption and PL emission spectra were recorded (Figure 3). C8F8 maintained its color integrity even after annealing at 200 °C for 4 h.

The energy band diagrams of the polymer were determined from the band gaps, which were estimated from the absorption edges, and the HOMO energy levels, which were estimated from cyclic voltammetry. The CV was performed with a solution of 0.1 M TBAHFP in anhydrous acetonitrile and ferrocene as the internal standard at a scan rate of 100 mV/s at room temperature under the protection of nitrogen. A platium electrode coated with a thin polymer was used as the working electrode. A Pt wire and an Ag electrode were used as the counter electrode and reference eletrode, respectively. After coating, the film adhering to the electrode waas dried in a vacuum oven for 3 h. From the onset potential for the oxidation, the estimate of the ionization potential (IP, HOMO level) for the C8F8 (IP = E_{ox}^{onset} + 4.4) is ca. 5.79 eV(see Supporting Information).[10] The elcetron affinity (EA, LUMO level), calculated from the values of the band gap and HOMO energy level, is 3.35 eV.

3-2. C8F8-based PLEDs. PLEDs of varying architectures, based on the copolymer C8F8, were fabricated and evaluated in ambient air. Four different device structures were investigated: ITO/PEDOT/C8F8/CsF/Al (Device 1), ITO/PEDOT/TFB + TPD-Si_2/C8F8/CsF/Al (Device 2), ITO/PEDOT/C8F8+TFB/ CsF/Al (Device 3), ITO/PEDOT/TFB + TPD-Si_2/C8F8+TFB/CsF/Al (Device 4). The EL spectra of C8F8-based and C8F8 + TFB blend-based PLEDs are shown in Figure 5. The EL emission of C8F8-based device 1 is cyan in color and has a maximum at 488 nm and CIE coordinates of (0.16, 0.35). The PLED based on the C8F8 + TFB blend (Device 3) emits

pure green with an EL maximum at 523 nm and CIE coordinates (0.28, 0.58). This red-shift emission from C8F8 + TFB blend may be due to exciplex states at the C8F8: TFB heterojunction.

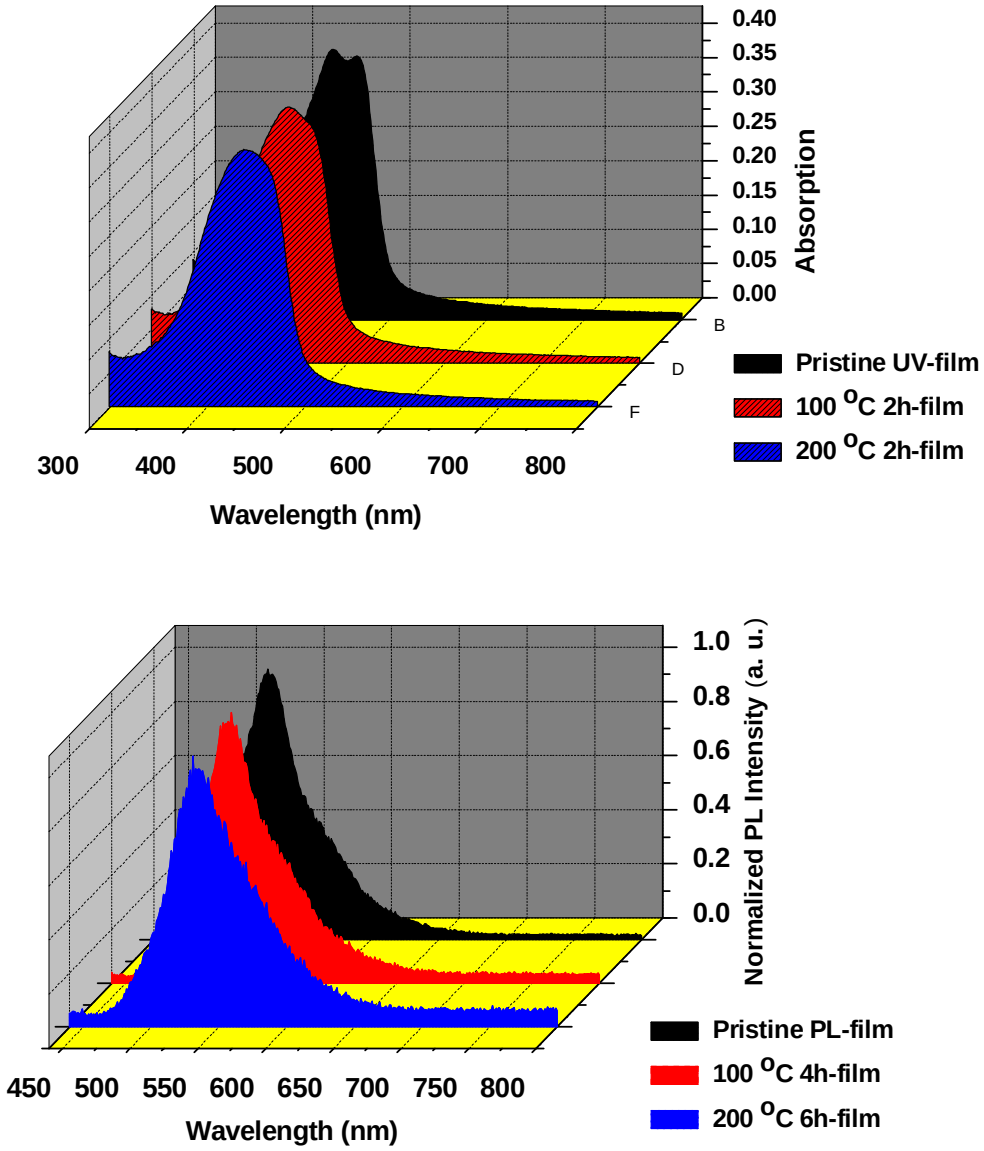

Figure 3. Effect of thermal aging on UV-Vis absorption and PL spectra of C8F8 under air.

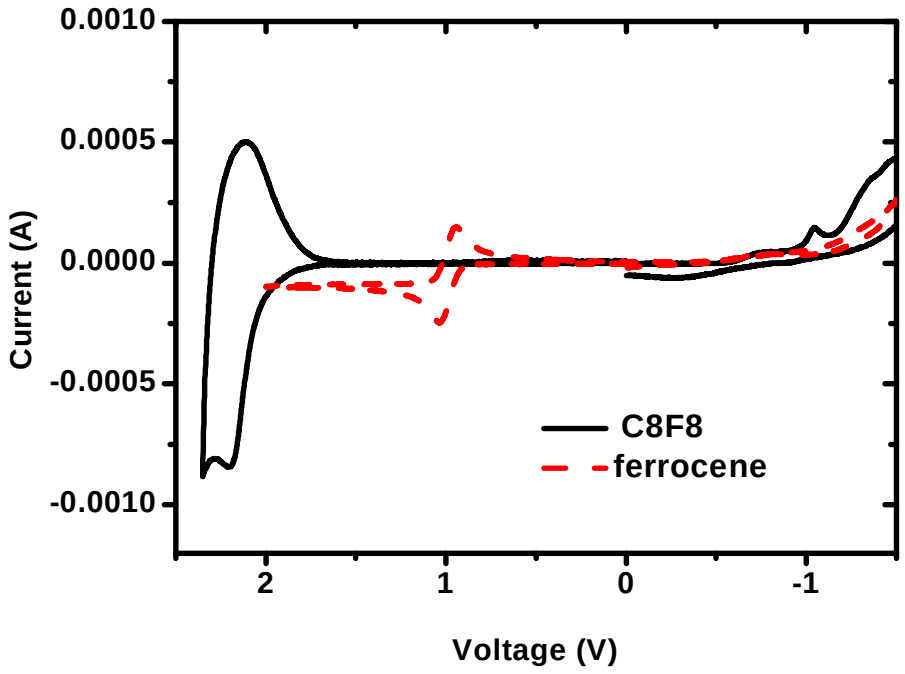

Figure 4. Cyclic Voltammogram of C8F8 film.

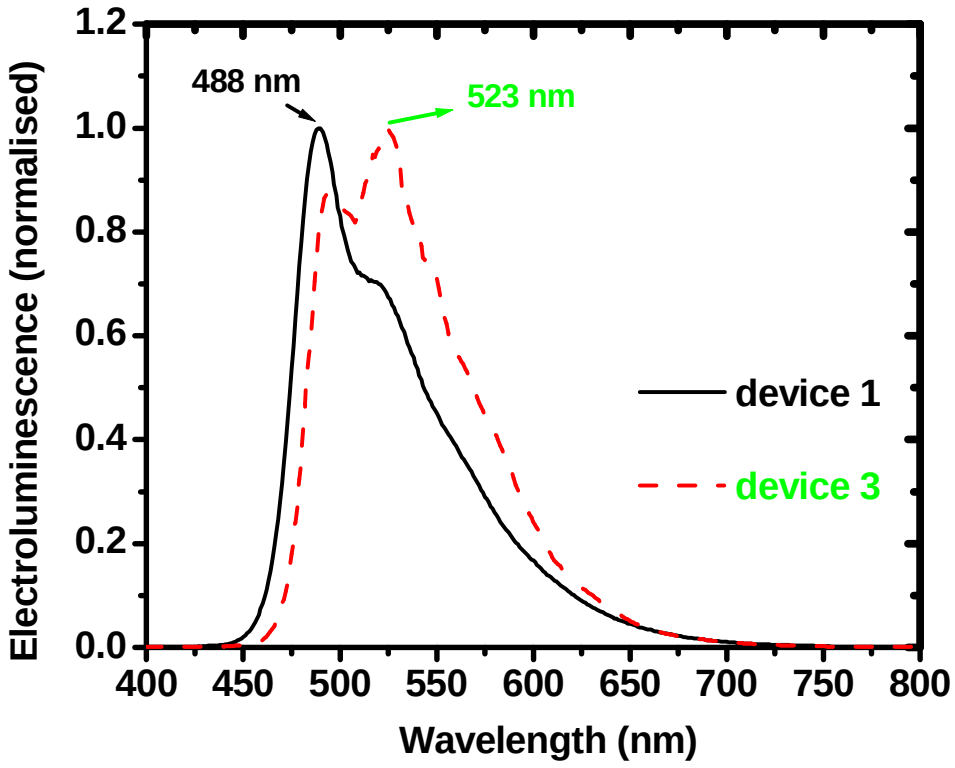

Figure 5. EL of spectra of C8F8-based PLED: ITO/PEDOT/C8F8/CsF /Al (Device 1) and C8F8 + TFB blend-based PLED: ITO/PEDOT/C8F8 + TFB/CsF/Al (Device 3).

Typical luminance - current density - current efficiency - voltage characteristics of PLEDs fabricated with C8F8 and the C8F8 + TFB blend are shown in Figure 6. The electroluminescence properties, including turn-on voltage, EL emission maximum, maximum luminance and maximum current efficiency are summarized in Table 2. The performances of C8F8 + TFB blend based devices (3 and 4) are superior to those of the C8F8-only based devices (1 and 2) in the same device configuration. This is attributed to the type-II heterojunction formed by C8F8 (IP = 5.79 eV, EA = 3.35 eV) and TFB (IP = 5.3 eV, EA = 2.3 eV). The two systems form type-II heterojunction, i.e., both the HOMO and LUMO energies are higher in one polymer than in the other, leading to an interface with charge-transfer character (Scheme 2). Type-II heterojunctions have generally been found to be useful for device optimization.[11,12] In LEDs, they cause charge to accumulate at opposite sides of the junction leading to a well-defined recombination zone whose position in the device can be controlled, as well as producing less leakage current as shown in Figure 6A.

The performance of the single-HTL devices is modest for both C8F8- (device 1) and C8F8 + TFB blend- (device 3) based diodes, yielding maximum light output of 560 cd/m^2 and 1090 cd/m^2, with maximum current efficiency of 0.11 cd/A and 0.60 cd/A, respectively. This indicates inadequate charge-carrier utilization in the single HTL diodes, with most of the electrons passing through the devices with no recombination. As expected, the performance of the C8F8- and C8F8 + TFB blend- based PLEDs is greatly improved by using an additional layer to facilitate hole injection, transport, and confinement of electrons and holes (Table 2). Devices using TFB + TPD-Si_2 as a hole-transport/electron-blocking layer (HTL/EBL)[13] exhibit a turn-on voltage of 2.4-3.0 V, at which point uniform emission over the whole pixel is visible to the eye. For C8F8-only emissive layer (EML) diodes, device 2 combines a lower turn-on voltage (2.4 V) with a higher

maximum luminance of 9140 cd/m^2 and a maximum current efficiency of 0.95 cd/A. In the case of the C8F8 + TFB blend EML, device 4 with a 3.0 V turn-on voltage, exhibits a maximum luminance of 13,200 cd/m^2 and a maximum current efficiency of 3.22 cd/A and is clearly superior to device 3.

Table 2. Device Characteristics of C8F8-based PLEDs.

	Turn-on Voltage (V)	λ_{max}^{EL} (nm)	Max. Light output (cd/m^2)	Max. Cur. Efficiency (cd/A)	Notes
Device 1	3.3	488	560	0.11	Single EML, PEDOT as HTL
Device 2	2.4	491	**9,140**	**0.95**	Single EML, Double HTL
Device 3	4.4	523	1,090	0.60	Blend EML, PEDOT as HTL
Device 4	3.0	525	**13,200**	**3.22**	Blend EML, Double HTL

Figure 6. EL response of ITO/PEDOT/C8F8/CsF/Al (Device 1), ITO/PEDOT/TFB + TPD-Si_2/C8F8/CsF/Al (Device 2), ITO/PEDOT/C8F8+TFB/CsF/Al (Device 3), ITO/PEDOT/TFB + TPD-Si_2/C8F8+TFB/CsF/Al (Device 4). (A) current density versus voltage; (B) luminance versus voltage; (C) current efficiency versus voltage.

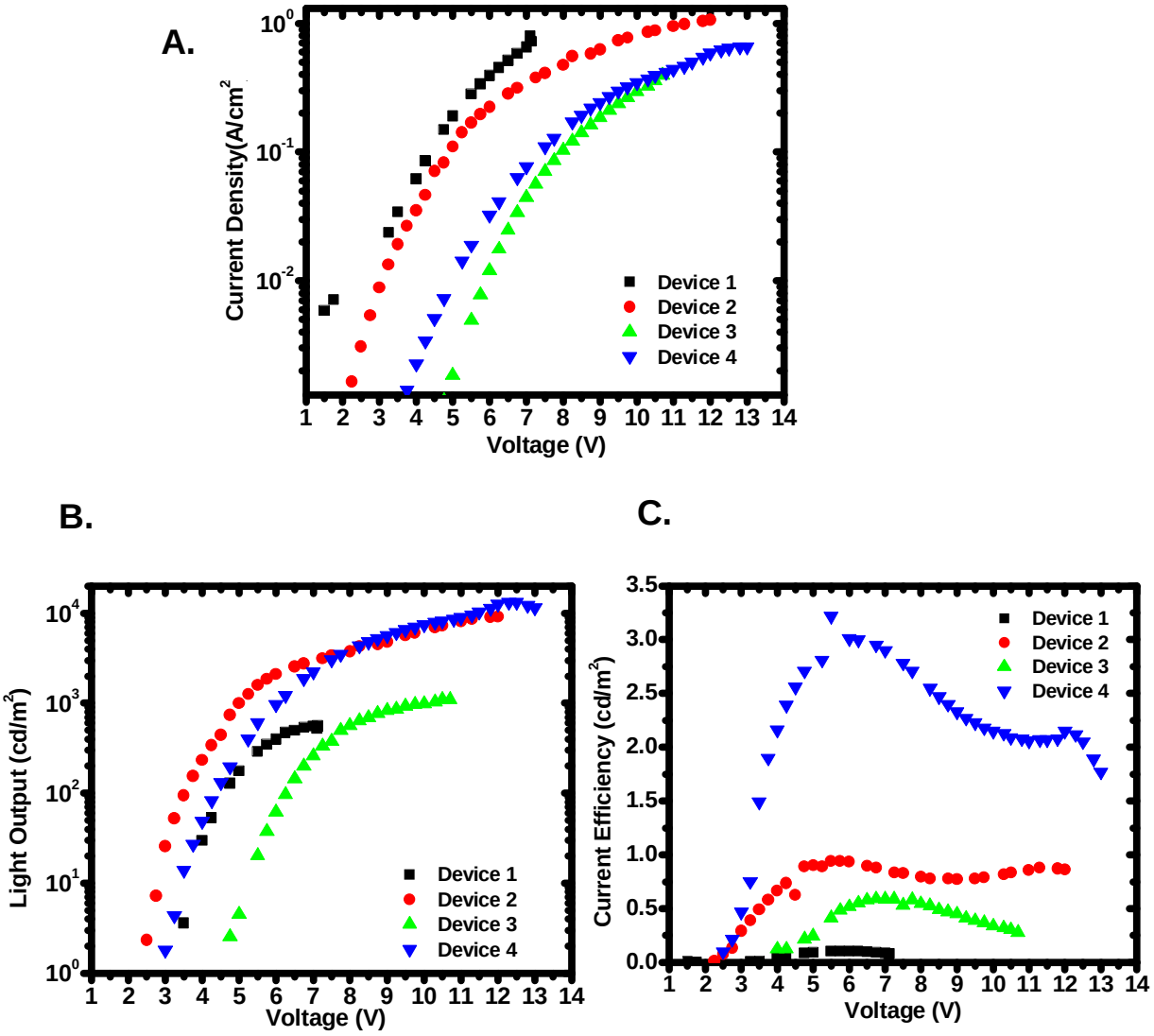

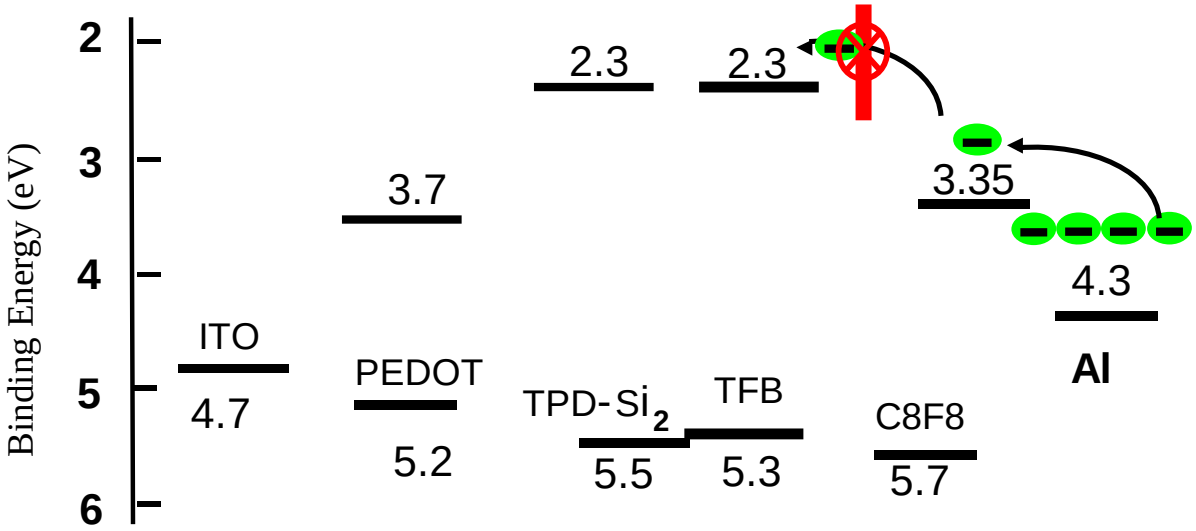

Scheme 2. Energy –level diagram for the electrodes and organic layers.

4. Conclusions

In summary, we have synthesized and characterized a novel cyan emitting copolymer poly(2,5-N-n-octyl-3,4-cyclicimidothienyl-co-2',7'-9',9'-di-n- octylfluorene) (C8F8), consisting of electron-deficient cyclicimidothiophene and fluorene moieties. The UV and photoluminescence spectra of the polymer indicate that the polymer has a band gap of 2.56 eV and cyan light emission. An organic light-emitting device incorporating this copolymer as the emitting layer exhibits a voltage-independent and stable cyan emission having color coordinates (0.16, 0.35) at 6 V; the maximum brightness is 560 cd m^{-2} and the maximum current efficiency, 0.11 cd A^{-1}. In addition, using a blend of C8F8 with the electron-rich copolymer TFB as the emitting layer in a double hole injection/transport layer (PEDOT-PSS /TFB + TPD-Si_2 device, leads to a high-brightness, highly efficient green electroluminescent device having CIE coordinate of (0.31, 0.57), a maximum brightness of 13,220 cd m^{-2}, and a maximum current efficiency of 3.22 cd A^{-1}.

References

Chapter One

1. (a) Kiriakidis, G.; Baraton, M.-J.; Mao, S. S. *Appl. Phys. A: Mater. Sci. Process* **2007,** *89,* 1. (b) Baraton, M.-J.; Mao, S. S. *Thin Solid Films* **2007**, *515*, 1. (c) Puetz, J. *Metalloberflaeche* **2007,** *61*, 38. (d) Fortunato, E.; Ginley, D.; Hosono, H.; Paine, D. C. *MRS Bull.* **2007,** *32,* 242. (d) Granqvist, C. G. *Sol. Energy Mater. Sol. Cells* **2007,** *91,* 1529. (d) Shen, S. Fang, G.; Li, C.; Xu, S.; Zhao, X. *Phys. Stat. Sol. A: Appl. Mater. Sci.* **2006,** *203,* 1891.

2. (a) Granqvist, C. G.; Hultaker, A. *Thin Solid Films* **2002**, *411*, 1. (b) Hosono, H.; Ohta, H.; Orita, M.; Ueda, K.; Hirano, M. *Vacuum* **2002,** *66*, 419. (c) Freeman, A. J.; Poeppelmeier, K. R.; Mason, T. O.; Chang, R. P. H.; Marks, T. J. *MRS Bull.* **2000,** *25*, 45. (d) Minami, T. *MRS Bull.* **2000,** *25*, 38. (e) Gordon, R. G. *MRS Bull.* **2000,** *25*, 52. (f) Lewis, B. G.; Paine, D. C. *MRS Bull.* **2000,** *25*, 22. (g) Kawazoe, H.; Yanagi, H.; Ueda, K.; Hosono, H. *MRS Bull.* **2000,** *25*, 28. (h) Coutts, T. J.; Young, D. L.; Li, X. *MRS Bull.* **2000,** *25*, 58.

3. (a) Ohta, H.; Hosono, H. *Materials. Today* **2004,** *7*, 42. (b) Granqvist, C. G. *Adv. Mater.* **2003,** *15*, 1789. (c) Kawamura, K.; Takahashi, M.; Yagihara, M.; Nakayama, T. Eur. Pat. Appl. EP 1271561, A2 20030102, CAN 138:81680, AN 2003:4983, **2003.** (d) Mason, T. O.; Gonzalez, G. B.; Kammler, D. R.; Mansourian-Hadavi, N.; Ingram, B. J. *Thin Solid Films* **2002,** *411*, 106. (e) Wu, X.; Dhere, R. G.; Albin, D. S.; Gessert, T. A.; DeHart, C.; Keane, J. C.; Duda, A.; Coutts, T. J.; Asher, S.; Levi, D. H.; Moutinho, H. R.; Yan, Y.; Moriarty, T.; Johnston, S.; Emery, K.; Sheldon, P. *Proc.-NCPV Program Rev. Meet., Lakewood, Co, USA* **2001,** 47. (f) Ginley, D. S.; Bright, C. *MRS Bull.* **2000,** *25*, 15. (g)

Coutts, T. J.; Mason, T. O.; Perkins, J. D.; Ginley, D. S. *Electrochem. Soc. Proc.* **1999,** 274.

4. Kim, J. S.; Ho, P. K. H.; Thomas, D. S.; Friend, R. H.; Cacialli, F.; Bao, G.-W.; Li, S. F. Y. *Chem. Phys. Lett.* **1999,** *315*, 307.

5. Kim, J. S.; Cacialli, F.; Granstrom, M.; Friend, R. H.; Johansson, N.; Salaneck, W. R.; Daik, R.; Feast, W. J. *Synth. Met.* **1999,** *101*, 111.

6. Kim, H.; Gilmore, C. M.; Pique, A.; Horowitz, J. S.; Mattoussi, H.; Murata, H.; Kafafi, Z. H.; Chrisey, D. B. *J. Appl. Phys.* **1999,** *86*, 6451.

7. Mason, M. G.; Hung, L. S.; Tang, C. W.; Lee, S. T.; Wong, K. W.; Wang, M. *J. Appl. Phys.* **1999,** *86*, 1688.

8. Brabec, C. J.; Sariciftci, N. S.; Hummelen, J. C. *Adv. Funct. Mater.* **2001,** *11*, 15.

9. Hatton, R. A.; Willis, M. R.; Chesters, M. A.; Rutten, F. J. M.; Briggs, D. *J. Mater. Chem.* **2003,** *13*, 38.

10. Bruner, E. L.; Koch, N.; Span, A. R.; Bernasek, S. L.; Kahn, A.; Schwartz, J. *J. Amer. Chem. Soc.* **2002,** *124*, 3192.

11. Schlatmann, A. R.; Floet, D. W.; Hillberer, A.; Garten, F.; Smulders, J. M.; Klapwijk, T. M.; Hadziioannou, G. *Appl. Phys. Lett.* **1996,** *69*, 1764.

12. (a) Milliron, F. J.; Hill, I. G.; Shen, C.; Kahn, A.; Schwartz, J. *J. Appl. Phys.* **2000,** *87*, 572. (b) Wu, C. C.; Wu, C. I.; Sturm, J. C.; Kahn, A. *Appl. Phys. Lett.* **1997,** *70*, 1348.

13. Nuesch, F.; Rothberg, L. J.; Forsythe, E. W.; Le, Q. T.; Gao, Y. *Appl. Phys. Lett*. **1999,** *74*, 880.

14. Le, Q. T.; Forsythe, E. W.; Nuesch, F.; Rothberg, L. J.; Yan, L.; Gao, Y. *Thin Solid Films* **2000,** *363*, 42.

15. Kim, J. S.; Granstrom, M.; Friend, R. H.; Johansson, N.; Salaneck, W. R.; Daik, R.; Feast, W. J.; Cacialli, F. *J. Appl. Phys*. **1998,** *84*, 6859.

16. Karg, S.; Scott, J. C.; Salem, J. R.; Angelopoulos, M. *Synth. Met*. **1996,** *80*, 111.

17. Carter, S. A.; Angelopoulos, M.; Karg, S.; Brock, P. J.; Scott, J. C. *Appl. Phys. Lett.* **1997,** *70*, 2067.

18. VanderKam, S. K.; Gawalt, E. S.; Schwartz, J.; Bocarsly, A. B. *Langmuir* **1999,** *15*, 6598.

19. (a) Span, A. R.; Bruner, E. L.; Bernasek, S. L.; Schwartz, J. *Langmuir* **2001,** *17*, 948. (b) Purvis, K. L.; Lu, G.; Schwartz, J.; Bernasek, S. L. *J. Am. Chem. Soc.* **2000,** *122*, 1808.

20. (a) Guo, J; Koch, N.; Schwartz, J.; Bernasek, S. L. *J. Phys. Chem. B* **2005,** *109*, 3966. (b) Appleyard, S. F. J.; Day, S. R.; Pickford, R. D.; Willis, M. R. *J. Mater. Chem.* **2000,** *10*, 169.

21. (a) Cui, J., Huang, Q.; Veinot, J. G. C.; Yan, H.; Wang, Q.; Hutchison, G. R.; Richter, A. G.; Evmenenko, G.; Dutta, P.; Marks, T. J. *Langmuir* **2002,** *18*, 9958. (b) Cui, J.; Wang, A.; Edelman, N. L.; Lee, P. A.; Armstrong, N. R.; Marks, T. J. *Adv. Mater.* **2001,** *13*, 1476. (c) Malinsky, J. E.; Jabbour, G. E.; Shaheen, S. E.; Anderson, J. D.; Richter, A. G.; Armstrong, N. R.; Kipplelen, B.; Dutta, P.; Peyghambarian, N.; Marks, T. J. *Adv. Mater.*

1999, *11*, 227. (d) Li, W.; Wang, Q.; Cui, J.; Chou, H.; Shaheen, S. W.; Jabbour, G. E.; Anderson, J. D.; Le, P. A.; Kippelen, B.; Peyghambarian, N.; Armstrong, N. R.; Marks, T. J. *Adv. Mater.* **1999,** *11*, 730.

22. (a) Huang, Q.; Li, J.; Evmenenko, G. A.; Dutta, P., and Marks, T. J., *J. Appl. Phys.,* **2007,** 101, 093101/01. (b) Huang, Q.; Li, J.; Evmenenko, G. A.; Dutta, P., and Marks, T. J., *Chem. Mater*. **2006,** 18, 2431. (c) Veinot, J. G. C.; Marks, T. J. *Acc. Chem. Res*., **2005,** *38*, 632. (d) Huang, Q.; Evmenenko, G. A.; Dutta, P.; Lee, P.; Armstrong, N. R.; Marks, T.J. *J. Am. Chem. Soc.* **2005,** *127*, 10227. (e) Huang, Q.; Evmenenko, G.; Dutta, P.; Marks, T. J. M *J. Am. Chem. Soc.* **2003,** *125*, 14704.

23. Dunphy, D. R.; Mendes, S. B.; Saavedra, S. S.; Armstrong, N. R. *Anal. Chem.* **1997,** *69*, 3086.

24. Bradshaw, J. T.; Mendes, S. B.; Armstrong, N. R.; Saavedra, S. S. *Anal. Chem.* **2003,** *75*, 1080.

25. Jansseune, T. *Compd. Semiconductor Mag.* 2003, Sept.

26. Philips, J. M.; Kwo, J.; Thomas, G. A.; Carter, S. A.; Cava, R. J.; Hou, S. Y.; Krajewski, J. J.; Marshall, J. H.; Peck, W. F.; Rapkine, D. H.; Dover, R. B. V. *Appl. Phys. Lett.* **1994,** *65*, 115.

27. Schlatmann, A. R.; Floet, D. W.; Hillberer, A.; Garten, F.; Smulders, P. J. M.; Klapwijk, T. M.; Hadziioannou, G. *Appl. Phys. Lett*. **1996,** *69*, 1764.

28. Scott, J. C.; Kaufman, J. H.; Brock, P. J.; Dipietro, R.; Salem, J.; Goitia, J. A. *J. Appyl. Phys.* **1996,** *79*, 2745.

29. Marks, T. J.; Veinot, J. G. C.; Cui, J.; Yan, H.; Wang, A.; Edelman, N. L.; Ni, J.; Huang, Q.; Lee, P. A.; Armstrong, N. R. *Synth. Met*. **2002,** *127*, 29.

30. (a) Metz, A. W.; Ireland, J. R.; Zheng, J. G.; Lobo, R. P. S. M.; Yang, Y.; Ni, J.; Stern, C. L.; Dravid, V. P.; Bontemps, N.; Kannewurf, C. R.; Poeppelmeier, K. R.; Marks, T. J. *J. Am. Chem. Soc.* **2004,** *126*, 8477. (b) Asahi, R.; Wang, A.; Babcock, J. R.; Edleman, N. L.; Metz, A. W.; Lane, M. A.; Dravid, V. P.; Kannewurf, C. R.; Freeman, A. J.; Marks, T. J. *Thin Solid Films* **2002,** *411*, 101. (c) Wang, A.; Babcock, J. R.; Edleman, N. L.; Metz, A. W.; Lane, M. A.; Asahi, R.; Dravid, V. P.; Kannewurf, C. R.; Freeman, A. J.; Marks, T. J. *Proc. Natl. Acad. Sci. U.S.A.* **2001,** *98*, 7113.

31. Yang, Y.; Huang, Q.; Metz, A. W.; Jin, S.; Ni, J.; Wang, L.; Marks, T. J. *J. Soc. for Information Display*, **2005**, *13*, 383.

32. Ni, J.; Yan, H.; Wang, A.; Yang, Y.; Stern, C. L.; Metz, A. W.; Jin, S.; Wang, L.; Marks, T. J.; Ireland, J. R.; Kannewurf. C. R. *J. Am. Chem. Soc.* **2005,** *127*, 5613.

33. Yang, Y.; Huang, Q.; Metz, A. W.; Ni, J.; Jin, S.; Marks, T. J.; Madsen, M. E.; DiVenere, A.; Ho, S.-T. *Adv. Mater.*, **2004,** 16, 321.

34. Wang, L.; Yang, Y.; Marks, T. J.; Liu, Z.; Ho, S.-T. *Appl. Phys. Lett*. **2005,** *87*, 161107/1.

35. Donley, C. L.; Dunphy, D. R.; Peterson, R. A.; Nebesny, K. W.; Armstrong, N. R. In *Conjugated Polymer and Molecular Interfaces: Science and Technology for Photonic and*

Optoelectronic Applications; Salaneck, W. R., Seki, K., Kahn, A., Pireauz, J. J., Eds.; Marcel Dekker: New York, 2001; pp 269-292.

36. Baes, C. F., Jr.; Mesmer, R. E. In *The Hydrolysis of Cations*; John Wiley & Sons: New York, 1976; pp 319-327, 349-357.

37. (a) Brumbach, M.; Veneman, P. A.; Marrikar, F. S.; Schulmeyer, T.; Simmonds, A.; Xia, W.; Lee, P.; Armstrong, N. R. *Langmuir* **2007,** *23*, 11089. (b) Carter, C.; Brunmbach, M.; Donley, C.; Hreha, R. D.; Marder, S. R.; Domercq, B.; Yoo, S.; Kippelen, B.; Armstrong, N. R. *J. Phys. Chem B* **2006,** *110*, 25191. (c) Armstrong, N. R.; Carter, C.; Donley, C.; Simmonds, A.; Lee, P.; Brumbach, M.; Kippelen, B.; Domercq, B.; Yoo, S., *Thin Solid Films* **2003,** *445*, 342. (d) Donley, C.; Dunphy, D.; Paine, D.; Carter, C.; Nebesny, K.; Lee, P.; Alloway, D.; Armstrong, N. R. *Langmuir* **2002,** *18*, 450.

38. Appleyard, S. F. J.; Day, S. R.; Pickford, R. D.; Willis, M. R. *J. Mater. Chem.* **2000,** *10*, 169.

39. Zuppiroli, L.; Si-Ahmed, L.; Kamars, K.; Nüesch, F.; Bussac, M. N.; Ades, D.; Siove, A.; Moons, E.; Grätzel, M. *Eur. Phys. J. B* **1999**, *11*, 505.

40. Forsythe, E.; Gao, Y. In *Handbook of Surfaces and Interfaces of Materials*; Nalwa, H. S., Ed.; Academic Press: London, 2001; Vol. 1, pp 285-327.

41. Goncalves-Conto, S.; Carrard, M.; Si-Ahmed, L.; Zuppiroli, L. *Adv. Mater.* **1999,** *11*, 112.

42. Ishii, H.; Sugiyama, K.; Ito, E.; Seki, K. *Adv. Mater.* **1999,** *11*, 605.

43. Vuillaume, D.; Lenfant, S. *Microelectron. Eng.* **2003,** *70*, 539.

44. Ahles, M.; Schmechel, R.; von Seggern, H. *Appl. Phys. Lett.* **2004,** *85*, 4499.

45. Nuzzo, R. G.; Allara, D. L. *J. Am. Chem. Soc.* **1983,** *105*, 4481.

46. Ulman, A. *An Introduction to Ultrathin Organic Films: From Langmuir-Blodgett to Self-Assembly*; Academic Press: New York, 1991.

47. (a) Finklea, H. O.; Snider, D. A.; Fedyk, J.; Sabatani, E.; Gafni, Y.; Rubinstein, I. *Langmuir* **1993,** *9*, 3660. (b) Laibinis, P. E.; Whitesides, G. M. *J. Am. Chem. Soc.* **1992,** *114*, 1990. (c) Bain, C. D.; Biebuyck, H. A.; Whitesides, G. M. *Langmuir* **1989,** *5*, 723.

48. (a) Bent, S. F. *ACS Nano* **2007,** *1*, 10. (b) Huck, W. T. S. *Angew. Chem., Inter. Ed.* **2007,** *46*, 2754. (c) Tao, F.; Bernasek, S. L. *Chem. Rev.* **2007,** *107*, 1408.

49. Vericat, C.; Vela, M. E.; Benitez, G. A.; Gago, J. A. Martin; Torrelles, X.; Salvarezza, R. C. *J. Phys.: Condensed Matter* **2006,** *18*, R867.

50. Chidsey, C. E. D.; Bertozzi, C. R.; Putvinski, T. M.; Mujsce, A. M. *J. Am. Chem. Soc.* **1990,** *112*, 4301.

51. De Long, H. C.; Buttry, D. A. *Langmuir* **1990,** *6*, 1319.

52. Murray, R. W., Ed. *Molecular Design of Electrode Surfaces*; John Wiley and Sons: New York, 1992.

53. Finklea, H. O. In *Electroanalytical Chemistry*; Bard, A. J., Rubinstein, I., Eds.; Marcel Dekker: New York, 1996; Vol. 19, p 109.

54. Boozer, C.; Ladd, J.; Chen, S.; Yu, Q.; Homola, J.; Jiang, S. *Anal. Chem.* **2004,** *76*, 6967.

55. Campuzano, S.; Pedrero, M.; Pingarron, J. M. *Talanta* **2005,** *66*, 1310.

56. Zamborini, F. P.; Campbell, J. K.; Crooks, R. M. *Langmuir* **1998,** *14*, 640.

57. Jennings, G. K.; Laibinis, P. E. *J. Am. Chem. Soc.* **1997,** *119*, 5208.

58. Kitagawa, K.; Morita, T.; Kimura, S. *Langmuir* **2005,** *21*, 10624.

59. Chen, J.; Reed, M. A.; Rawlett, A. M.; Tour, J. M. *Science* **1999,** *286*, 1550.

60. Andres, R. P.; Bein, T.; Dorogi, M.; Feng, S.; Henderson, J. I.; Kubiak, C. P.; Mahoney, W.; Osifchin, R. G.; Reifenberger, R. *Science* **1996,** *272*, 1323.

61. (a) Bain, C. D.; Troughton, E. B.; Tao, Y.-T.; Evall, J.; Whitesides, G. M.; Nuzzo, R. G. *J. Am. Chem. Soc.* **1989,** *111*, 321. (b) Sagiv, J. *J. Am. Chem. Soc.* **1980,** *102*, 92.

62. (a) Chidsey, C. E. D. *Science* **1991,** *261*, 919. (b) Pinkerton, M. J.; LeMest, Y.; Zhang, H.; Watanabe, M.; Murray, R. W. *J. Am. Chem. Soc.***1990,** *112*, 3730. (c) Wipf, D. O.; Kriatensen, M. D.; Wightman, R. M. *Anal. Chem.* **1988,** *60*, 306. (d) Aoki, K.; Morita, M.; Niwa, O.; Tabei, H. *J. Electroanal. Chem.* **1988,** *266*, 269.

63. Wilson, R.; Schiffrin, D. J. *Analyst* **1995,** *120*, 175.

64. Jong, S.-J.; Fang, J.-M., *J. Org. Chem.*, **2001,** *66*, 3533.

65. Ulman, A. *Chem. Rev.* **1996**, *96*, 1533.

66. Richter, A. G.; Yu, C. J.; Datta, A.; Kmetko, J.; Dutta, P. *Phys. Rev. E* **2000,** *61*, 607.

67. Heiney, P. A.; Grüneberg, K.; Fang, J.; Dulcey, C.; Shashidhar, S. *Langmuir* **2000,** *16*, 2651.

68. Evmenenko, G.; van der Boom, M. E.; Yu, C.-J.; Kmetko, J.; Dutta, P. *Polymer* **2003,** *44*, 1051.

69. Als-Nielsen, J. *Physica* **1986,** *140A*, 376.

70. Evmenenko, G.; Yu, C.-J.; Kmetko, J.; Dutta, P. *Langmuir* **2002,** *18*, 5468.

71. Zotti, G.; Schiavon, G.; Zecchin, S.; Berlin, A.; Pagani, G. *Langmuir* **1998,** *14*, 1728.

72. Hains, A. W.; Martinson, A. B. F.; Irwin, M. D.; Yan, H.; Marks, T. J. unpublished results.

73. Seah, M. P. In *Practical Surface Analysis by Auger and X-ray Photoelectron Spectroscopy*, Briggs, D.; Seah, M. P., Eds.; John Wiley and Sons: Chichester, UK, 1983; Vol. 14, p 181.

74. Chidsey, C. E. D.; Bertozzi, C. R.; Putvinski, T. M.; Mujsce, A. M. *J. Am. Chem. Soc.* **1990,** *112*, 4301.

75. Weber, K.; Creager, S. E. *Anal. Chem.* **1994,** *66*, 3164.

76. Laviron, E. *J. Electroanal. Chem.*, **1979,** *101*, 19.

77. Bard, A. J.; Faulkner, L. A. *Electrochemical Methods-Fundamentals and Applications*; Wiley: New York, 1984; pp 580-631.

78. Clark, R. A.; Bowden, E. F. *Langmuir* **1997,** *13*, 559.

79. Zhang, W. W.; Ren, X. M.; Li, H. F.; Lu, C. S.; Hu, C. J.; Zhu, H. Z.; Meng, Q. J. *J. Colloid Interface Sci.* **2002,** *255*, 150.

80. Nielsen, M.; Larsen, N. B.; Gothelf, K. V. *Langmuir* **2002,** *18*, 2795.

81. Liau, Y. H.; Scherer, N. F.; Rhodes, K. *J. Phys. Chem. B* **2001,** *105*, 3282.

82. Liu, H. Y.; Yamamoto, H.; Wei, J. J.; Waldeck, D. H. *Langmuir* **2003,** *19*, 2378.

83. Finklea, H. O.; Liu, L.; Ravenscroft, M. S.; Punturi, S. *J. Phys. Chem.* **1996,** *100*, 18852.

84. Finklea, H. O.; Hanshew, D. D. *J. Am. Chem. Soc.* **1992,** *114*, 3173.

85. Newton, M. D.; Sutin, N. *Annu. Rev. Phys. Chem.* **1984,** *35*, 437.

86. Nahir, T. M.; Clark, R. A.; Bowden, E. F. *Anal. Chem.* **1994,** *66*, 2595-2598.

87. Newton, M. D. *Chem. Rev.* **1991,** *91*, 767-792.

88. Napper, A. M.; Liu, H. Y.; Waldeck, D. H. *J. Phys. Chem. B* **2001,** *105*, 7699.

89. Clark, R. A.; Bowden, E. F. *Langmuir* **1997,** *13*, 559.

90. Marcus, R. A. *J. Phys. Chem.* **1963,** *67*, 853.

91. Marcus, R. A. *Angew. Chem., Int. Ed.* **1993,** *32*, 1111.

92. Geer, R. E.; stinger, D. A.; Chen, M. S.; Calvert, J. M.; Shashidhar, R. *Langmuir* **1994,** *10*, 1171.

93. Monk, P. *Fundamentasl of Electroanalytical Chemistry;* John Wiley and Sons: Chichester, UK, 2001; pp 156-169.

94. Memming, R. In *Electroanalytical Chemistry: A Series of Advances*; Bard, A. J., Eds; Marcel Dekker: NewYork, 1979; pp 1-81.

95. Fujihira, M.; Rusling, J. F.; Rubinstein, I. In *Encyclopedia of Electrochemistry;* Bard, A. J.; Stratmann, M., Eds; Weinheim: Wiley-VCH, 2006; Vol.10, pp 1-57.

Chapter TWO

1. Martin, G. In *Handbook of Optoelectronics*; Dakin, J. P.; Brown, R. G. W., Ed.; CRC Press LLC, Boca Raton, Fla., 2006; Vol. II, 1, pp 693-718.

2. Veinot, J. G. C.; Marks, T. J. *Acct. Chem. Res.*, **2005**, *38*, 632.

3. Chen, C.-T. *Chem. Mater.* **2004,** *16*, 4389-4400.

4. Shim, H.-K.; Jin, J.-I. *Adv. Polym. Sci.* **2002,** *158*, 193-243.

5. Nalwa, H. S. In *Handbook of Advanced Electronic and Photonic Materials and Devices*; Nalwa, H. S., Ed.; Academic: San Diego, CA, 2001; Vol. 10, pp 1-51.

6. Mitschke, U.; Baürle, P. *J. Mater. Chem.* **2000,** *10*, 1471-1507.

7. Scherf, U.; List, E. J. W. *Adv. Mater.* **2002,** *14*, 477-489.

8. Huang, Q.; Li, J.; Evmenenko, G. A.; Dutta, P., and Marks, T. J., *J. Appl. Phys.*, **2007,** 101, 093101/01.

9. Huang, Q.; Li, J.; Evmenenko, G. A.; Dutta, P., and Marks, T. J., *Chem. Mater.* **2006,** 18, 2431.

10. Huang, Q.; Evmenenko, G. A.; Dutta, P.; Lee, P.; Armstrong, N. R.; Marks, T.J. *J. Am. Chem. Soc.* **2005,** *127*, 10227.

11. Huang, Q.; Evmenenko, G.; Dutta, P.; Marks, T. J. M *J. Am. Chem. Soc.* **2003,** *125*, 14704.

12. Huang, Q. L.; Cui, J.; Veinot, J. G. C.; Yan, H.; Marks, T. J. *Appl. Phys. Lett.* **2003,** *82*, 331-333.

13. Niu, Y. H.; Hou, Q.; Cao, Y. *Appl. Phys. Lett.* **2003,** *82*, 2163-2165.

14. Duan, J. P.; Sun, P. P.; Cheng, C. H. *Adv. Mater.* **2003,** *15*, 224-227.

15. Mller, C. D.; Falcou, A.; Reckefuss, N.; Rojahn, M.; Wiederhirn, V.; Rudati, P.; Frohne, H.; Nuyken, O.; Becker, H.; Meerholz, K. *Nature* **2003,** *421*, 829-833.

16. Niu, Y. H.; Yang, W.; Cao, Y. *Appl. Phys. Lett.* **2002,** *81*, 2884-2886.

17. Herguch, P.; Jiang, X. Z.; Liu, M. S.; Jen, A. K. Y. *Macromolecules* **2002,** *35*, 6094-6100.

18. Ishii, H.; Sugiyama, K.; Ito, E.; Seki, K. *Adv. Mater.* **1999,** *11*, 605-625.

19. Tang, C. W.; VanSlyke, S. A. *Appl. Phys. Lett.* **1987,** *51*, 913-915.

20. Brown, A. R.; Bradley, D. D. C.; Burroughes, J. H.; Friend, R. H.; Greenham, N. C.; Burn, P. L.; Holmes, A. B.; Kraft, A. *Appl. Phys. Lett.* **1992,** *61*, 2793-2795.

21. Shen, Y.; Jacobs, D. B.; Malliaras, G. G.; Koley, G.; Spencer, M. G.; Ioannidis, A. *Adv. Mater.* **2001,** *13*, 1234-1238.

22. Forsythe, E. W.; Abkowitz, M. A.; Gao, Y. *J. Phys. Chem. B* **2000,** *104*, 3948-3952.

23. Nesch, F.; Forsythe, E. W.; Le, Q. T.; Gao, Y.; Rothberg, L. J. *J. Appl. Phys.* **2000,** *87*, 7973-7980.

24. Appleyard, S. F. J.; Day, S. R.; Pickford, R. D.; Willis, M. R. *J. Mater. Chem.* **2000,** *10*, 169-173.

25. Malinsky, J. E.; Jabbour, G. E.; Shaheen, S. E.; Anderson, J. D.; Richter, A. G.; Marks, T. J.; Armstrong, N. R.; Kippelen, B.; Dutta, P.; Peyghambarian, N. *Adv. Mater.* **1999,** *11*, 227-231.

26. Hatton, R. A.; Willis, M. R.; Chesters, M. A.; Briggs, D. *J. Mater. Chem.* **2003,** *13*, 722.

27. Lee, J.; Jung, B.-J.; Lee, J.-I.; Chu, H. Y.; Do, L.-M.; Shim, H.-K. *J. Mater. Chem.* **2002,** *12*, 3494.

28. Gross, M.; Muller, D.; Nothofer, H.; Scherf, U.; Neher, D.; Brauchle, C.; Meerholz, K. *Nature* **2000,** *405*, 661-665.

29. Yang, Y.; Heeger, A. H. *Appl. Phy. Lett.* **1994,** *64*, 1245-1247.

30. Carter, S. A.; Angelopoulos, M.; Karg, S.; Brock, P. J.; Scott, J. C. *Appl. Phys. Lett.* **1997,** *70*, 2067-2069.

31. Brown, T. M.; Kim, J. S.; Friend, R. H.; Cacialli, F.; Daik, R.; Feast, W. J. *Appl. Phys. Lett.* **1999,** *75*, 1679-1681.

32. Groenendaal, B. L.; Jonas, F.; Freitag, D.; Pielartzik, H.; Reynolds, J. R. *Adv. Mater.* **2000,** *12*, 481-494.

33. Cao, Y.; Yu, G.; Zhang, C.; Menon, R.; Heeger, A. J. *Synth. Met.* **1997,** *87*, 171-174.

34. Tadayyon, S. M.; Grandin, H. M.; Griffiths, K.; Norton, P. R.; Aziz, H.; Popovic, Z. D. *Org. Electron.* **2004,** *5*, 157-166.

35. Mori, T.; Mitsuoka, T.; Ishii, M.; Fujikawa, H.; Taga, Y. *Appl. Phys. Lett.* **2002,** *80*, 3895-3897.

36. Appleyard, S. F. J.; Day, S. R.; Pickford, R. D.; Willis, M. R. *J. Mater. Chem.* **2000,** *10*, 169-174.

37. Guo, J; Koch, N.; Schwartz, J.; Bernasek, S. L. *J. Phys. Chem. B* **2005,** *109*, 3966-3970.

38. Berlin, A.; Zotti, G.; Schiavon, G.; Zecchin, S. *J. Am. Chem. Soc.* **1998,** *120*, 13453-13460.

39. Shen, Y.; Jacobs, D. B.; Malliaras, G. G.; Koley, G.; Spencer, M. G.; Ioannidis, A. *Adv. Mater.* **2001,** *13*, 1234-1238.

40. Ganzorig, C.; Kwak, K. J.; Yagi, K.; Fujihira, M. *Appl. Phys. Lett.* **2001,** *79*, 272-274.

41. Bruening, M.; Moons, E.; Yaron-Marcovich, D.; Cahen, D.; Libman, J.; Shanzer, A. *J. Am. Chem. Soc.* **1994,** *116*, 2972.

42. Malinsky, J. E.; Jabbour, G. E.; Shaheen, S. E.; Anderson, J. D.; Richter, A. G.; Marks, T. J.; Armstrong, N. R.; Kippelen, B.; Dutta, P.; Peyghambarian, N. *Adv. Mater.* **1999,** *11*, 227-231.

43. Cui, J.; Huang, Q.; Wang, Q.; Marks, T. J. *Langmuir* **2001,** *17*, 2051-2054.

44. Cui, J.; Huang, Q.; Veinot, J. C. G.; Yan, H.; Wang, Q.; Hutchison, G. R.; Richter, A. G.; Evmenenko, G.; Dutta, P.; Marks, T. J. *Langmuir* **2002,** *18*, 9958-9970.

45. Milliron, D. J.; Hill, I. G.; Shen, C.; Kahn, A.; Schwartz, J. *J. Appl. Phys.* **2000,** *87*, 572-576.

46. Li, W.; Wang, Q.; Cui, J.; Chou, H.; Marks, T. J.; Jabbour, G. E.; Shaheen, S. E.; Kippelen, B.; Pegyhambarian, N.; Dutta, P.; Richter, A. J.; Anderson, J.; Lee, P.; Armstrong, N. *Adv. Mater.* **1999,** *11*, 730.

47. Cui, J.; Huang, Q.; Veinot, J. G. C.; Yan, H.; Marks, T. *Adv. Mater.* **2002,** *14*, 565-569.

48. Huang, Q. L.; Cui, J.; Yan, H.; Veinot, J. G. C.; Marks, T. J. *Appl. Phys. Lett.* **2002,** *81*, 3528-3530.

49. Yan, H.; Huang, Q. L.; Cui, J.; Veinot, J. G. C.; Kern, M. M.; Marks, T. J. *Adv. Mater.* **2003,** *15*, 835-839.

50. Yan, H.; Huang, Q.; Scott, B. J.; Marks, T. J. *Appl. Phys. Lett.* **2004,** *84*, 3873-3875.

51. Yan, H.; Lee, P.; Armstrong, N. R.; Graham, A.; Evmenenko, G. A.; Dutta, P.; Marks, T. J. *J. Am. Chem. Soc.* **2005,** *127*, 3172.

52. Koene, B. E.; Loy, D. E.; Thompson, M. E. *Chem. Mater.* **1998,** *10*, 2235-2250.

53. Ulman, A. *Chem. Rev.* **1996,** *96*, 1533-1554.

54. Jeon, N. L.; Nuzzo, R. G.; Xia, Y.; Mrksich, M.; Whitesides, G. M. *Langmuir* **1995,** *11*, 3024-3026.

55. Ulman, A. *Thin Solid Films* **1996,** *273*, 48-53.

56. (a) Gelest Inc. Catalog, *Silane Coupling Agents: Connecting Across Boundaries;* 2001, pp 1-20. (b) Plueddemann E., In *Silane Coupling Agents*; 2nd ed., Plenum Press, New York, 1991. (c) Witucki, G. L. *J. Coatings Technology* **1993,** *65*, 57-60.

57. (a) Crist, B. V. In *Handbooks of Monochromatic XPS Spectra*; Crist, B. V., Ed.; XPS International LLC: Mountain View, CA, 2004; Vol. 1-5. (b) Grant, J. T.; Briggs, D. In *Surface Analysis by Auger and X-ray Photoelectron Spectroscopy*; Grant, J. T.; Briggs, D., Ed; IM Publications: Chichester, UK, 2003.

58. Murray, R. W. In *Molecular Design of Electrode Surfaces, Techniques of Chemistry*; Murray, R. W., Ed.; Wiley: New York, 1992; Vol. 22, pp 1-158.

59. Donley, C.; Dunphy, D.; Paine, D.; Carter, C.; Nebesny, K.; Lee, P.; Alloway, D.; Armstrong, N. R. *Langmuir* **2002,** *18*, 450-457.

60. DuBois, C. J., Jr.; McCarley, R. L. *J. Electroanal. Chem.* **1998,** *454*, 99-105.

61. Immoos, C. E.; Chou, J.; Bayachou, M.; Blair, E.; Greaves, J.; Farmer, P. J. *J. Am. Chem. Soc.* **2004,** *126*, 4934-4942.

62. Nowall, W. B.; Kuhr, W. G. *Anal. Chem.* **1995,** *67*, 3583-3588.

63. Inzelt, G. In *Electroanalytical Chemistry*; Bard, A. J., Rubenstein, I., Eds.; Marcel Dekker: New York, 1994; Vol. 18, pp 90-134.

64. Napper, A. M.; Liu, H. Y.; Waldeck, D. H. *J. Phys. Chem. B* **2001,** *105*, 7699-7707.

65. Nahir, T. M.; Clark, R. A.; Bowden, E. F. *Anal. Chem.* **1994,** *66*, 2595-2598.

66. Forster, R. J. *Inorg. Chem.* **1996,** *35*, 3394-3403.

67. Richardson, J. N.; Rowe, G. K.; Carter, M. T.; Tender, L. M.; Curtin, L. S.; Peck, S. R.; Murray, R. W. *Electrochim. Acta* **1995,** *40*, 1331-1338.

68. Cahen, D.; Hodes, G. *Adv. Mater.* **2002,** *14*, 789-798.

69. Yan H.; Scott, B. J.; Huang, Q.; Marks, T. J. *Adv. Mater.* **2004,** *16*, 1948-1953.

Chapter Three

1. Tans, S. J.; Verschueren, A. R. M.; Cees, D. *Nature* **1998**, *393*, 49.

2. Stadermann, M.; Papadakis, S. J.; Falvo, M. R.; Novak, J.; Snow, E.; Fu, Q.; Liu, J.; Fridan, Y.; Boland, J. J.; Superfine, R.; Washburn, S. *Phys. Rev. B.* **2004**, *69*, 201402/1.

3. Durkop, T.; Getty, S. A.; Cobas, E.; Fuhrer, M. S. *Nano. Lett.* **2004,** *4*, 35.

4. Perebeinos, V.; Tersoff, J.; Avouris, P. *Phys. Rev. Lett.* **2005,** *94*, 027402/1.

5. Stahl, H.; Appenzeller, J.; Martel, R.; Avouris, P.; Lengeler, B. *Phys. Rev. Lett.* **2000**, *85*, 5186.

6. Zhou, C.; Kong, J.; Dai, H. *Phys. Rev. Lett.* **2000,** *84*, 5604.

7. Moore, V. C.; Strano, M. S.; Haroz, E. H.; Hauge, R. H.; Smalley, R. E.; Schmidt, J.; Talmon, Y. *Nano. Lett.* **2003,** *3*, 1379.

8. Bekyarova, E.; Itkis, M. E.; Cabrera, N.; Zhao, B.; Yu, A.; Gao, J.; Haddon, R. C. *J. Am. Chem. Soc.* **2005,** *127*, 5990.

9. Kaempgen, M.; Duesberg, G. S.; Roth, S. *Appl. Surf. Sci.* **2005,** *252*, 425.

10. Wu, Z.; Chen, Z.; Du, X.; Logan, J. M.; Sippel, J.;Nikolou, M.; Kamaras, K.; Reynolds, J. R.; Tanner, D. B.; Hebard, A. F.; Rinzler A. G. *Science*, **2004,** *305*, 1273.

11. Hu, L.; Hecht, D.S.; Grüner, G. *Nano Lett.* **2004,** *4*, 2513.

12. Saran, N.; Parikh, K.; Suh, D.-S.; Munoz, E.; Kolla, H.; Manohar, S. K. *J. Am. Chem. Soc.* **2004,** *126*, 4462.

13. Hur, S.-H.; Park, O. O.; Rogers, J. A. *Appl. Phys. Lett.* **2005,** *86*, 243502.

14. Bradley, K.; Gabriel, J.-C. P.; Grüner, G. *Nano Lett.* **2003**, *3*, 1353.

15. Artukovic, E.; Kaempgen, M.; Hecht, D. S.; Roth, S.; Grüner, G. *Nano Lett.* **2005,** *5*, 757.

16. Snow, E. S.; Campbell, P. M.; Ancona, M. G.; Novak, J. P. *Appl. Phys. Lett.* **2005,** *86*, 033105/1.

17. Cao, Q.; Hur, S. -H., Zhu, Z. -T.; Sun, Y. G.; Wang, C. -J.; Meitl, M. A.; Shim, A.; Rogers, J. A. *Adv. Mater.* **2006,** *18*, 304.

18. Lee, K.; Wu, Z.; Chen, Z.; Ren, F.; Pearton, S. J.; Rinzler, A. G. *Nano Lett.* **2004,** *4*, 911.

19. Yoon, B. –J.; Hong, E. H.; Jee, S. E.; Yoon, D. –M.; Shim, D. –S.; Son, G. –Y.; Lee, Y. J.; Lee, K. –H.; Kim, H. S.; Park, C. G. *J. Am. Chem. Soc.* **2005,** *17*, 4049.

20. Suzuki, S.; Bower, C.; Watanabe, Y.; Zhou, O. *Appl. Phys. Lett.* **2000,** *76*, 4007.

21. Zhao, J.; Han, J.; Lu, J. P. *Phys. Rev. B*, **2002,** *65*, 193401/1.

22. Veinot, J. G. C.; Marks, T. J. *Acc. Chem. Res*., **2005,** *38*, 632.

23. Chen, C. –T. *Chem. Mater*. **2004,** *16*, 4389.

24. Mitschke, U.; Bauerle, P. *J. Mater. Chem.* **2000,** *10*, 1471.

25. Shim, H. –K.; Jin, J. –I. *Adv. Polym. Sci*. **2002,** *158*, 193.

26. Schlatmann, A. R.; Floet, D. W.; Hillberer, A.; Garten, F.; Smulders, P. J. M.; Klapwijk, T. M.; Hadziioannou, G. *Appl. Phys. Lett*. **1996,** *69*, 1764.

27. Scott, J. C.; Kaufman, J. H.; Brock, P. J.; Dipietro, R.; Salem, J.; Goitia, J. A. *J. Appyl. Phys.* **1996,** *79*, 2745.

28. Philips, J. M.; Kwo, J.; Thomas, G. A.; Carter, S. A.; Cava, R. J.; Hou, S. Y.; Krajewski, J. J.; Marshall, J. H.; Peck, W. F.; Rapkine, D. H.; Dover, R. B. V. *Appl. Phys. Lett.* **1994,** *65*, 115.

29. Ni, J.; Yan, H.; Wang, A.; Yang, Y.; Stern, C. L.; Metz, A. W.; Jin, S.; Wang, L.; Marks, T. J.; Ireland, J. R.; Kannewurf. C. R. *J. Am. Chem. Soc.* **2005,** *127*, 5613.

30. Jansseune, T. *Compound Semiconductor Magazine,* Sept **2003.**

31. Zhang, M.; Fang, S.; Zakhidov, A., A.; Lee, S. B.; Aliev, A. E.; Williams, C. D.; Atkinson, K. R.; Baughman, R. H. *Science*, **2005,** *309*, 1215.

32. Zhou, Y.; Hu, L.; Grüner, G. *Appl. Phys. Lett.* **2006,** *88*, 1231091

33. Ruzicka, B.; Degiorgi, L.; Gaal, R.; Thien-Nga, L.; Bacsa, R.; Salvetat, J.P.; Forro, L. *Phys. Rev. B* **2000,** *61*, 2468.

34. Huang, Q.; Evmenenko, G. A.; Dutta, P.; Lee, P.; Armstrong, N. R.; Marks, T.J. *J. Am. Chem. Soc.* **2005,** *127*, 10227.

35. Yan, H.; Scott, B.; Huang, Q.; Marks, T. J. *Adv. Mater.* **2004,** *16*, 1948.

36. Yan, H.; Lee, P.; Armstrong, N. R.; Graham, A.; Evmenenko, G. A.; Dutta, P.; Marks, T. J. *J. Am. Chem. Soc.* **2005,** *127*, 3172.

37. Pasquier, A. D.; Unalan, H. E.; Kanwal, S. M.; Chhowalla, M. *Appl. Phys. Lett.* **2005,** *87*, 203511.

38. Organic light-emitting materials and device VII, Kafafi, Z. H.; Lane, P. A. editors, Proceedings of SPIE Vol. 5214, **2003,** 40.

39. Hecht, D; Gruner, G., unpublished.

Chapter Four

1. Hung, L. S.; Chen, C. H. *Mater. Sci. Eng., R.* **2002**, *39*, 143.

2. Malliaras, G. G.; Scott, J. C. *J. Appl. Phys.* **1998**, *83*, 5399.

3. Schlatmann, A. R.; Floet, D. W.; Hillberer, A.; Garten, F.; Smulders, P. J. M.; Klapwijk, T. M.; Hadziioannou, G. *Appl. Phys. Lett.* **1996,** *69*, 1764.

4. Scott, J. C.; Kaufman, J. H.; Brock, P. J.; Dipietro, R.; Salem, J.; Goitia, J. A. *J. Appyl. Phys.* **1996,** *79*, 2745.

5. Philips, J. M.; Kwo, J.; Thomas, G. A.; Carter, S. A.; Cava, R. J.; Hou, S. Y.; Krajewski, J. J.; Marshall, J. H.; Peck, W. F.; Rapkine, D. H.; Dover, R. B. V. *Appl. Phys. Lett.* **1994,** *65*, 115.

6. Jansseune, T. *Compound Semiconductor Magazine*, Sept **2003.**

7. Martin, E. J. J.; Yan, M.; Lane, M.; Ireland, J.; Kannewurf, C. R.; Chang, R. P. H. *Thin Solid Films* **2004**, *461*, 309.

8. Ni, J.; Wang, L.; Yang, Y.; Yan, H.; Jin, S.; Marks, T. J.; Ireland, J.; Kannewurf, C. R. *Inorg. Chem.* **2005**, *44*, 6071.

9. Ni, J.; Yan, H.; Wang, A.; Yang, Y.; Stern, C. L.; Metz, A. W.; Jin, S.; Wang, L.; Marks, T. J.; Ireland, J. R.; Kannewurf. C. R. *J. Am. Chem. Soc.* **2005,** *127*, 5613.

10. Yang, Y.; Huang, Q.; Metz, A. W.; Jin, S.; Ni, J.; Wang, L.; Marks, T. J. *J. Soc. Inf. Disp.* **2005**, *13*, 383.

11. Hu, L.; Hecht, D.S.; Grüner, G. *Nano Lett.* **2004,** *4*, 2513.

12. Wu, Z.; Chen, Z.; Du, X.; Logan, J. M.; Sippel, J.;Nikolou, M.; Kamaras, K.; Reynolds, J. R.; Tanner, D. B.; Hebard, A. F.; Rinzler A. G. *Science*, **2004,** *305*, 1273.

13. Suzuki, S.; Bower, C.; Watanabe, Y.; Zhou, O. *Appl. Phys. Lett.* **2000,** *76*, 4007.

14. Zhao, J.; Han, J.; Lu, J. P. *Phys. Rev. B*, **2002,** *65*, 193401/1.

15. Wu, C. C.; Wu, C. I.; Sturm, J. C.; Kahn, A. *Appl. Phys. Lett.* **1997**, *70*, 1348.

16. Li, J.; Hu, L.; Wang, L.; Zhou, Y.; Grüner, G.; Marks, T. J. *Nano Lett.* **2006**, *6*, 2472.

17. Aguirre, C. M.; Auvray, S.; Pigeon, S.; Izquierdo, R.; Desjardins, P.; Martel, R. *Appl. Phys. Lett.* **2006**, *88*, 183104.

18. Zhang, D.; Ryu, K.; Liu, X.; Polikarpov, E.; Ly, J.; Tompson, M. E.; Zhou, C. *Nano Lett.* **2006**, *6*, 1880.

19. Pasquier, A. D.; Unalan, H. E.; Kanwal, S. M.; Chhowalla, M. *Appl. Phys. Lett.* **2005,** *87*, 203511.

20. Rowell, M. W.; Topinka, M. A.; McGehee, M. D.; Prall, H.-J.; Dennler, G.; Sariciftci, N. S.; Hu, L.; Grüner, G. *Appl. Phys. Lett.* **2006**, *88*, 233506.

21. Ke, L.; Kumar, R. S.; Chen, P.; Shen, L.; Chua, S.-J.; Burden, A. P. *IEEE Photonics Technology Letters* **2005**, *17*, 543.

22. Kawashima, T.; Ezure, T.; Okada, K.; Matsui, H.; Goto, K.; Tanabe, N. *J. Photochem. Photobiol., A* **2004**, *164*, 199.

23. Yang, Y.; Huang, Q.; Metz, A. W.; Ni, J.; Jin, S.; Marks, T. J.; Madsen, M. E.; DiVenere, A.; Ho, S.-T. *Adv. Mater.*, **2004**, *16*, 321.

24. Zhou, Y.; Hu, L.; Grüner, G. *Appl. Phys. Lett.* **2006,** *88*, 1231091

25. Tak, Y. H.; Kim, K. B.; Park, H. G.; Lee, K. H.; Lee, J. R. *Thin Solid Films* **2002**, *411*,12.

26. Yan, H.; Lee, P.; Armstrong, N. R.; Graham, A.; Evmenenko, G. A.; Dutta, P.; Marks, T. J. *J. Am. Chem. Soc.* **2005,** *127*, 3172.

27. Cui, J.; Wang, A.; Edelman, N. L.; Lee, P. A.; Armstrong, N. R.; Marks, T. J. *Adv. Mater.* **2001**, *13*, 1476.

Chapter Five

1. Burroughs, J. H.; Bradley, D. D. C.; Brown, A. R.; Marks, R. N.; Mackay, K.; Friend, R. H.; Burns, P.L.; Holmes, A. B. *Nature* **1990**, *347*, 539.

2. (a) Akcelrud, L. *Prog. Polym. Sci*. **2003**, *28*, 875. (b) Mitschke, U.; Bäurele, P. *J. Mater. Chem.* **2000**, *10*, 1471.

3. Wu, W.; Inbasekaran, M.; Hudack, M.; Welsh, D.; Yu, W.; Cheng, Y.; Wang, C.; Kram, S.; Tacey, M.; Bernius, M.; Fletcher, R.; Kiszka, K.; Munger, S.; O'brein, J. *Microelectron. J.* **2004,** *35*, 343.

4. Hughes, G.; Bryce, M. R. *J. Mater. Chem.* **2005**, *15*, 94.

5. (a) Morin, J.-F.; Leclerc, M. *Macromolecules* **2002**, *35*, 8413. (b) Yang, R.; Tian, R.; Yang, Y.; Hou, Q.; Cao, Y. *Macromolecules* **2003**, *36*, 7453. (c) Niu, Y.-H.; Hou, Q.; Cao, Y. *Appl. Phys. Lett.* **2003**, *82*, 2163.

6. (a) Müller, C. D.; Falcou, A.; Reckefuss, N.; Rojahn, M.; Wiederhirn, V.; Rudati, P.; Frohne, H.; Nuyken, O.; Becker, H.; Meerholz, K. *Nature* **2003**, *241*, 829. (b) Niu, Y.-H.; Huang, J.; Cao, Y. *Adv. Mater.* **2003**, *15*, 807.

7. (a) Ego, C.; Marsitzky, D.; Becker, S.; Zhang, J.; Grimsdale, A. C.; Müllen, K.; MacKenzie, J. D.; Silva, C.; Friend, R. H. *J. Am. Chem. Soc.* **2003**, *125*, 437. (b) Yang, J.; Jiang, C.; Zhang, Y.; Yang, R.; Yang, W.; Hou, Q.; Cao, Y. *Macromolecules* **2004**, *37*, 1211. (c)Yang, R.; Tian, R.; Yan, J.; Zhang, Y.; Yang, J.; Hou, Q.; Yang, W.; Zhang, C.; Cao, Y. *Macromolecules* **2005**, *38*, 244.

8. Scherf, U.; List, E. J. W. *Adv. Mater.* **2002**, *14*, 477.

9. Rees, I. D.; Robinson, K. L.; Holmes, A. B.; O'Dell, R.; Towns, C. R. *MRS Bull.* **2002**, *27*, 451.

10. Leeuw, D. M.; Simenon, M. J.; Brown, A. R.; Einerhand, R. E. F. *Synth. Met*. **1997,** *87*, 53.

11. (a) Moons, E. *J. Phys.-Condes. Matter* **2002**, *14*, 12235. (b) Morteani, A. C.; Dhoot, A. S.; Kim, J. S.; Silva, C.; Greenham, N. C.; Murphy, C.; Moons, E.; Sina, S.; Burroughes, J. H.; Friend, R. H. *Adv. Mater.* **2003,** *15*, 1708.

12. (a) Morteani, A. C.; Sreearunothai, P.; Herz, L. M.; Friend, R. H.; Silva, C. *Phys. Rev. Lett.* 2004, *92*, 247402. (b) Snaith, H. J.; Arias, A. C.; Morteani, A. C.; Silva, C.; Friend, R. H. *Nano Lett.* **2002,** *2*, 12. (c) Snaith, H. J.; Friend, R. H. *Thin Solid Films* **2004**, *451*, 567

13. Yan, H.; Lee, P.; Armstrong, N. R.; Graham, A.; Evmenenko, G. A.; Dutta, P.; Marks, T. J. *J. Am. Chem. Soc.* **2005,** *127*, 3172.

Curriculum Vita

Jianfeng Li

EDUCATION

December 2007 **Northwestern University**, Evanston, Illinois.

Ph.D. in Chemistry

June 2002 **University of Science & Technology of China,** Hefei, Anhui, China.

B.S. in Materials Science and Engineering, GPA: 3.7/4.0, cum laude.

RESEARCH EXPERIENCE

2002-present **Northwestern University,** Department of chemistry, Evanston, Illinois

Research Assistant.

- Synthesized and characterized hole injection/transportation and emissive materials (small molecules and polymers) for OLEDs.
- Fabricated and characterized OLED devices (I-V, Light-V, Efficiency- V, and degradation testing).
- Developed an electrochemically-active molecular probe that can be self-assembled (SM) on transparent conductive oxides (TCOs) electrode surfaces to study the electrochemical properties.
- Fabricated polymer-based LEDs with the conducting, transparent SWNT film anodes.
- Investigated systematically nanoscale modifying layer for hole injection/transport in (OLEDs).

2000-2002 **University of Science & Technology of China,** Hefei, Anhui, China.
Undergraduate research assistant.
Photoluminescence Study of XO (X=Zn, Sn) Nanocrystallites with BN Capsules and characterization by X-ray diffraction (XRD), HR-TEM.

TEACHING EXPERIENCE

Winter 2004 **Northwestern University,** Department of chemistry, Evanston, Illinois

Teaching Assistant for Advanced Analytical Chemistry Laboratory

- Instructed multi-week course on GC and Taught laboratory sections for senior undergraduates.

2002-2003 **Northwestern University,** Department of chemistry, Evanston, Illinois
Teaching Assistant for General Chemistry Laboratory

- Taught laboratory sections and served as a grader for problem sets and exams.

AWARDS/HONORS

2003 Outstanding Teaching Assistant, Northwestern University.

2002 Cum laude, University of Science & Technology of China

2001 The third prize of the 7th **"Challenge Cup"-the National Contest of Academic Research for the Undergraduates in China**

2001 "Guanghua" Scholarship, USTC (30 out of 5000 students)

Publications, conference papers and working papers

Publications

"Transparent Active Matrix Organic Light-emitting Diode Displays Driven by Nanowire Transistor Circuitry" Ju, S.; **Li, J.**; Liu, J.; Zhou, C.; Facchetti, A.; Janes, D. B.; Marks, T. J., Accepted by *Nano Letters.*

"Triarylamine Siloxane Anode Functionalization/Hole Injection Layers in High Efficiency/High Luminance Small-Molecule Green- and Blue-Emitting Organic Light-Emitting Diodes." Huang, Q.; **Li, J.**; Evmenenko, G. A.; Dutta, P., and Marks, T. J., *J. Appl. Phys.*, **2007,** 101, 093101/01-093101/13.

"Organic Light-Emitting Diodes Having Carbon Nanotube Anodes." **Li, J.;** Hu, L.; Wang, L.; Zhou, Y.; Grüner, G.; and Marks, T. J., *Nano Letters*, **2006**, 6, 2472-2477.

"Systematic Investigation of Nanoscale Adsorbate Effects at Organic Light-Emitting Diode Interfaces. Interfacial Structure-Charge Injection-Luminance Relationships" Huang, Q.; **Li, J.;** Evmenenko, G. A.; Dutta, P., and Marks, T. J., *Chem. Mater*., **2006**, 18, 2431-2442.

"Photoluminescence Enhancement of ZnO Nanocrystallites with BN Capsules" **Li, J.;** Yao, L.; Ye, C.; Mo, C.; Cai, W., *Journal of Crystal Growth*, **2001**, 223, 535-538.

"Photoluminecence Study of XO (X=Zn, Sn) Nanocrystallites with BN Capsules," **Li, J.;** Yao, L.; Ye, C.; Mo, C.; Cai, W., *Acta Physica Sinica*, **2001**, 50, 1623-1625

Manuscripts in preparation

"Cyan and Green Light-emitting Diodes from a Fluorene-Based Copolymer" **Li, J.;** Lu, G.; Facchetti, A.; and Marks, T. J., To be submitted.

"Characterization of Transparent Conducting Oxide Surfaces Using Self-assembled Electroactive Monolayers" **Li, J.;** Evmenenko, G. A.; Dutta, P., and Marks, T. J., To be submitted.

"Highly Transparent and Conductive Carbon Nanotube-Indium Tin Oxide Double-layer Thin Film as Anode for Organic Light-Emitting Diodes" **Li, J.;** Hu, L.; Liu, J.; Grüner, G.; and Marks, T. J., To be submitted.

"Air-Stable, Cross-Linkable hole-Injecting/Tranporting Interlayers for Improved Charge Injection in Organic Light-Emitting Diodes" **Li, J.;** and Marks, T. J., To be submitted.

Conference Papers

"Novel fluorene-based copolymer for cyan and green light-emitting diodes." **Li, J.;** Lu, G.; Facchetti, A.; Marks, Tobin J. PMSE Preprints **2007**, 96, 757-758.

"New polymeric hole transport layer materials applied to indium-tin-oxide anodes by a dipping process." Huang, Q.; **Li, J.;** Scott, B.; Yan, H.; Marks, T. J., PMSE Preprints, **2004,** 91, 490-491.

PRESENTATION

- **Li, J**; Hu, L; Gruner, G.; Marks, T. J. "Organic Light-emitting DiodesHaving Carbon Nanotube Anodes" MRS Spring Meeting, San Francisco, CA, April 12th, 2007

- **Li, J.;** Lu, G.; Facchetti, A.; and Marks, T. J. "Novel Fluorene-based Copolymer for Cyan and Green Light-emitting Diodes" 233rd ACS National Meeting, Chicago, IL March 28th, 2007

- **Li, J.;** Huang, Q.; Wang, L.; Evmenenko, G.; Dutta, P.; Marks, T. J. "Studying the electrochemical properties of transparent conducting oxide anode surfaces by the self-assembled monolayer." 231st ACS National Meeting, Atlanta, GA, March 30th , 2006

- Huang, Q.; **Li, J.;** Scott, B.; Yan, H.; Marks, T. J., "New polymeric hole transport layer materials applied to indium-tin-oxide anodes by a dipping process." 228th ACS National Meeting, Philadelphia, PA, August 24th , 2004

PATENT

Hu, Liangbing; Gruner, George; **Li, Jianfeng**; Marks, Tobin. "**Organic light-emitting diodes with nanostructure film electrodes"** U.S. Pat. Appl. Publ. (2007), 12pp. Cont.-in-part of Appl. No. PCT/US05/047315.

PROFESSIONAL AFFILIATION

Sigma Xi- the Scientific Research Society

American Chemical Society

Materials Research Society

Phi Lambda Upsilon

SPIE-The International Society for Optical Engineering